Deep Underground Neutrino Experiment (DUNE)

DUNE Near Detector
Updated Conceptual Design Report

SAND Chapter

July 16, 2024

The DUNE Collaboration

Contents

List of Figures

List of Tables

Chapter 1

System for on-Axis Neutrino Detection

1.1 Lead/Scintillating-Fiber Calorimeter (ECAL)

1.1.1 ECAL Design and Structure

The KLOE ECAL [2] is a fine sampling lead-scintillating calorimeter with photomultiplier tube (PMT) readout. The central part (barrel) approximating a cylindrical shell of 4 m inner diameter, 4.3 m active length and 23 cm thickness ($\sim 15\ X_0$), consists of 24 modules with trapezoidal cross-section and fibers running parallel to the cylinder axis. Two endcaps close the barrel hermetically. Each of them consists of 32 “C” shaped modules arranged vertically along the chords of the circle inscribed in the barrel (see Fig. 1.1). In the endcap modules fibers run perpendicular to the cylinder axis, so that for the whole ECAL fibers are mostly transverse to the particle trajectories.

The modules are read out on the two sides through Plexiglas light guides optically coupled to fine mesh PMTs. The readout granularity is $\sim 4.4 \times 4.4\ \mathrm{cm}^2$. Each barrel module has 60 channels per side while endcap modules have 10, 15 or 30 channels per side depending on their width. The total number of readout channels is 4880, corresponding to a total of 2440 cells read-out at both ends and arranged in five layers. Both in the barrel and in the endcaps, PMT axes are almost parallel to the magnetic field, in order to decrease the field effects on PMT response, and to increase hermeticity (see Fig. 1.1).

The basic calorimeter structure consists of an alternating stack of 1 mm scintillating fiber layers glued between thin grooved lead foils, obtained by passing 0.5 mm thick lead foils through rollers of a proper shape. The grooves in the two sides of each foil are displaced half a pitch, so that fibers are located at the corners of adjacent, quasi-equilateral triangles, resulting in an optimal and uniform arrangement of the fibers in the stack. The final composite has a fiber : lead : glue volume ratio of approximately 48 : 42 : 10, a density of $\sim 5\ \mathrm{g/cm}^3$ and a radiation length X_0 of $\sim$ 1.6 cm, is self-supporting and can be easily machined (see Fig. 1.2). The efficiency for low energy photons is high due to the very small lead foil thickness ($< 0.1\ X_0$).

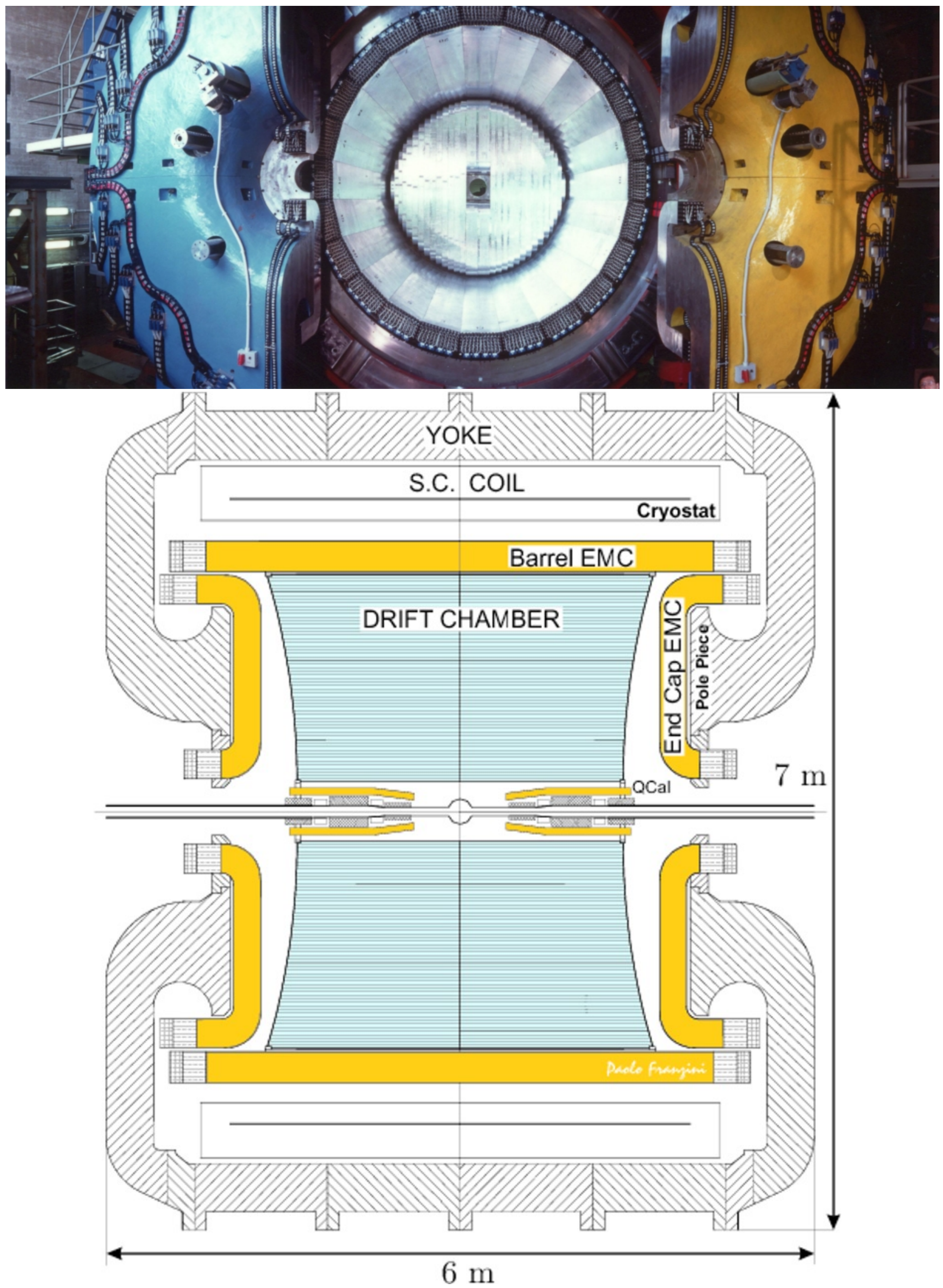

Figure 1.1: KLOE ECAL (top) and KLOE Detector cross section (bottom).

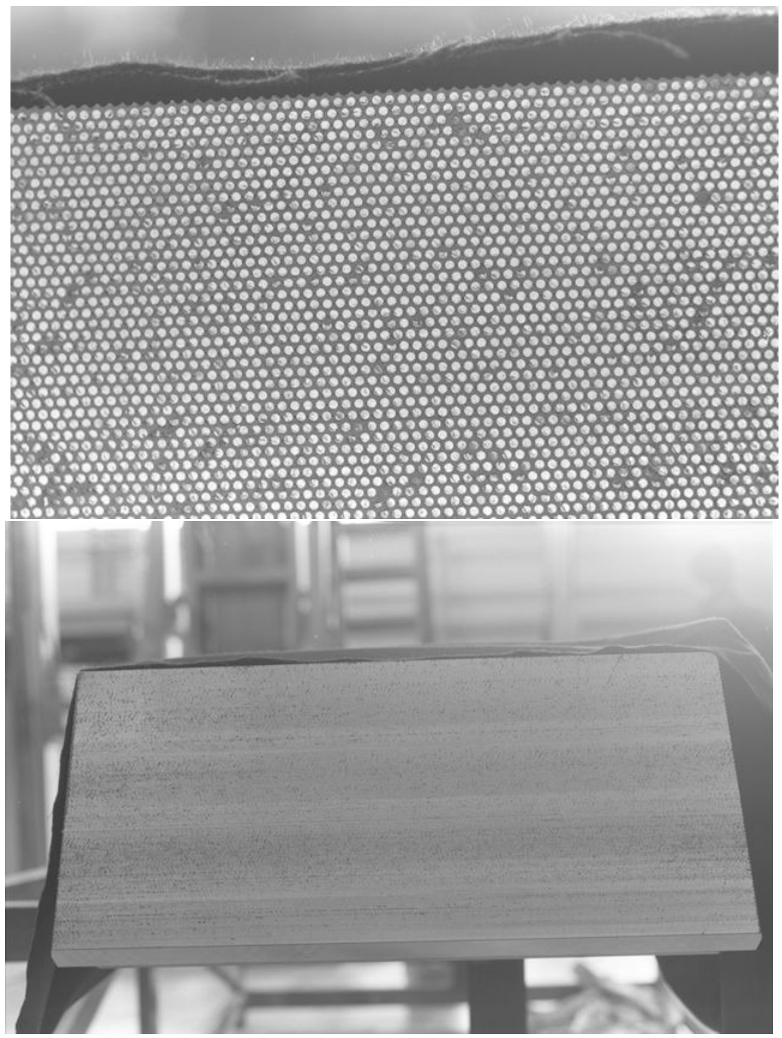

Figure 1.2: KLOE ECAL lead-fiber structure detail (top) and barrel module cross-section view (bottom).

1.1.1.1 Scintillating Fibers

Two types of fibers (Kuraray SCSF-813 and Pol.Hi.Tech. 0046) with a total length of 15,000 km have been used to assembly the ECAL. The former have higher light output and longer attenuation length, the latter are less expensive. Anyway, the performance differences are not significant and the Kuraray fibers are used in the inner half of the calorimeter. All fibers have an attenuation length between 3 and 5 m and produce ~ 1 PE for 1 mm of crossed fiber at a distance of 2 m from PMT. The emitted light is in the blue-green region ($\lambda_{peak} \sim 460$ nm).

1.1.1.2 PMTs

The light guides matching the module end faces to the photo-tube windows begin with a mixing section and terminate with a Winston cone [3], passing from an approximately squared to a circular area with a concentration factor of ~ 4 (see Fig. 1.3).

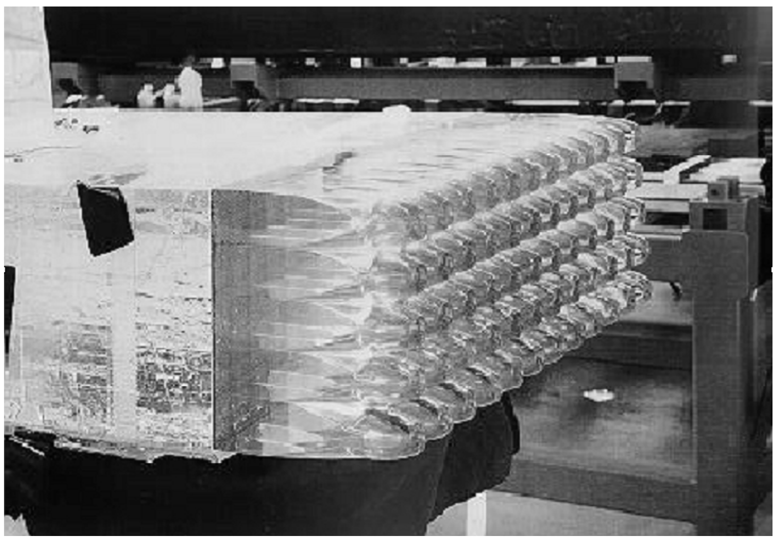

Figure 1.3: Light guides at one end of a KLOE ECAL barrel module before PMT installation.

The PMTs must operate in a magnetic field with the suitable efficiency, linearity, timing resolution and dynamical range. The Hamamatsu R5946/01 1.5" tubes [4] have been chosen because the electron multiplication occurs between dynodes made of fine mesh, very close to each other. Then the effect of the magnetic field on the electron path is very small. The field intensity at PMT location is less than 0.2 T and the PMT alignment is such that the component transverse to the tube axis is less than 0.07 T. It has been measured that the PMT gain decreases by 10% when the field is on, but linearity and resolution are not affected.
The PMTs are operated with grounded cathodes in order to eliminate leakages, possible origin of noise and field distortions.
A thin aluminum cylinder holds each PMT mechanically in place and a spring pushes gently it against the light guide. The optical contact PMT-light guide is made by means of Bicron optical gel BC-630.

Each PMT is connected to a PMT-base, hosting the high voltage divider and a preamplifier (see Fig. 1.4). The PMT-base has low noise, high bandwidth and high output dynamic range in order to avoid distortion of the fast pulses from the PMT.

The cables carrying high and low voltage, a test pulse and the output signal are connected to the PMT-base through its rear connector.

Figure 1.4: KLOE PMT-base.

1.1.1.3 SiPMs as Possible Spare for PMTs

The silicon photomultipliers (SiPMs) work efficiently in a range compatible with the typical wavelength-shifted light of the scintillating fibers, and are insensitive to magnetic fields, unlike PMTs. In addition, since SiPMs operate at low voltage, the high voltage power supply would no longer be required, with convenience in compactness and cost.

For the aforementioned reasons, the substitution of SiPMs with PMTs in the System for on-Axis Neutrino Detection (SAND) calorimeter, with a possible improvement of efficiency and timing resolution, has been investigated [5]. The SiPMs used in this test are the 4×4 arrays of the Hamamatsu S13361-3050 series. Anyway, it is excluded to substitute the single PMT channel with 16 readout channels. Thus, in these measurements, the SiPM array is considered as a unique element. The MPPC series has been chosen since it achieves the maximum Photo-Detection Efficiency (PDE_{MAX}) close to the peak wavelength of the scintillating fibers (typically PDE_{MAX} = 40% at $\lambda = 450$ nm). But the quantum efficiency of the Hamamatsu R5946 1.5' mesh photomultiplier presently used in the calorimeter is 23% at $\lambda = 390$ nm.

A block ($24.5 \times 13.5 \times 40$ cm^3) of the lead-scintillating fiber calorimeter has been equipped (Fig. 1.5, left) with light guides like in KLOE. These light guides are shaped to cover the PMT surface and are not optimal for the smaller SiPM surface. Excluding the option to remove the present light guides and to mount new ones in the calorimeter, the test has been performed gluing a small adapter on the light guide to optimize the coupling with the SiPM (Fig. 1.5, right).

The signals induced by cosmic muons have been collected on one side by SiPM and on the opposite one by standard KLOE PMT. This setup allowed to compare directly the different performance. The measurements were performed for two SiPMs and two PMTs. The average results for efficiency and timing resolution in these conditions are reported in Table 1.1. Even if the differences are small, PMTs perform better in the present setup. The difficulties in coupling SiPMs with the light guides without deep mechanical changes, the lack of improvement, the cost, and the necessary commissioning time advise against the substitution of 4880 available and tested PMTs with new SiPMs. Nevertheless, the results from this study do not exclude the use of SiPMs as a spare. A mechanical setup is under study.

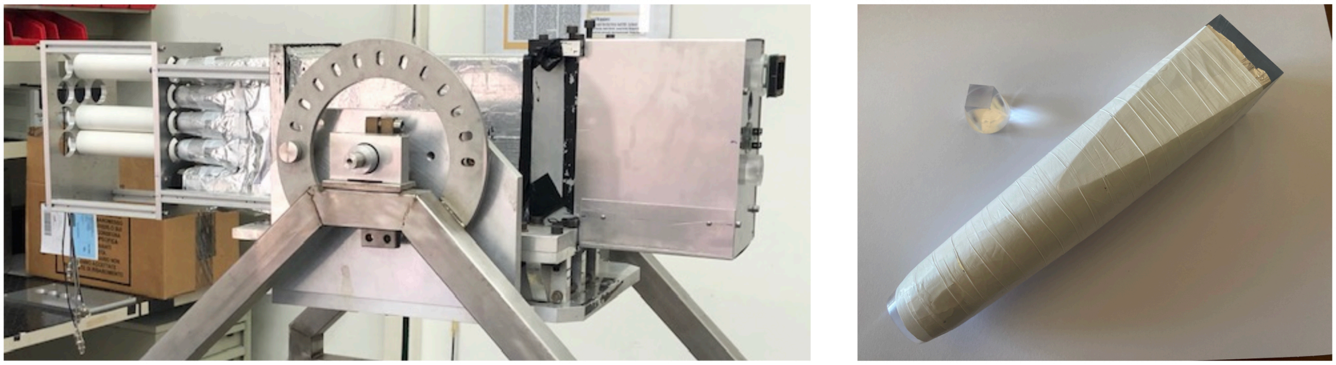

Figure 1.5: Left: experimental setup to compare PMT and SiPM. The SiPMs are on the right, the calorimeter block is at the center, the PMTs are on the left. Right: light guide and adapter for SiPM.

Table 1.1: Comparison of SiPM performance with PMT ones

	Efficiency (%)	Time Resolution (ps)
PMT	91.6 ± 0.2	197 ± 4
SiPM	90.8 ± 0.3	240 ± 3

1.1.2 Performance in KLOE Experiment

In KLOE the signal from the PMT is split into three ways. One split signal is used for analogical sums for trigger purposes. Two split signals are sent to ADC and to TDC boards after discrimination [2]. The TDC signal is delayed by a monostable while a continuous sampling technique is used for the ADC. The ADC is coupled to an analogue integrator and the signal of the integrator is sampled each 450 ns by two sample and hold circuits. After the trigger a third sampling of the integrator is performed and the value of the buffered signal is subtracted to compute the signal charge. A calibration and equalization in response of the calorimeter has been performed with cosmic rays by selecting minimum ionizing particle (MIP) and measuring, for each calorimeter channel, the peak of the energy released at calorimeter center. The accuracy of MIPs determination was typically of 1%. By adjusting the PMT high voltages, the whole calorimeter was equalized at a 5% level. Run by run PMT relative gain variations (a typical run lasts about one hour) are corrected by recalibrating each cell response using Bhabha scattering events ($e^+e^- \rightarrow e^+e^-$), copiously produced at the DAΦNE collider [6]. The absolute energy scale is set run by run using $e^+e^- \rightarrow \gamma\gamma$ events. with photons of energy 510 MeV. The mean time of each cell is obtained from the measured times t^A, t^B at both ends as

$$t = \frac{t^A - t_0^A}{2} + \frac{t^B - t_0^B}{2} - \frac{L}{2v} - t_0^G \tag{1.1}$$

where t_0^A, t_0^B are the time offsets for each channel, v is the light velocity into the fiber, L is the calorimeter cell length and t_0^G is an overall time offset related to the trigger start time. Using cosmic ray events the $t^A - t^B$ difference distribution is measured. The mean value of this distribution is used to set the difference $t_0^A - t_0^B$ while the width is used to determine v.

The position of the impinging particle along the fibers (conventionally the z-coordinate in the

KLOE reference system) is determined using the relation:

$$z = \left(\frac{t^A - t_0^A}{2} - \frac{t^B - t_0^B}{2} \right) \cdot v \tag{1.2}$$

The previous determination of $t_0^A - t_0^B$ allows to reconstruct the longitudinal position z. This information is used in cosmic ray analysis to associate the energy deposit in the fibers to a cosmic ray track in the KLOE drift chamber. The cosmic rays selected in this way are used to inter-calibrate t_0^A and t_0^B among the cells, imposing that the difference in time between two cells is the expected propagation time of the cosmic ray. Finer calibrations are performed run by run using $e^+e^- \to \gamma\gamma$ events. With this sample the time offset t_0^A, t_0^B of the hit cells are calibrated imposing $t - r/c = 0$ where r is the photon path length and t its reconstructed time.

The trigger formation time has a spread of few tens of nanoseconds. In order to avoid a worsening of the time resolution, the trigger signal is phase locked with the RF signal. The event time is therefore discretized according the bunch crossings. The delay due to the cable length shifts the time of flight of a constant quantity. This shift is determined from the position of the largest peak of the $t - r/c$ distribution for $e^+e^- \to \gamma\gamma$ events. The association of an event to the correct bunch crossing is performed off-line and depends on the event topology, being the bunch crossing time spacing of 2.7 ns. For example, in events with prompt photons the correct bunch is easily determined by imposing the $t - r/c = 0$ constraint. On the other hand, for $K_S \to \pi^+\pi^-$ events, the bunch crossing is determined requiring $t - l/v_\pi = 0$, where l is the pion track length and v_π the pion velocity determined by the measurement of its momentum in the KLOE Drift Chamber.

Cells close in space and time are grouped into energy clusters. The cluster energy E is the sum of the cell energies, the cluster time and position are energy-weighted averages.

The efficiency has been evaluated with different data samples (see Fig. 1.6): $e^+e^- \to e^+e^-\gamma$, $\phi \to \pi^+\pi^-\pi^0$, and $K_L \to \pi^+\pi^-\pi^0$ In the first case, events are selected requiring two tracks and zero missing mass, in the other cases two tracks and one cluster are required. The position of the second cluster is evaluated by missing momentum from photon direction and pion momenta. For energies larger than 100 MeV a constant value of more than 98% is observed. The loss in efficiency below 100 MeV is mainly due to ADC and TDC thresholds and the clustering algorithm.

The time resolution has been evaluated using $\phi \to \eta\gamma$, $\phi \to \pi^0\gamma$, $e^+e^- \to e^+e^-\gamma$ events (see Fig. 1.7). The resolution is evaluated from the standard deviation of the $t - r/c$ distribution, yielding:

$$\sigma_t = \frac{54\,\text{ps}}{\sqrt{E(GeV)}} \oplus 140\,\text{ps} \tag{1.3}$$

The constant term of 140 ps is due to residual detector miscalibration of $\mathcal{O}(100\,\text{ps})$, the time jitter of the RF coincidence and the uncertainty on the interaction point position due to the finite length of the bunches.

Cluster positions are measured with a resolution of 1.3 cm in the coordinate transverse to the fibers, and with a resolution of $1.2\,\text{cm}/\sqrt{E(GeV)}$ in the longitudinal coordinate, using time differences (1.2).

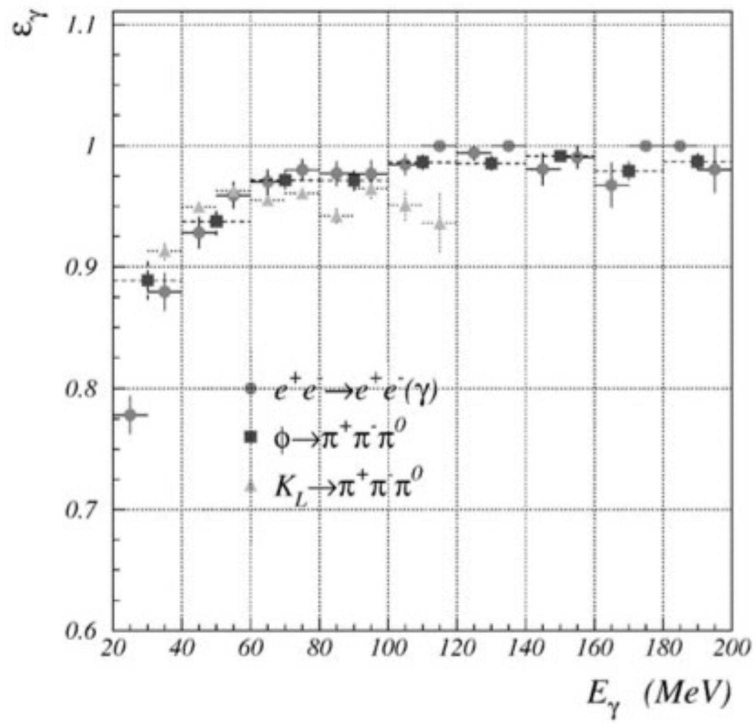

Figure 1.6: KLOE ECAL photon efficiency vs energy.

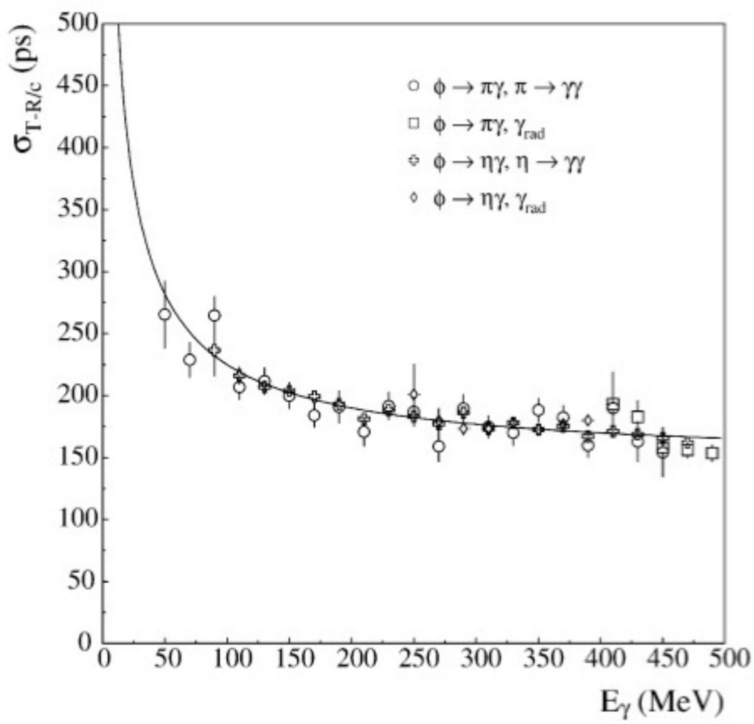

Figure 1.7: KLOE ECAL photon time resolution vs energy. The fit result $\sigma_t = 54\,\text{ps}/\sqrt{E(GeV)}$ is superimposed.

The energy response and resolution are studied using $e^+e^- \to e^+e^-\gamma$ events. The photon energies are evaluated with high precision by the e^+e^- momenta and then compared with the reconstructed cluster energies (see Fig. 1.8). The ECAL response is linear at better than 2% for $E_\gamma > 75\,\mathrm{MeV}$, while a 5% deviation is observed at lower energy. The energy resolution is:

$$\frac{\sigma(E)}{E} = \frac{5.7\%}{\sqrt{E(GeV)}} \tag{1.4}$$

with a negligible constant term.

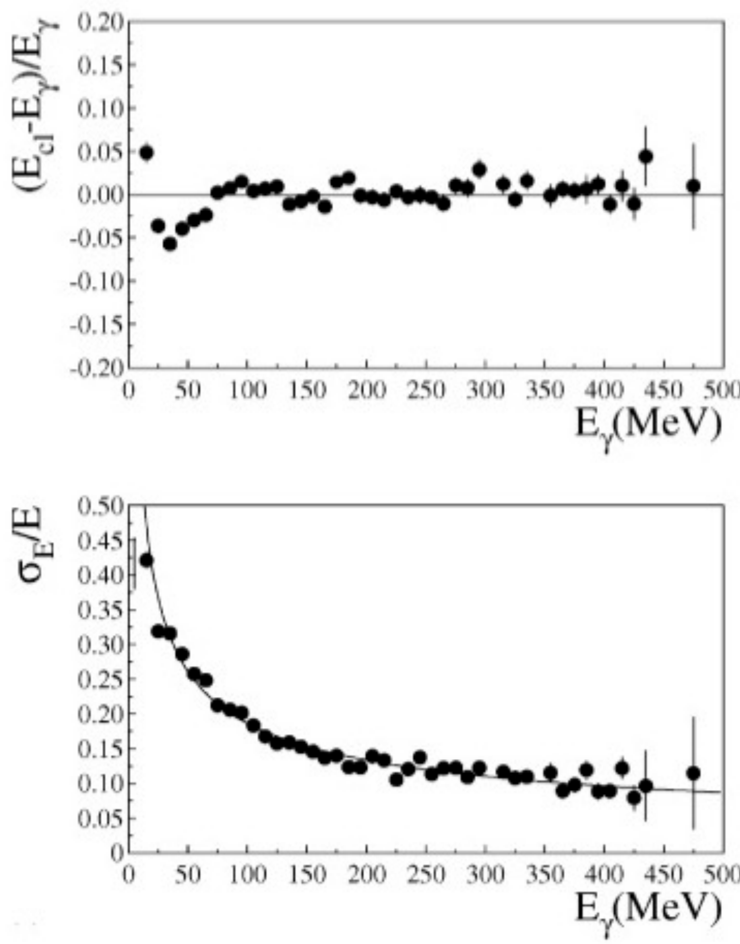

Figure 1.8: KLOE ECAL energy linearity (top) and resolution (bottom) vs energy. The fit result $\sigma(E)/E = 5.7\%/\sqrt{E(GeV)}$ is superimposed.

The time and energy resolution performance (1.3) and (1.4) of the KLOE ECAL did not show sign of worsening during the first KLOE data taking campaign (years 2001-2006) and the second campaign for the KLOE-2 experiment (years 2014-2018). Resolutions were measured again during KLOE-2 confirming the previous results:

$$\begin{aligned} \sigma_t &= \frac{58\,\mathrm{ps}}{\sqrt{E(GeV)}} \oplus 135\,\mathrm{ps}\ , \\ \frac{\sigma(E)}{E} &= \frac{5.6\%}{\sqrt{E(GeV)}}\ . \end{aligned} \tag{1.5}$$

The overall detection efficiency to neutrons of a small prototype of KLOE ECAL has been measured at the neutron beam facility of The Svedberg Laboratory, TSL, Uppsala, in the kinetic energy range from 5 to 175 MeV [7].

The measurement of the neutron detection efficiency of a NE110 scintillator provided a reference calibration. At the lowest trigger threshold, the overall ECAL prototype efficiency, ϵ_{calo}, ranges from 40% to 50%. This value largely exceeds the estimated 8 − 16 % expected if the response were proportional only to the scintillator equivalent thickness (see Fig. 1.9).

A detailed simulation of the calorimeter and of the TSL beamline has been performed, showing an overall neutron efficiency of about 50 %, when no trigger threshold is applied. The reasons of such an efficiency enhancement, in comparison with the typical scintillator-based neutron counters, are explained by the existence of a contribution from the passive material to neutron detection efficiency in a high-sampling calorimeter configuration as in KLOE ECAL.

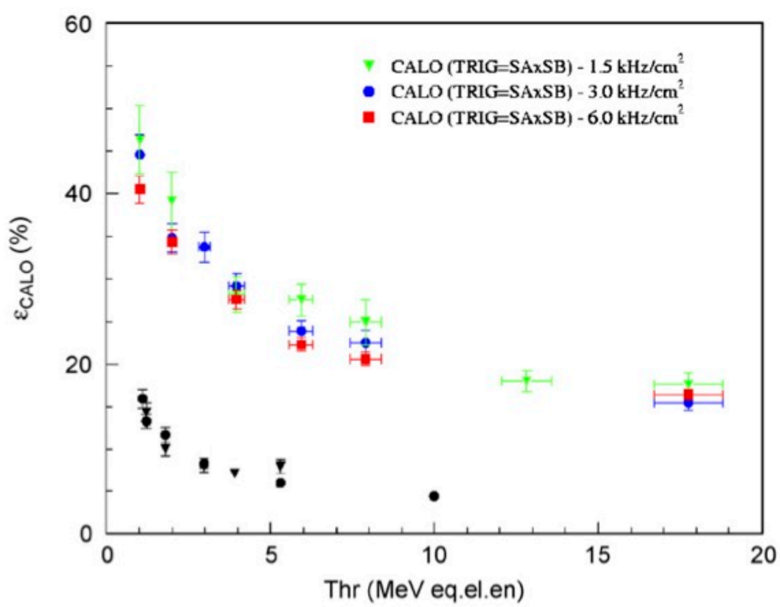

Figure 1.9: Dependence of the neutron efficiency ϵ_{calo} of the KLOE ECAL prototype on the trigger threshold. The horizontal scale is in MeV set for electron response. The scintillator efficiency measurements are reported (black points), scaled by the ratio between the two scintillator thicknesses.

1.1.3 Requirements for ECAL

The expected Physics performance of SAND exposed to the DUNE neutrino beam have been extensively studied with a complete Monte Carlo simulation of the proposed detector [8]. For the calorimeter the mentioned KLOE ECAL performance in terms of photon efficiency, time and energy resolutions (1.3)-(1.4), and efficiency to neutrons has been assumed in the simulation.

The ECAL impact on the SAND event reconstruction and background rejection capabilities is important, especially for time resolution, affecting the particle identification capabilities with the time of flight technique, and for detection efficiency of low energy photons and neutrons. The energy resolution appears a less critical parameter, being at the level of some percent for the highest photon and electron energies of few GeVs (with longitudinal leakage that starts becoming important for a 15 X_0 thick calorimeter), and dominated for hadrons by large fluctuations due to the limited shower containment (the ECAL thickness corresponds to about one interaction length). These fluctuations can be reduced by adding information on the event from the tracker system and/or imposing kinematic constraints, when possible.

Anyhow special attention is devoted in the ECAL dismounting and refurbishment operations, and in re-designing the front-end electronics to keep the ECAL performance at the same level as in KLOE.

1.1.4 ECAL Calibration and Monitor System

The plan is to calibrate the SAND ECAL following the experience of many years of operation of the ECAL in the KLOE experiment, described in Sect.1.1.2.
A several step process can be envisaged:

1. Cell-by-cell response equalization and time offset alignment with MIPs;
2. Setting the absolute energy scale, at cluster level, with photons from π^0 decays and electrons from beam events;
3. Timing alignment with the rest of SAND detector by using muons, pions, and electrons from events with reconstructed vertices in the inner tracker.

For the first step cosmic muons, selected with a dedicated trigger in period of no beam, can be used as MIPs. However, a reduction factor of about 100 of the rate of cosmic muons with respect to KLOE has to be taken into account due to the shielding of both the soil and the rock above the ND in DUNE.
Due to the reduced rate of cosmics, and due to the fact that the best orientation for calibration tracks is perpendicular to the ECAL module surface, also a sample of almost horizontal MIPs would be very useful. Muons produced in neutrino interactions in the rocks of the ND hall and in the material in front of the ECAL, including the iron yoke of the magnet, could be exploited. According to preliminary studies [8], about 1.5×10^3 of such muons per beam spill reach the ECAL; by applying a quality selection only a fraction of these events will be useful for calibration.

1.1.5 ECAL Electronics

The neutrino interactions inside the SAND detector have to be identified by reconstructing the particles in the final state of the various processes. In particular, when these particles reach the ECAL modules, the PMT signals of both sides of the hit cells are readout and converted by the ECAL electronics digital counts for time and amplitude. From this information the energy releases into the hit cells, their times and positions are derived [2]. The ECAL front-end electronics should match the requirements in terms of Physics performance, dynamical range of the PMT signals, and minimization of their pile-up in SAND exposed at the DUNE neutrino beam.

As the existing ECAL electronics were optimized to work in the conditions of the KLOE experiment, different from those in SAND. A comparative study of the physical requirements in SAND and the characteristics of the existing front-end electronics is therefore important for the final choice of the SAND readout electronics.

1.1.5.1 Studies for the Optimization of the PMT Working Point

The neutrino interaction processes inside the detector are simulated with the neutrino event generator GENIE. The response of the detector, reconstructed with *gegede* and *dunendggd*, is performed with *edep-sim* and digitized with *sand-reco* [8]. In particular, the tracks are used for vertex reconstruction whose position is useful for event classification. A fiducial volume (FV) for the interesting neutrino events is defined as the volume delimited by the surface at 20 cm distance from the inner ECAL surface.

The MC sample used for the analysis presented in the following contains 118592 events of neutrino interactions with the SAND detector (the same sample has been used in other studies presented in Ref. [8]) and the beam in the FHC polarization mode, corresponding to a total of 1.011×10^{17} protons on target (POT). At 1.2 MW beam power and an expected rate of 7.5×10^{13} POT/spill these events correspond to $\sim$ 27 minutes of data taking, or equivalently to $\sim$ 15 minutes at 2.1 MW beam power.

The associated neutrino energy spectrum is shown in Fig. 1.10 for all events and in Fig. 1.11 only for events with the primary vertex in the FV. It is worth noting that the spectra of the different neutrino components in the beam have a tail extending up to $\mathcal{O}(100\,\mathrm{GeV})$.

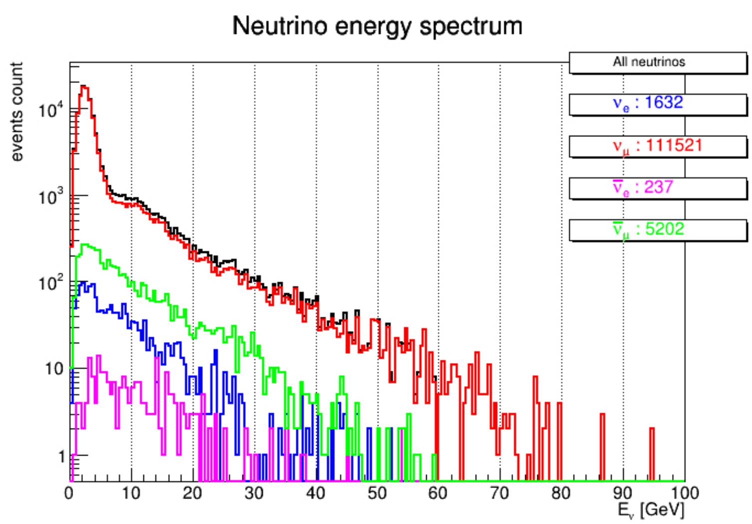

Figure 1.10: Neutrino energy spectrum for all events in the MC simulation.

The spatial distribution of neutrino interaction vertices is shown in Fig. 1.12 for all events (top) and for events in the FV (bottom). As shown in the top panel, the primary vertices are mostly located in the most massive regions, the internal ring of ECAL and the external ring representing the iron yoke. In the bottom panel, a thickening of primary vertices is observed on the left side

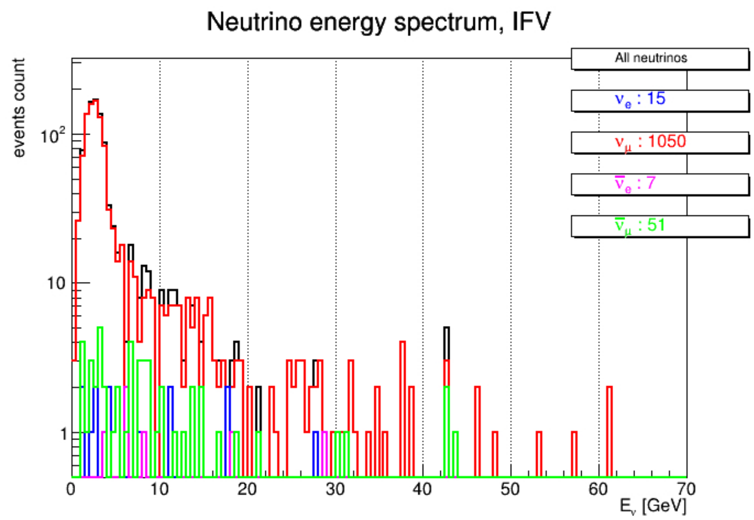

Figure 1.11: Neutrino energy spectrum for simulated events with the primary neutrino interaction vertex contained in the FV.

that corresponds to GRAIN.

The response of ECAL is digitized similarly as in the official KLOE Monte Carlo simulation. The deposited energy in the cells is propagated to PMT with a double exponential attenuation curve, according to the attenuation length of light in the fibers and converted in photoelectron (PE). The light yield is $\sim$ 1 PE/MeV of total energy of the particle at the center of the cell of a barrel module. The discriminator threshold is set to 2.5 PE, and a constant fraction discriminator at 15% of the signal is simulated, as well as a multihit TDC (30 ns integration time + 50 ns dead time).

For each of the 118592 events of neutrino interaction, and for each cell of all the ECAL modules, barrel and endcaps, the number of PEs is recorded. Furthermore, the same analysis can be performed selecting only the primary vertex of the neutrino interaction in the FV. The distribution of the number of PE of all the cells involved for each event was produced, as well as the distribution of the total release of PE in the calorimeter for each event. These distributions are shown in Fig. 1.13. It can be noticed that the number of PEs can reach the value of about 25000 for a single cell.

The next step is to relate the PE distribution to the neutrino energies. The neutrino energy range 0 - 100 GeV is considered, with a particular focus on the energy range below 10 GeV, relevant for the neutrino oscillation analyses in DUNE. Figures 1.14 and 1.15 show the distributions of the number of PEs corresponding to different slices of the neutrino energy spectrum. It can be noticed the correlation between the distribution of the number of PEs and the neutrino energy.

Then, the same distributions are evaluated considering only those cells with a number of PEs greater than a chosen threshold. Figures 1.16, 1.17, 1.18, and 1.19 show the resulting distributions in the case of a threshold of 1000, 2000, 3000 and 4000 PEs, respectively.

Counting the number of events for the slices of energy below 10 GeV, the conclusion that only

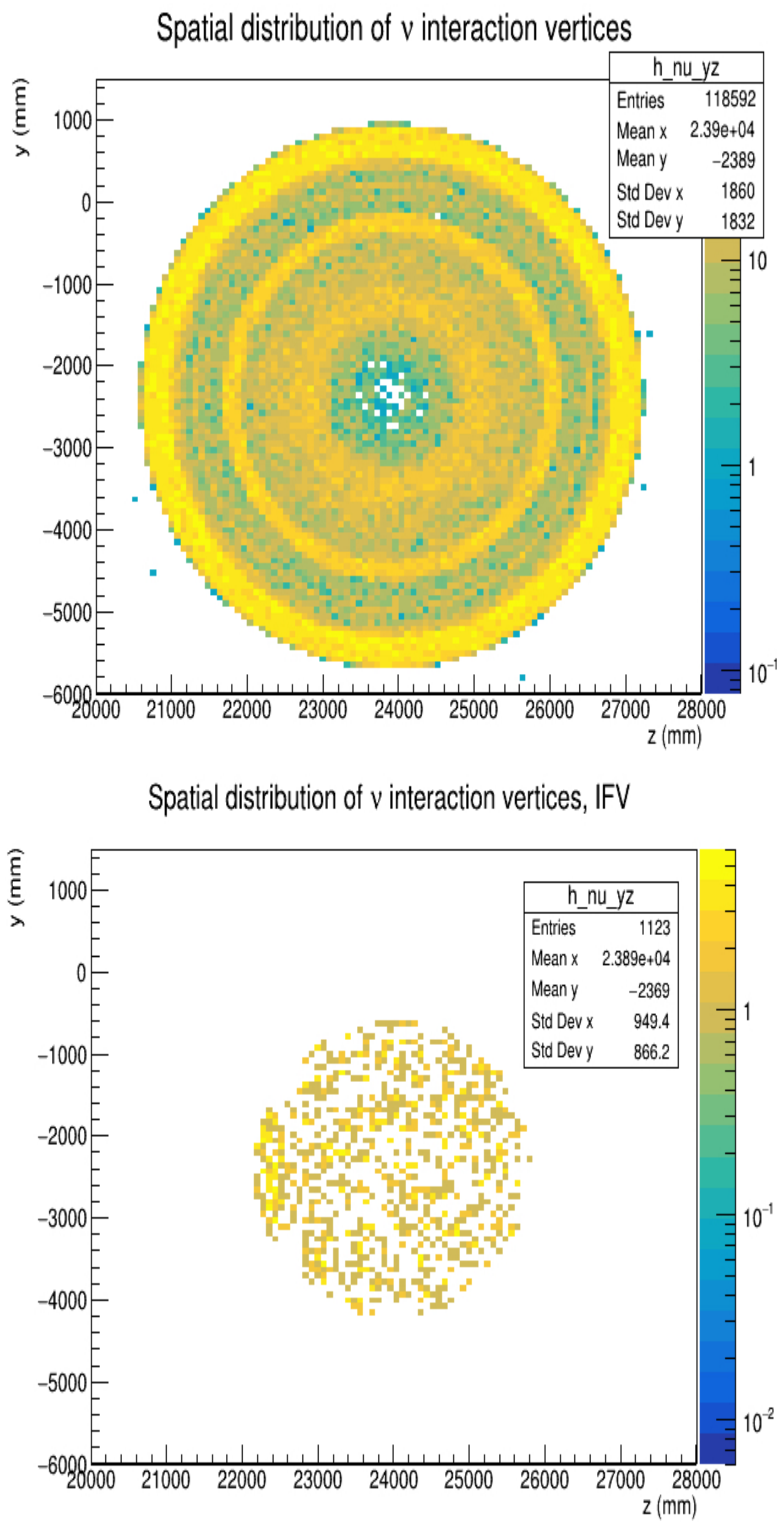

Figure 1.12: Spatial distributions of the neutrino interaction vertices for all events (top) and in the FV (bottom) for the MC sample used for the analysis.

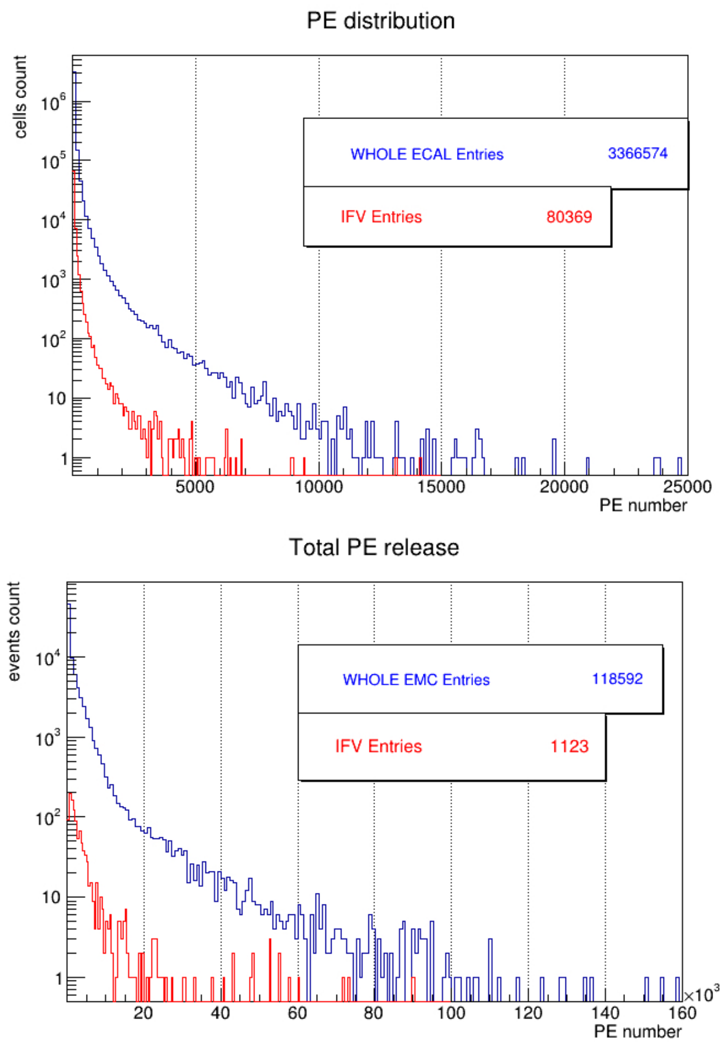

Figure 1.13: (Top) Distribution of the number of PEs released per cell and per event, for all simulated events (blue) and for events in the FV (red). (Bottom) Distribution of the total number of PEs released per event, for all simulated events (blue) and for events in the FV (red).

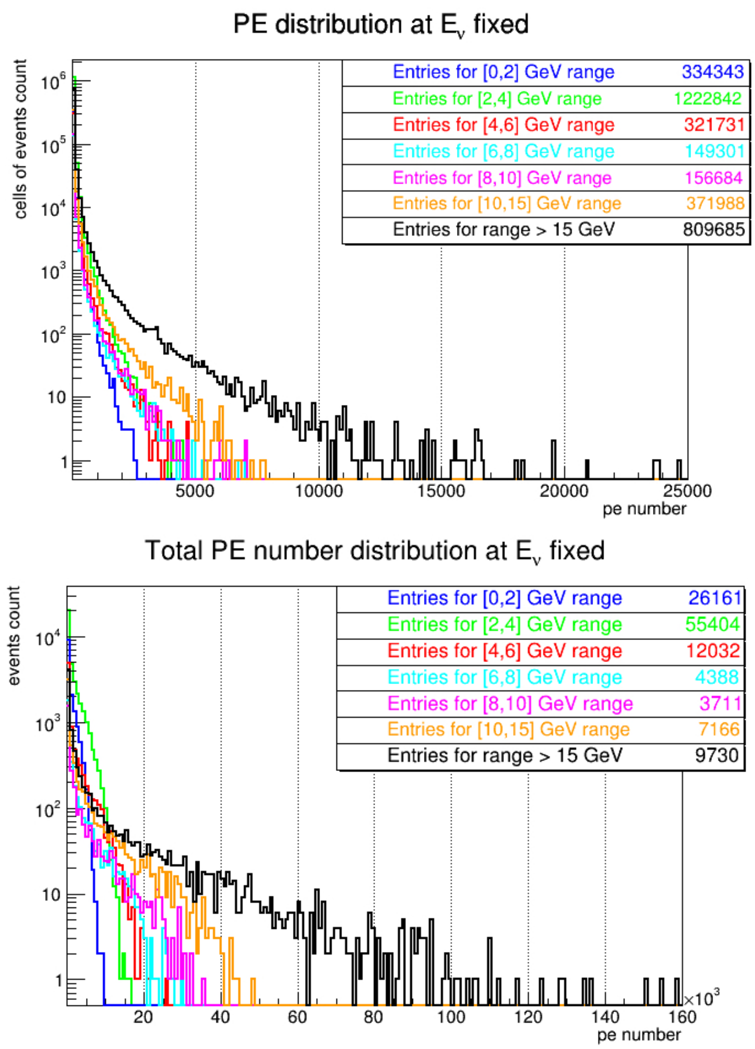

Figure 1.14: (Top) Distribution of the number of PEs released per cell and per event, for all simulated events and for different neutrino energy ranges. (Bottom) Distribution of the total number of PEs released per event, for all simulated events and for different neutrino energy ranges.

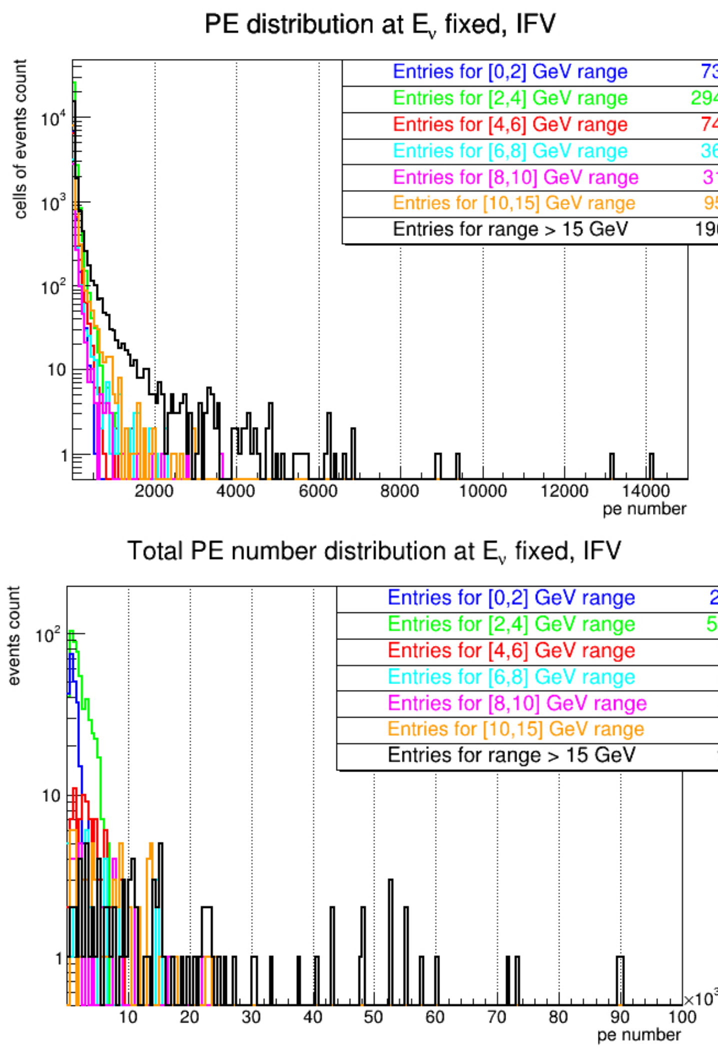

Figure 1.15: (Top) Distribution of the number of PEs released per cell and per event, for simulated events in the FV and for different neutrino energy ranges. (Bottom) Distribution of the total number of PEs released per event, for simulated events in the FV and for different neutrino energy ranges.

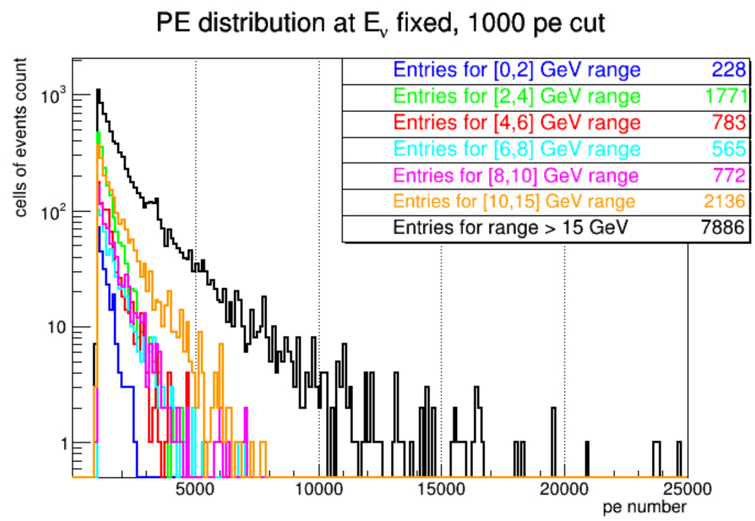

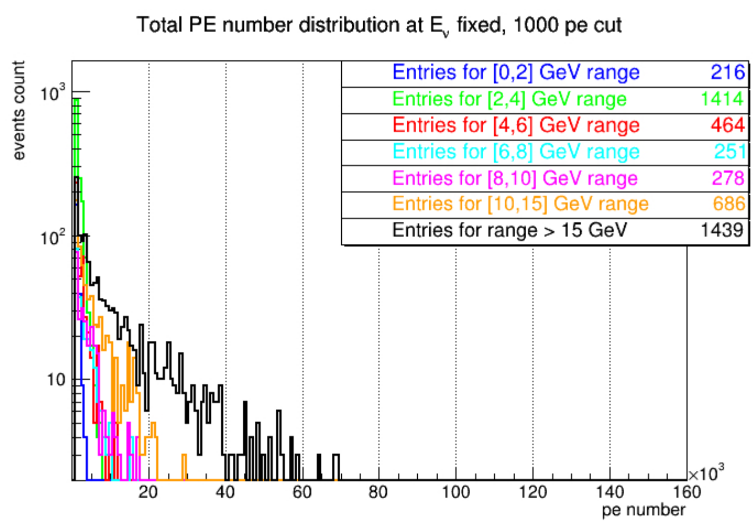

Figure 1.16: (Top) Distribution of the number of PEs released per cell and per event, for all simulated events and for different neutrino energy ranges. (Bottom) Distribution of the total number of PEs released per event, for all simulated events and for different neutrino energy ranges. Entries correspond only to cells above a threshold of 1000 PEs.

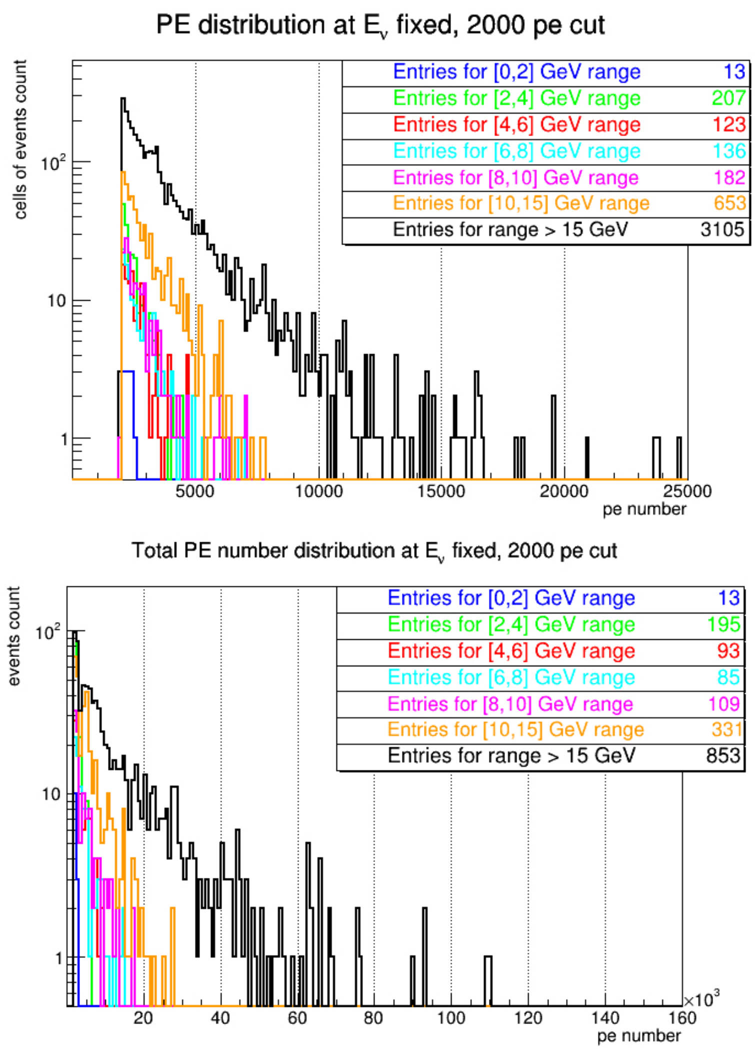

Figure 1.17: (Top) Distribution of the number of PEs released per cell and per event, for all simulated events and for different neutrino energy ranges. (Bottom) Distribution of the total number of PEs released per event, for all simulated events and for different neutrino energy ranges. Entries correspond only to cells above a threshold of 2000 PEs.

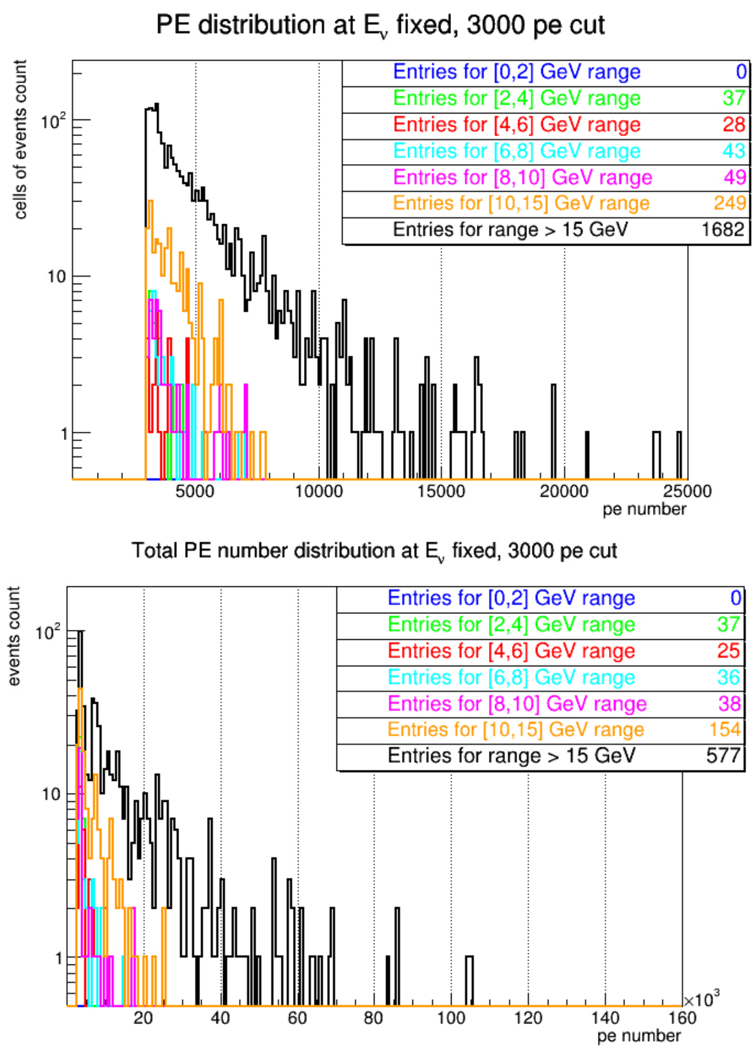

Figure 1.18: (Top) Distribution of the number of PEs released per cell and per event, for all simulated events and for different neutrino energy ranges. (Bottom) Distribution of the total number of PEs released per event, for all simulated events and for different neutrino energy ranges. Entries correspond only to cells above a threshold of 3000 PEs.

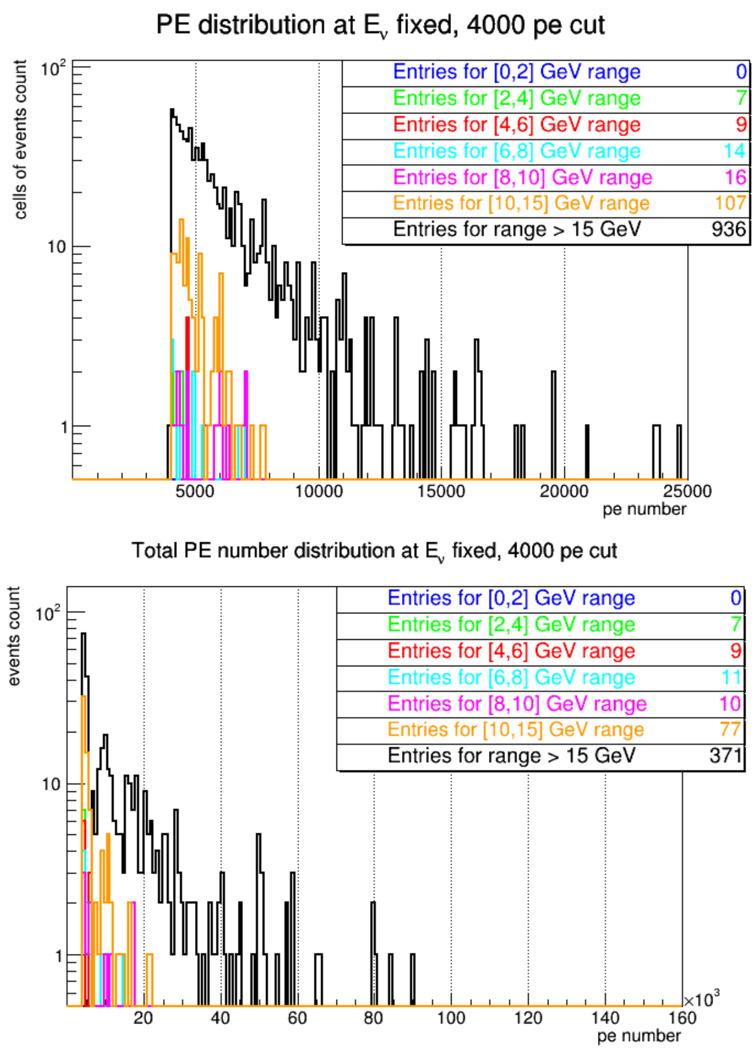

Figure 1.19: (Top) Distribution of the number of PEs released per cell and per event, for all simulated events and for different neutrino energy ranges. (Bottom) Distribution of the total number of PEs released per event, for all simulated events and for different neutrino energy ranges. Entries correspond only to cells above a threshold of 4000 PEs.

a fraction of 2.58% or 0.49% of the events has at least one cell above the threshold of 1000 or 2000 PE, respectively, is reached. The values for these thresholds and for the others are shown in Tab. 1.2, while Tab. 1.3 reports also the fraction of cells hit above the mentioned thresholds for all events.

Table 1.2: Fraction of events with at least one cell above PE threshold in the neutrino energy range 0-10 GeV.

PE threshold	Fraction of events (%)
1000	2.58
2000	0.49
3000	0.13
4000	3.64×10^{-2}

Table 1.3: Fraction of hit cells above PE threshold in the neutrino energy range 0-10 GeV.

PE threshold	Fraction of hit cells (%)
1000	0.19
2000	3.0×10^{-2}
3000	7.2×10^{-3}
4000	2.1×10^{-3}

The number of PEs ranges from 1 to 25000; however this upper limit corresponds to events with an energy range beyond the scope of interest for DUNE oscillation analyses. The minimum number of PEs considered in the simulation is chosen to be 3 to avoid background noise, while the maximum number that could be considered of interest is 1000 or 2000 PEs, as discussed in the following. These numbers set the dynamic range for the PMT signals, that has to match the readout electronics. In particular, a linearity of the electronics for signals up to 2000 PEs would guarantee a linear response for more than 99.5% of the events, as can be inferred from Tab. 1.2.

The next step corresponds to evaluate the probability that a single cell is hit in a neutrino interaction event. To extract this information from the MC sample the cell occupancy plots are evaluated for the modules of the two endcaps and the 24 modules of the barrel, using the ID cell code for the barrel $\mathrm{ID}_{barrel} = 1000 \times mod + 100 \times plane + column$ where *mod* is the module index going from 0 to 23, *plane* is the plane index going from 0 to 4, and *column* is the column index going from 0 to 11. For the two endcaps, the module numbers are 30 for endcap A and 40 for endcap B while the columns are grouped by the plane they belong to. Fig. 1.20 shows the occupancy plots of a module of the barrel and of the two endcaps.

It is noteworthy that the cells belonging to the fifth plane make the largest contribution to the occupancy plot. This is in part due to the fact that planes do not have equal thickness, in fact plane 5 is thicker than the others, namely 5.2 cm against 4.4 cm. Partly it is due to the more probable neutrino interaction in the iron yoke than the FV, with more secondary particles entering ECAL from the fifth planes.
From the occupancy plot it is possible to estimate the probability that a cell is hit in a neutrino

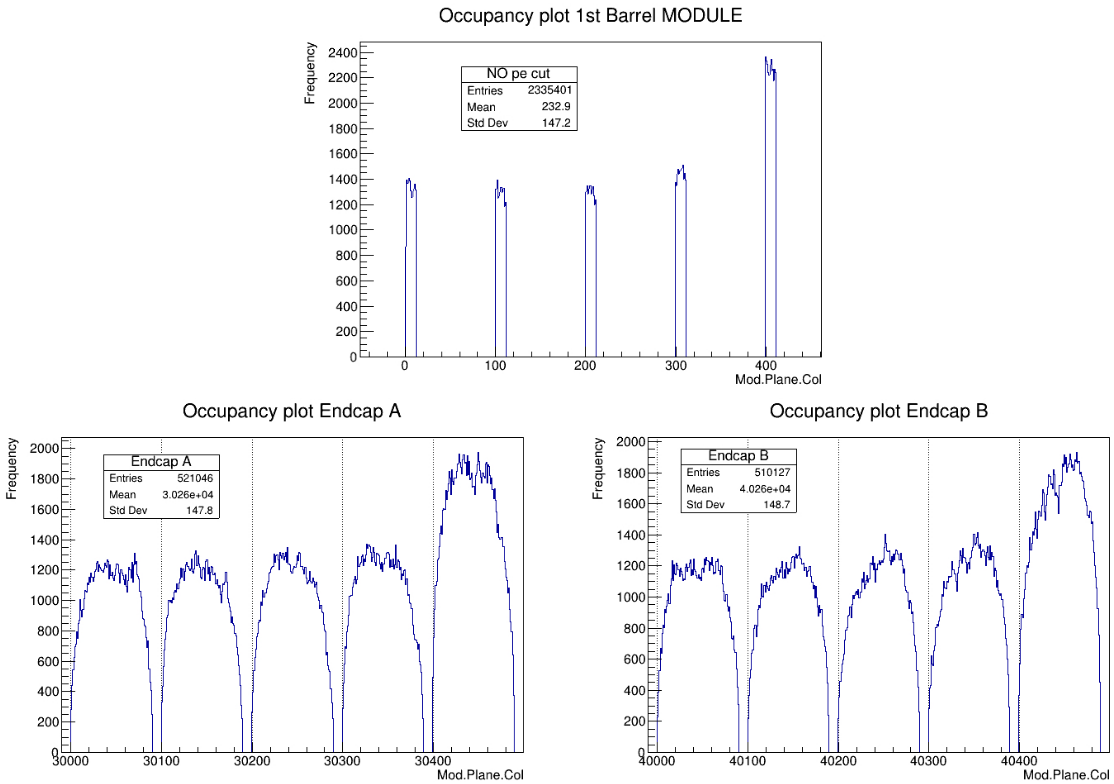

Figure 1.20: (Top) Number of hits for each cell (occupancy plot) of one ECAL barrel module as an example (# 1). (Bottom) Number of hits for each cell (occupancy plot) of ECAL End-Cap A modules (left), and End-Cap B modules (right). Each bin in the histograms represent a cell. Cells in the fifth plane have in average more hits than in other planes.

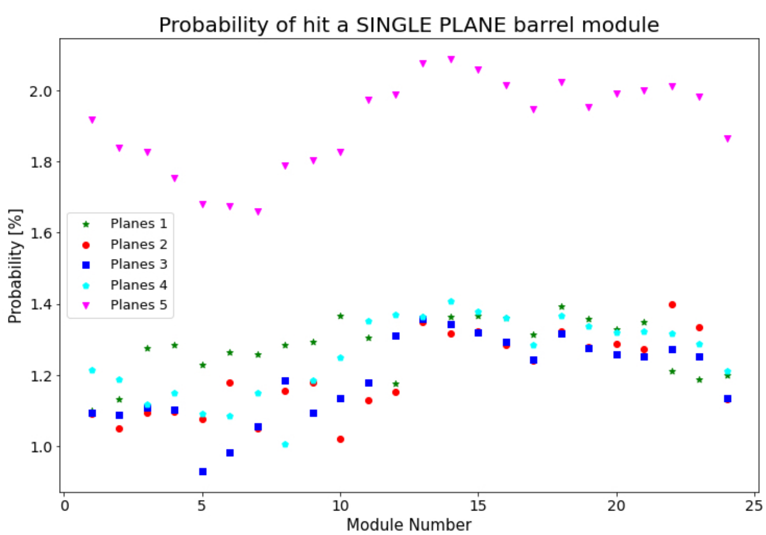

Figure 1.21: Probability of hitting a cell in a barrel module, separately for the 24 modules and the 5 planes.

interaction event. Fig. 1.21 shows the probabilities for all 24 modules of the barrel separately for planes 1-5 and averaged for the cells of each plane.

The average probabilities for the first 4 planes and for plane 5 for all 24 barrel modules are easily evaluated. The same analysis is performed for the Endcaps A and B. The results are summarized in Tab. 1.4:

Table 1.4: Average probabilities that a cell is hit in a neutrino interaction event.

ECAL	planes 1-4	plane 5	planes 1-5
Barrel	1.23%	1.91%	1.37%
Endcap A	0.80%	1.21%	0.88%
Endcap B	0.79%	1.15%	0.86%

A global weighted average is calculated using as weights the number of cells of the barrel (1440), the Endcap A (500) and the Endcap B (500):

$$P_{ECAL} = \frac{1440 \cdot P_{\text{barrel}} + 500 \cdot (P_{\text{EndcapA}} + P_{\text{EndcapB}})}{2440} = 1.16\% \tag{1.6}$$

This single value for the probability that a cell is hit in a neutrino interaction event will be considered in the next section for the evaluation of the pile-up, therefore assuming that all cells have the same probability.

The beam time structure is reconstructed to simulate the time of the neutrino interaction event and calculate the pile-up probability that, given a PMT signal, a second signal arrives within a fixed time window (TW) after the first signal. The times of N interactions per spill (in average N=84 with 1.2 MW beam) are extracted uniformly between 0 and 9.6 μs. The time difference between two consecutive interactions is calculated for all spills, following an exponential distribution with $\tau_{\text{spill}} = 114$ ns. From this, the distribution of time differences for a single cell with a probability to be hit of $P_{cell} = 1.16\%$ is evaluated, and then the pile-up probabilities for different time windows are also evaluated, TW = 50, 100, 150, 200 ns, as shown in Tab. 1.5, where the cases of higher $P_{cell} = 1.5\%, 2.0\%$ are also considered. The effect of the time spread of the cell hits within a single neutrino interaction events is negligible on the time scale of the spill, as shown in Tab. 1.6.

Table 1.5: Pile-up probability of PMT signals (without neutrino event time smearing).

Time window [ns]	$P_{ECAL} = 1.16\%$	$P_{ECAL} = 1.5\%$	$P_{ECAL} = 2.0\%$
50	0.67%	0.90%	1.28%
100	1.33%	1.81%	2.52%
150	1.95%	2.71%	3.72%
200	2.59%	3.58%	4.87%

Since the KLOE detector had high demands on time and energy resolutions, a high performance front end electronics (FEE) was required. This task lays on the base of the PMTs. This consists of a high voltage (HV) divider and a preamplifier which must have low noise, high bandwidth and high output dynamic range in order to avoid distortion of the fast pulses from the photomultiplier.

Table 1.6: Pile-up probability of PMT signals (with neutrino event time smearing).

Time window [ns]	$P_{ECAL} = 1.16\%$	$P_{ECAL} = 1.5\%$	$P_{ECAL} = 2.0\%$
50	0.64%	0.86%	1.36%
100	1.32%	1.71%	2.56%
150	1.91%	2.60%	3.78%
200	2.52%	3.48%	4.93%

The HV divider has a cathode that is grounded and a positive voltage is applied to the anode: this allows to reduce the noise associated with the charging surfaces in contact with the phototube envelopes. The voltage of the first stage is 300 V and is independent of the high voltage supplied, while the remaining high voltage is divided among the other 15 stages (see Fig. 1.22). For example, a typical divider current for a high voltage of 2000 V is 150 μA. To increase the linearity of the HV divider, the last five resistors are used in conjunction with capacitors to reduce the voltage fluctuations due to current spikes.
The preamplifier is necessary for the base because it provides an optimal coupling to the PMT and drives the cable that carries the signal to the next stage. It is a three-transistor transimpedance device AC coupled to the PMT, with a conversion gain $G_C = 247$ V/A (see Fig. 1.23). A high gain-bandwidth product and a high dynamic range are required both to avoid distortion of the signal edges and to keep the non-linearity below 0.2% over the whole range of interest for KLOE. The first stage is a common base with low input impedance. The second stage (common emitter) is necessary to increase the open loop gain; the third stage is an emitter follower and drives a 50 Ω coaxial cable. A typical PMT signal produced by the PMT-base is shown in Fig. 1.24.

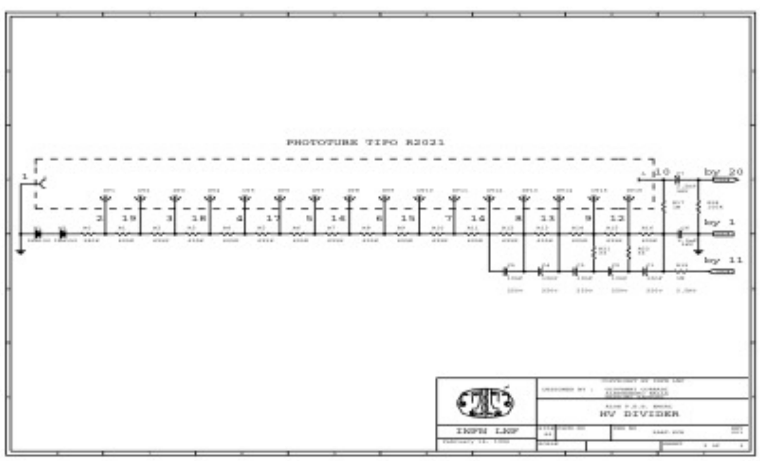

Figure 1.22: Electrical schematic of the HV divider in the PMT-base.

This signal can be approximated to a triangular pulse with base $\Delta t \sim 14$ ns and height $V = V^{\rm out}_{\rm peak}$. Until the preamplifier works within its linearity range the output voltage signal has the same shape of the input current signal and its amplitude is given by $V^{\rm out}_{\rm peak} = I^{\rm in}_{\rm peak} \times G_C$.

The dynamic range in terms of N_{PE} and the PMT gain $G_{\rm PM}$ can be evaluated in KLOE using the following constraints:

1. Minimum discriminator threshold $V_{TH} = 5$ mV

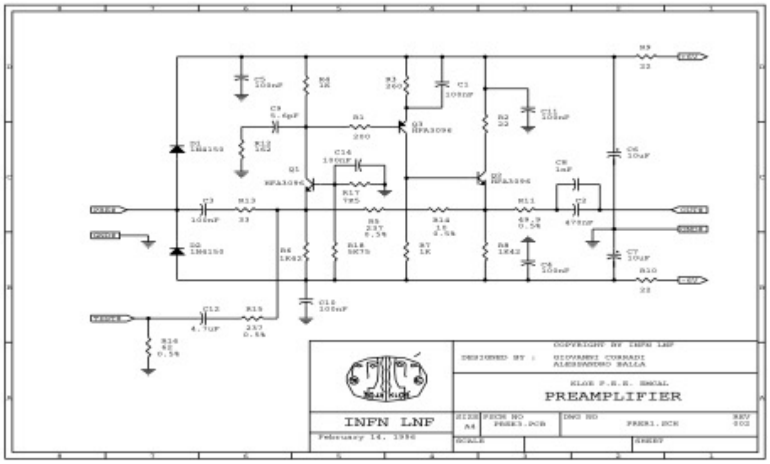

Figure 1.23: Electrical schematic of the preamplifier in the PMT-base.

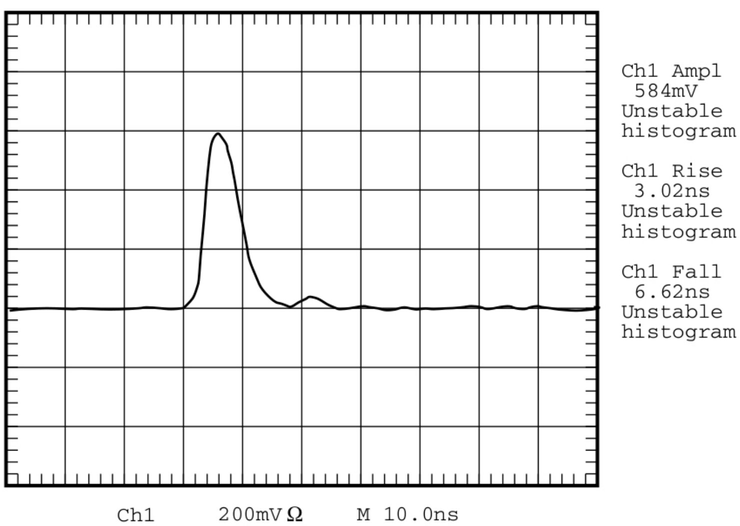

Figure 1.24: Typical signal from the PMT-base.

2. Preamplifier linearity (within 0.2%) range = [0, 4.7] V; $V_{preamp}(max) = 4.7$ V;

3. preamp transimpedance gain $G = 250\ V/A$; $I_{peak}(max) = V_{preamp}(max)/G = 19$ mA;

4. max signal charge $Q(\text{max}) = 133$ pC (triangle approx.);
   from $Q = e \cdot N_{pe} \cdot G_{PMT}$ follows $(N_{PE} \cdot G_{PMT})(\text{max}) = 83 \times 10^7$;

5. 1 PE/MeV at cell center; ~ 1.8 PE at the end;

6. max energy release in one cell: 410 MeV, implying $N_{PE}(\text{max})$ of $\mathcal{O}(1000)$.

7. $G_{TOT} = G_{PMT}\ G_{\text{preamp}}$ with $G_{\text{preamp}} = 2.5$

8. 12 m long cable attenuation: $C_{ATT} = 0.74$

9. maximum HV for divider is 2300 V; typical HV 1700-1800 corresponding to $G \sim 1 - 3 \times 10^6$

10. MAX single pulse amplitude at the discriminator/digitizer input is:
    $V_{dis}(max) = V_{preamp}(max) \cdot 0.5 \cdot C_{ATT} = 1.74\ V$

11. (signal ampl) $= V_{dis}(max)/N_{PE}(max)$
    $N_{PE}(min) = V_{TH}/(\text{signal ampl})$
    $N_{PE}(max)/N_{PE}(min) = V_{dis}(max)/V_{TH}$

From these constraints there follow possible choices of $N_{PE}(max)$ and G_{PM} as reported in Tab. 1.7. In KLOE the effective choice provided $N_{PE}(max) \sim 1000$ and $G_{PM} \sim 2 \times 10^6$.

Table 1.7: Maximum and minimum number of PEs given by a calorimeter readout cell as a function of the gain $G_{tot} = G_{PMT} \times G_{preamp}$.

$\boldsymbol{G_{PMT}}$ ($\times 10^5$)	G_{TOT} ($\times 10^6$)	N_{PE}(max)	signal amplitude (mV/PE)	N_{PE}(min) $V_{TH} = 5$ mV	MeV at module center
4.2	1.04	$\sim$ 2000	0.87	$\sim$ 6	6.0
5.5	1.38	$\sim$ 1500	1.16	$\sim$ 4	4.0
8.3	2.1	$\sim$ 1000	1.74	$\sim$ 3	3.0
10	2.5	$\sim$ 800	2.18	$\sim$ 2	2.0

As mentioned above, the preamplifier in the PMT-base provides an optimal coupling to the PMT and drives the cable carrying the signal to the next stage. A high gain bandwidth and an high dynamic range are required both to avoid distortions of the signal rise edges and to maintain the non-linearity below 0.2% in the whole range of interest. As $V_{dis}(max)$ depends directly on $V_{preamp}(max)$, the linearity of the preamplifier has been tested with the specific goal of investigating the possibility of slightly extending the dynamic range of signals by increasing $V_{preamp}(max)$, while keeping linearity still at an acceptable level, e.g. 1%. The test has been performed on a preamplifier using the test input specifically modified to get unity voltage gain and a total input resistance of 50 Ω.

The preamplifier response has been characterized in two different ways. First a square pulse at 1 MHz was generated using the Tektronix AFG 3252 signal generator, with an amplitude of −5 V and a width of 30 ns. Subsequently, the signal was passed through two calibrated attenuators in series in order to modulate the input voltage to the preamplifier. Then the input voltage, the output voltage, and the integral of the output voltage (which represents the charge) were measured with an oscilloscope LeCroy HDO6104. The results are shown in Figs. 1.25. The output saturation is clearly visible at an output value of $\sim 3.4\ V$. A linear fit to the integrated charge of the output signal Q_{int} vs input voltage V_{in} is performed and showed in Fig. 1.26.

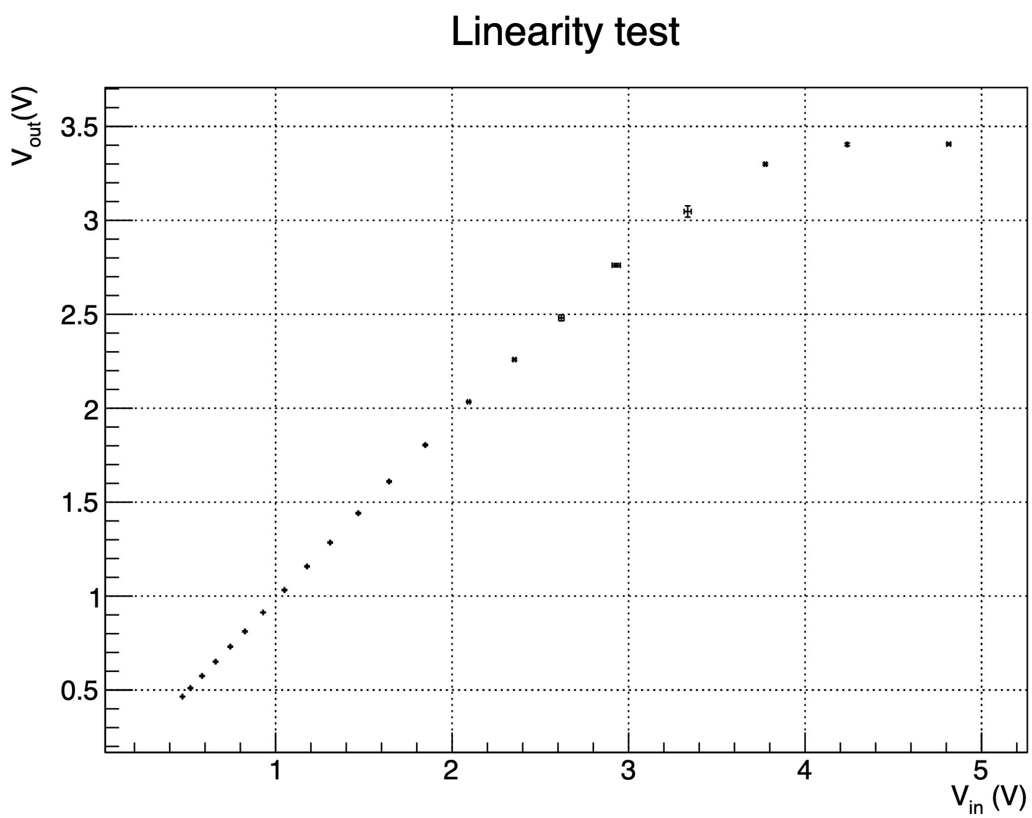

Figure 1.25: Preamplifier linearity test, showing output voltage V_{out} vs input voltage V_{in}.

To better understand the linearity of the amplifier, the linearity of the experimental setup chain was studied by bypassing the amplifier and inputting the same signal into the oscilloscope. The residuals of the data without the preamplifier were then subtracted from the residuals of the data with the preamplifier included in the chain. The residuals after this operation are shown in Fig. 1.27.

From the results of this test it can be concluded that by accepting the linearity of the preamplifier at 1% level, $Vpreamp(max)$ can be extended of $\sim 15\%$, from 4.7 V to 5.4 V, corresponding to

$$V_{dis}(max) = V_{preamp}(max) \cdot 0.5 \cdot C_{ATT} = 2.0\ V\ . \tag{1.7}$$

Assuming to have a very low noise environment as in KLOE and to lower the minimum discriminator threshold to $V_{TH} = 2.5\ mV$, suitable choices for the dynamic range of signals in SAND are

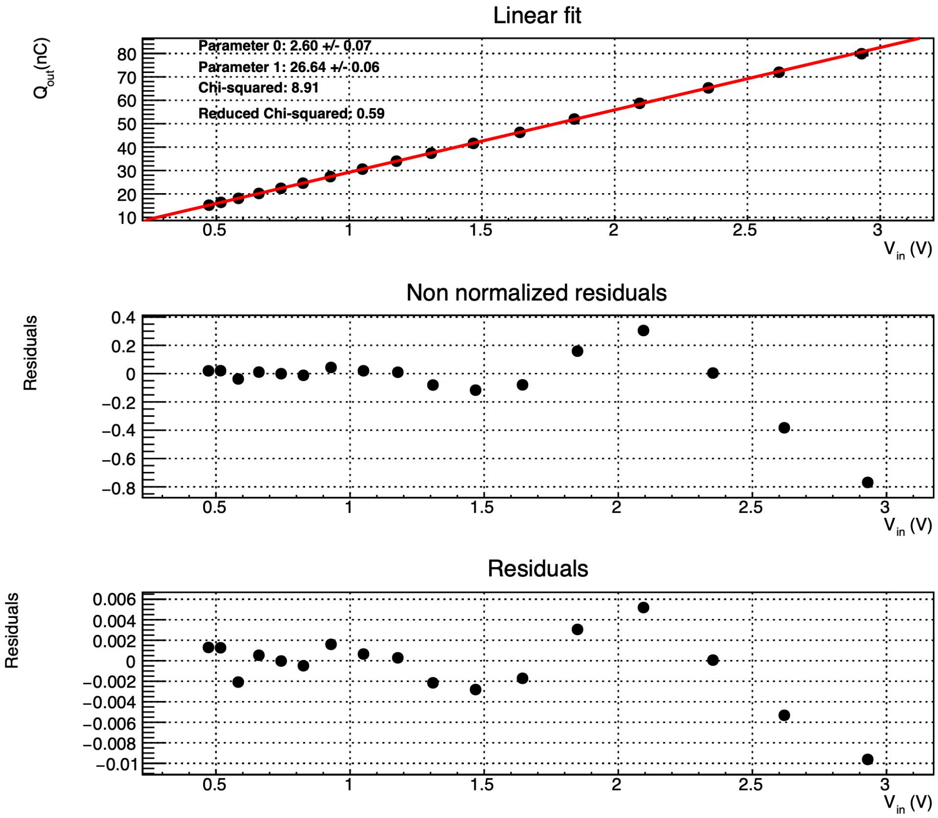

Figure 1.26: Preamplifier integrated charge linearity test, showing integrated charge of the output signal Q_{int} vs input voltage V_{in}.

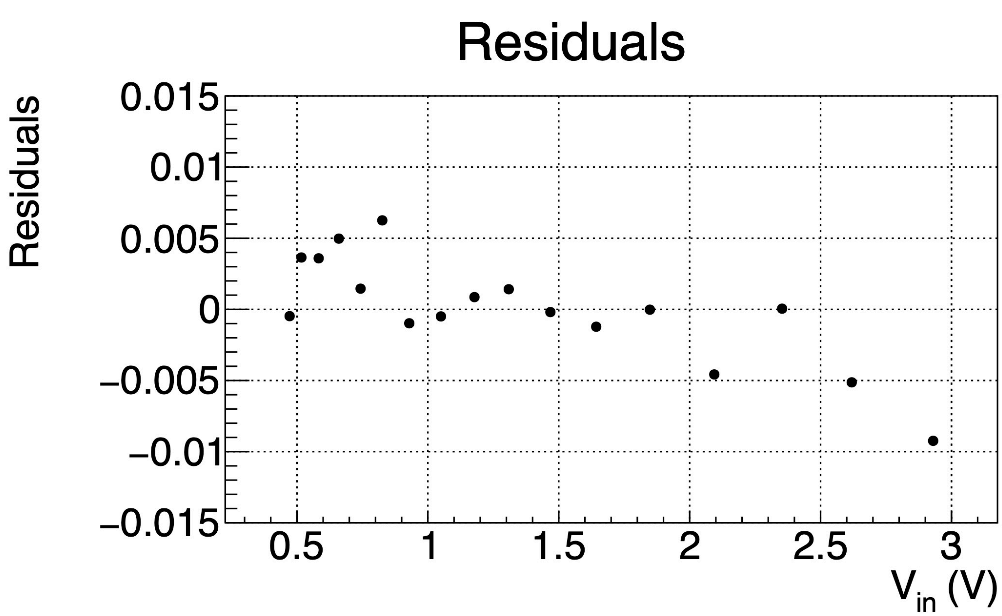

Figure 1.27: Normalized residuals to the setup linearity.

obtained, as shown in Tab. 1.8. Different dynamic ranges can be implemented changing G_{PMT}: the final choice should be a compromise between an affordable level of events with energy saturated cells, depending on N_{PE}(max), and an acceptable neutron detection efficiency, depending on N_{PE}(min).

It is worth noting that the use of a preamplifier lowers the effective PMT gain and HV values with a beneficial effect on PMT lifetime.

Table 1.8: Maximum and minimum number of PEs given by a calorimeter readout cell as a function of the gain $G_{tot} = G_{PMT} \times G_{preamp}$.

$\boldsymbol{G_{PMT}}$ ($\times 10^5$)	G_{TOT} ($\times 10^6$)	N_{PE}(max)	signal amplitude (mV/PE)	N_{PE}(min) $V_{TH} = 2.5$ mV	MeV at module center
4.8	1.2	~ 2000	1.0	~ 3	3.0
6.4	1.6	~ 1500	1.3	~ 2	2.0
9.5	2.4	~ 1000	2.0	~ 1	1.0

The preamplifier linearity with a special focus on the saturation regime has been studied also directly with PMT signals. Two PMTs were connected to a CAEN SP5601 Led driver using scintillating fibers (see Fig. 1.28). For each position of the light attenuator of the Led Driver, measurements were taken at two different high voltages for the two PMTs. Using a lower voltage ensured operation and the study of the system in the linear response region of the preamplifier. Subsequently, a higher voltage was used to study the system in the saturation regime of the preamplifier. The HV values used to characterize the response in the two regions for the two PMTs are reported in Tab. 1.9.

Table 1.9: HV values for the study of the PMT signals in the linear and saturation regimes of the preamplifier.

	PMT1 (V)	PMT2 (V)
Linearity regime	1700	1650
Saturation regime	2100	1900

The scan with the Led Driver light attenuator spans the two regimes and the attenuation scales have been inter-calibrated and coherently combined in order to have a unique attenuation scale factor, with unity corresponding to the maximum intensity. The result is shown in Fig. 1.29 for the output voltage and in Fig. 1.30 for the integrated charge vs the attenuation scale factor.

Since it was observed that the integrated charge exceeds the expected linear behavior when the attenuation scale factor approaches unity, instead of saturating, the trend of the full-width at half-maximum of the signals as a function of the attenuation was studied. The measurements are presented in Fig. 1.31. They are compared with the expected behavior for the PMT signal in a triangular model approximation with saturation implemented for the amplitude but without a corresponding increase of the signal width, as observed in the data. This phenomenon is fully clarified directly looking at the PMT signals at the oscilloscope (see Fig. 1.32). The time baseline

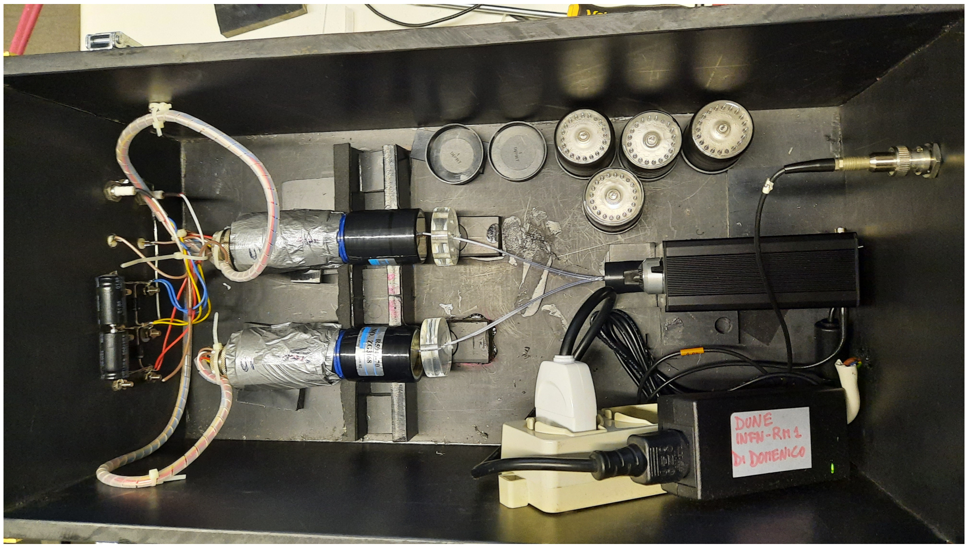

Figure 1.28: Experimental setup for the linearity test with PMTs.

is distorted during saturation. The recovery time from saturation to linear regime depends on the input signal amplitude. In conclusion the input information is not fully lost during the saturation regime. The "over-linearity" of the integrated charge, or the signal width increase vs the input signal amplitude could be exploited to characterize signals beyond the preamplifier saturation regime, and measure their amplitude also in this region.

1.1.5.2 FEE and data acquisition (DAQ)

In general three possible schemes can be envisaged for the ECAL FEE:

1. A digitizer with a sampling rate of $\sim 1\ GS/s$; this option is rather expensive, so a compromise with a slower digitizer with a sampling rate of $\sim 128\ MS/s$ complemented with a signal slow shaper;

2. a picoTDC based on the ASIC developed at European Organization for Nuclear Research (CERN) coupled with double (or more) threshold discriminator to reconstruct the amplitude of the signal with the Time-over-Threshold (ToT) technique;

3. a more conventional solution with the signal split in two paths: a fast one to a TDC (or picoTDC) for the time measurement, and a slower one to a QDC for the integrated charge measurement.

Possible solutions for the FEE that should constitute a good compromise between cost and performance are being investigated in collaboration with CAEN S.p.A. . In particular, several tests have been performed on the picoTDC option using the commercial CAEN board DT5203 with a double threshold discriminator A5256.

A preliminary test was conducted by CAEN using a signal function generator AFG3252. The output from the signal generator was sent to the picoTDC installed on a FERS (DT5203+A5256) through a calibrated attenuator, in order to vary the amplitude of the signals in a precise and

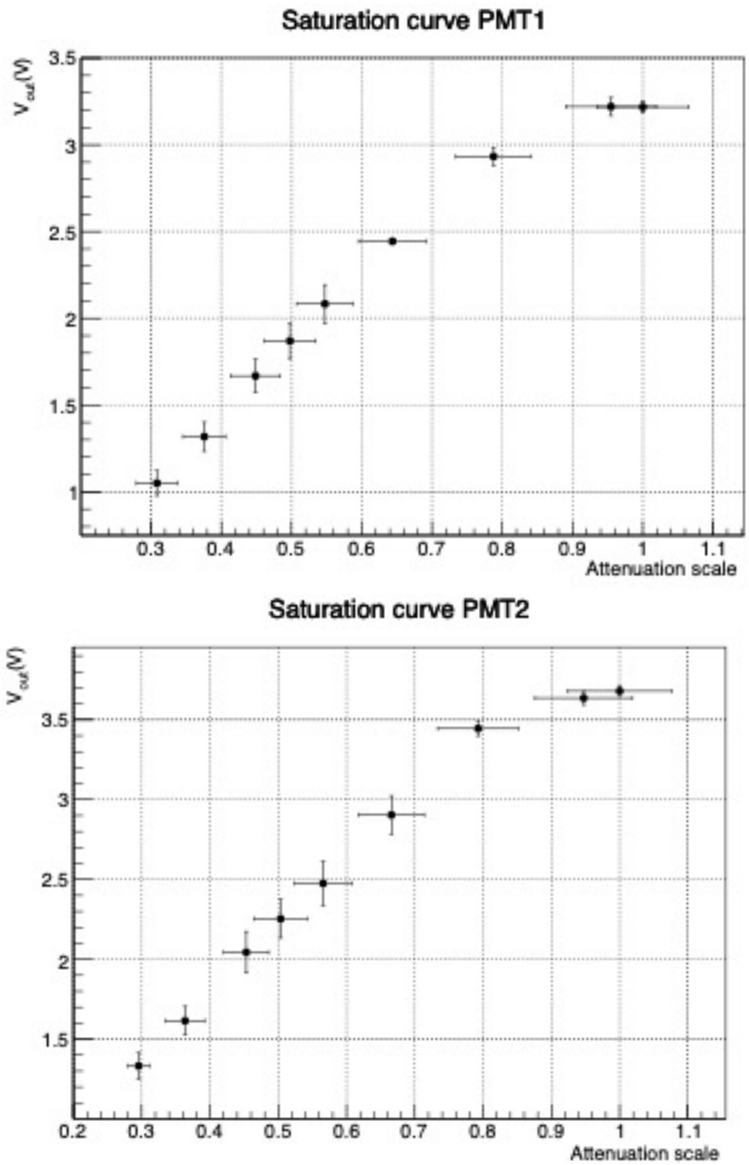

Figure 1.29: Preamplifier linearity test with PMT signals, PMT1 (Top) and PMT2 (Bottom) showing output voltage V_{out} vs attenuation scale factor.

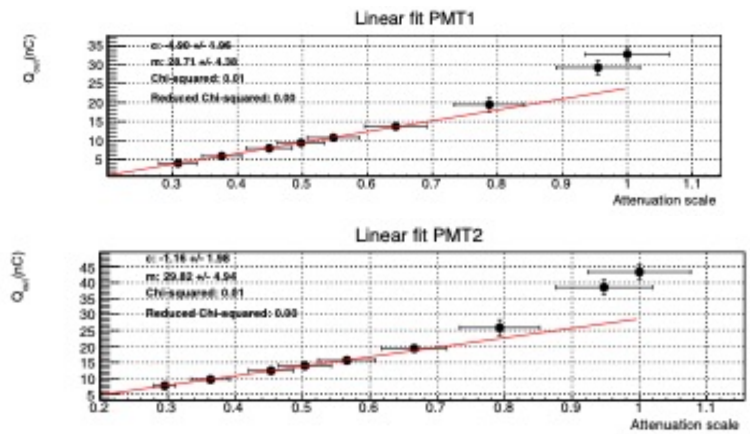

Figure 1.30: Preamplifier linearity test with PMT signals, PMT1 (Top) and PMT2 (Bottom) showing integrated charge Q_{int} vs attenuation scale factor.

controlled way, as shown Fig. 1.33. At 0 dB of attenuation, the amplitude was set to 3.85 V with a rise time of 2.5 ns. The low threshold was set to 5 mV and the high threshold to 300 mV.

First, calibration data for the ToT and ΔT (Walk) at different amplitudes (from 0 to 52 dB, in 3 dB steps) were acquired. Then, pulses were acquired at 6 different amplitudes spanning a 50 dB dynamic range, completely independently on the calibration data. The walk effect caused approximately a 2 ns spread in ΔT, resulting in 6 separate peaks. ΔT was corrected using ToT data with a 5^{th} order polynomial fit of the ToT-ΔT points collected at a lower threshold (5 mV). The corrected ΔT distribution shows a single peak. Using this correction a time resolution $\sigma_{\Delta T} \sim$ 18ps over the full 50 dB dynamic range was achieved.

Finally, using the calibration curve $ToT - A$, the amplitude A was reconstructed. The achieved resolution σ_A on the different reconstructed amplitude peaks, ranging from 12 mV to 3850 mV, is reported in Tab. 1.10.

Table 1.10: Resolution on reconstructed amplitudes from ToT.

A (mV)	σ_A (%)
12.2	1.1
38.0	3.1
121.8	3.3
385.9	0.1
1217.5	0.6
3850.0	0.8

A second test of the picoTDC has been done with PMT signals using the same set-up used to study the linearity of the preamplifier in the PMT-base, with two PMTs connected to a Led driver through scintillating fibers. In this case the output signal from the calibrated attenuator is split in two: one branch is sent to the picoTDC chain while the other is sent in input to a CAEN 730S 14-bit Digitizer module, as a reference measurement for the amplitude (see Fig. 1.34).

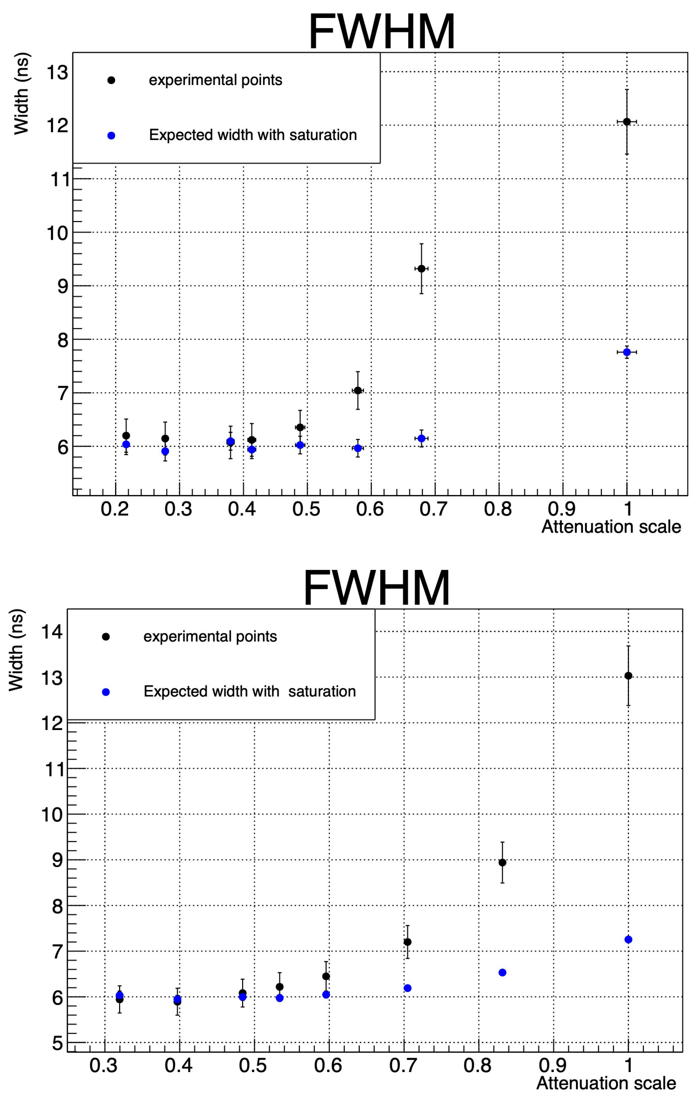

Figure 1.31: Behavior of the FWHM of the PMT1 signal (Top) and PMT2 (Bottom) vs attenuation scale factor. The expected behavior for the PMT signal in a triangular model approximation is also shown (blue points) with saturation implemented for the amplitude but without a corresponding increase of the signal width.

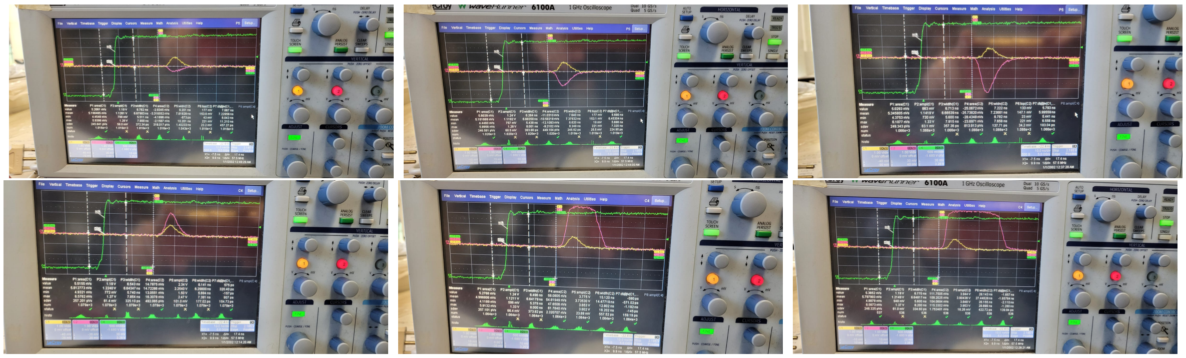

Figure 1.32: PMT signal (violet) at the oscilloscope without the preamplifier (Top) and with the preamplifier (Bottom) with the HV power supply at 1700 V (left), 1900 V (center) and]2100 V (right). The light intensity of the Led Driver is fixed at the maximum value for all cases shown in the pictures. The phenomenon of the preamplifier saturation and of the signal width increase is clearly visible in the bottom plots (violet signals) compared to the same signals from the PMTs without preamplifier. The ochre signals correspond to a reference PMT at fixed HV and with the preamplifier.

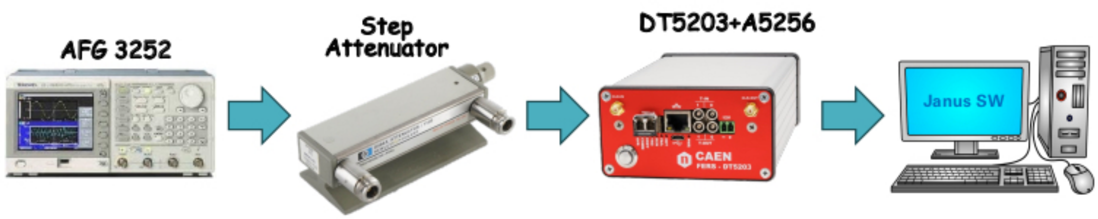

Figure 1.33: Set-up of the picoTDC test with signal function generator.

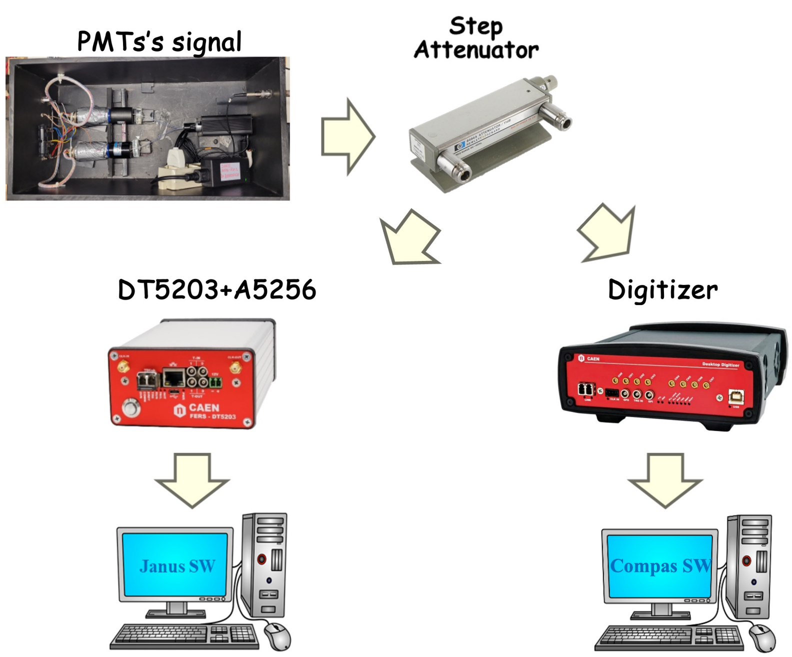

Figure 1.34: Set-up of the picoTDC test with PMT signals.

After performing a calibration similarly as in the previous case, data were acquired from 0 to 40 dB attenuation in 5 dB steps, with thresholds of 10 mV and 100 mV for the picoTDC, while no threshold was applied on the digitizer (synchronized with an external trigger).

As in the previous case, a fit of the Walk-ToT correlation plot was performed to correct the time resolution for both high and low thresholds, as shown in Fig. 1.35. The ΔT distributions before and after walk correction are shown in Figs.1.36 and 1.37 for the two thresholds. After the correction a fit to the ΔT peaks yields a global time resolution of $\sim$ 70 ps for the low threshold and of $\sim$ 60 ps for the high threshold.

The peak centered at 119.1 ns at the lower edge of the low threshold scan had an issue due to a secondary peak sometimes detected by the ToT measurement (see bottom plot of Fig. 1.36), and is not considered in the analysis. The time resolution results are summarized in Tab.1.11. All values are improved after walk correction. Even though the obtained resolutions are affected by the non-negligible light intensity fluctuations of the Led Driver (at the level of few percent of the PMT signal amplitudes) and it does not come as a surprise that they are worse than the value ($\sim$ 18 ps) obtained using the pulse generator test, nonetheless they are already better than the intrinsic ECAL time resolution considering its constant term.

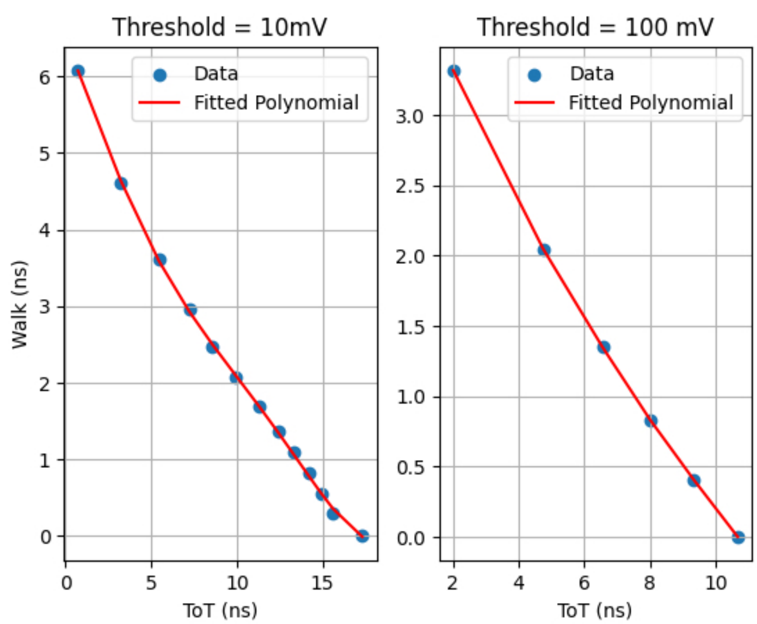

Figure 1.35: ToT-Walk picoTDC calibration curves; fit to calibration data points for low (left) and high (right) thresholds.

The ToT distributions were studied applying the calibration curves shown in Fig.1.38. In this way from the ToT histograms the corresponding amplitude histograms were derived for the two thresholds, as shown in Figs. 1.39 and 1.40.

The obtained reconstructed amplitude resolutions are presented in Tab. 1.12.

From these results it is evident that the best resolution for a given threshold is achieved for the closest amplitude to the threshold value, as expected even in a simple triangular PMT signal

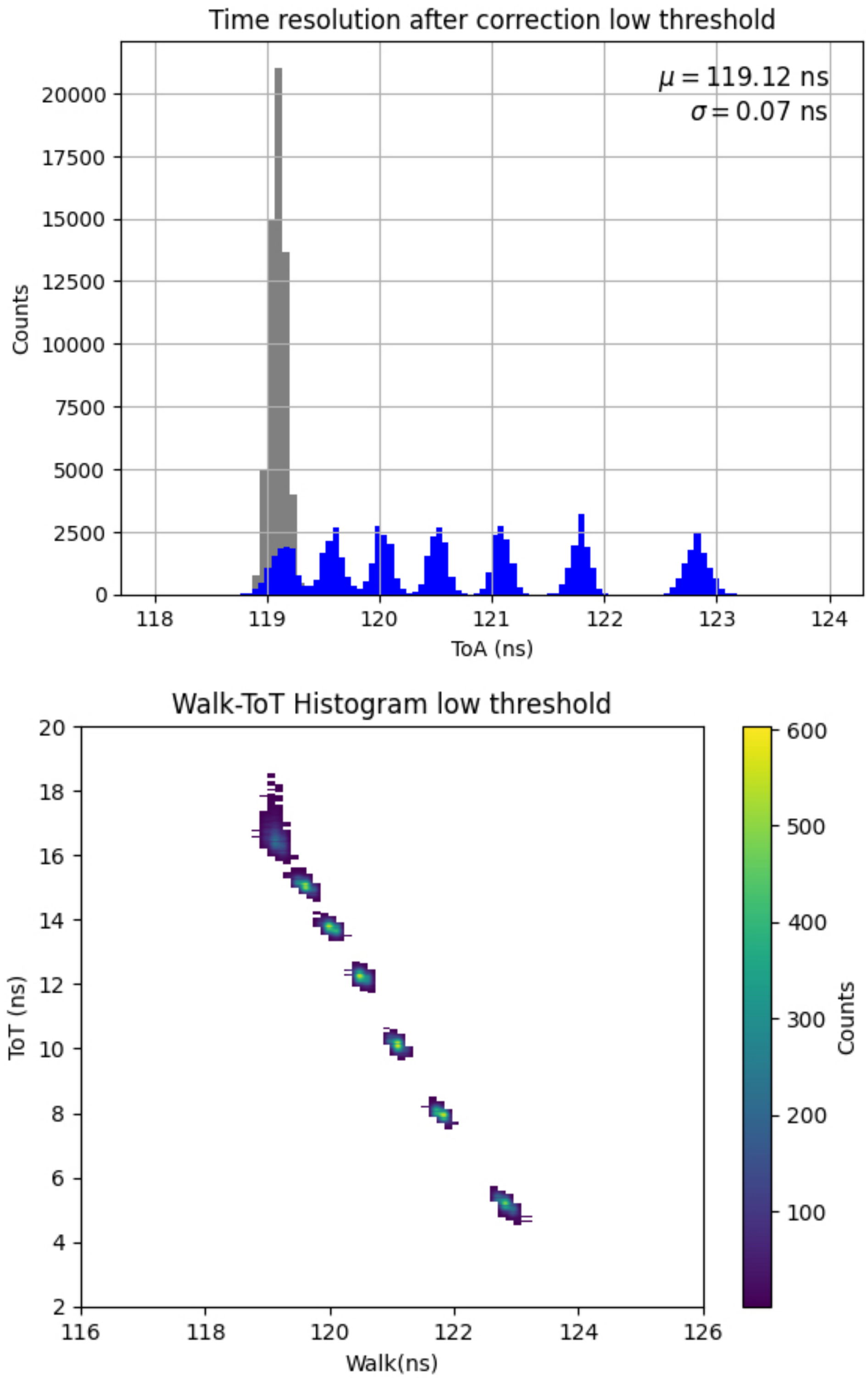

Figure 1.36: (Top) ΔT distributions before (blue peaks) and after (grey peak) walk correction for the low threshold. μ and σ values in the top-right corner of the plot refer to a gaussian fit to the grey distribution. (Bottom) ToT vs. ΔT correlation histogram before walk correction for the low threshold.

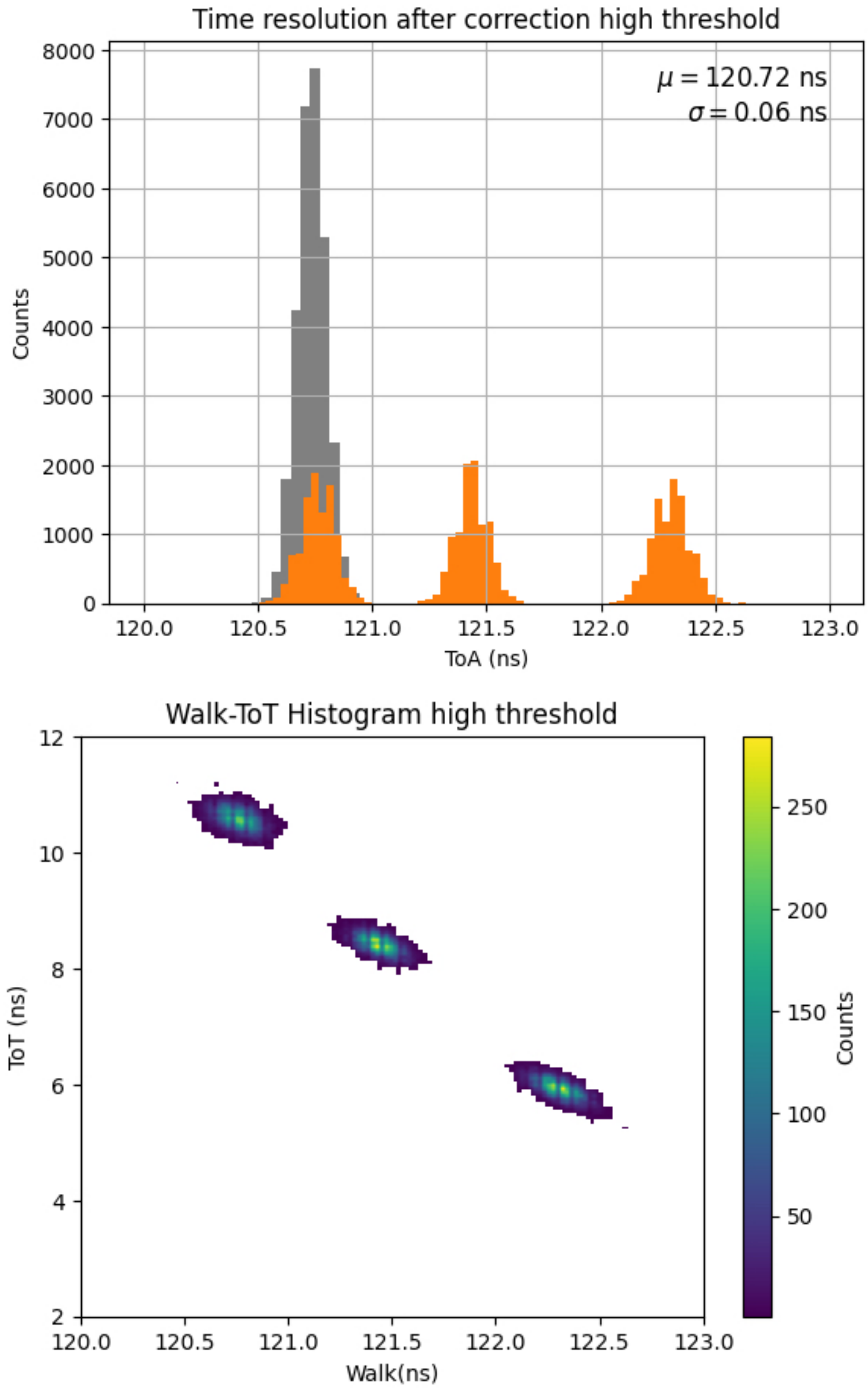

Figure 1.37: (Top) ΔT distributions before (ochre peaks) and after (grey peak) walk correction for the low threshold. μ and σ values in the top-right corner of the plot refer to a gaussian fit to the grey distribution. (Bottom) ToT vs. ΔT correlation histogram before walk correction for the low threshold.

Table 1.11: Time resolution on reconstructed ΔT before and after walk correction for low and high thresholds.

Threshold	mean ΔT (ns)	$\sigma_{\Delta T}$ (ps) before corr.	$\sigma_{\Delta T}$ (ps) after corr.
Low	119.1	-	-
Low	119.6	89	72
Low	120.0	81	71
Low	120.5	75	70
Low	121.1	74	65
Low	121.8	77	63
Low	122.8	100	71
High	120.8	74	69
High	121.4	72	61
High	122.3	82	62

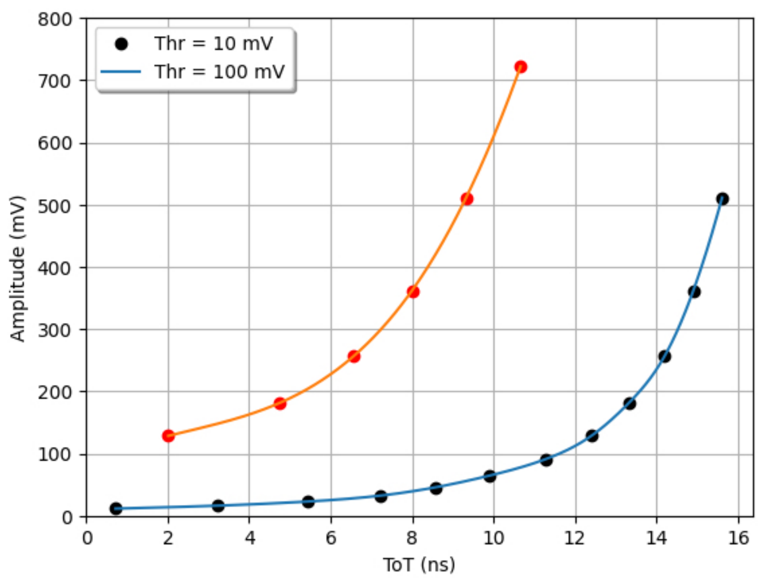

Figure 1.38: ToT-Amplitude picoTDC calibration curves; fit to calibration data points for low (blue) and high (ochre) thresholds.

Table 1.12: Resolutions on reconstructed amplitude from ToT for low and high thresholds.

mean A (mV)	σ_A (%) (low thr.)	σ_A (%) (high thr.)
722.0	-	4.2
406.0	8.0	3.8
228.3	5.9	3.2
128.4	5.4	-
72.2	4.0	-
40.6	4.0	-
22.8	3.2	-

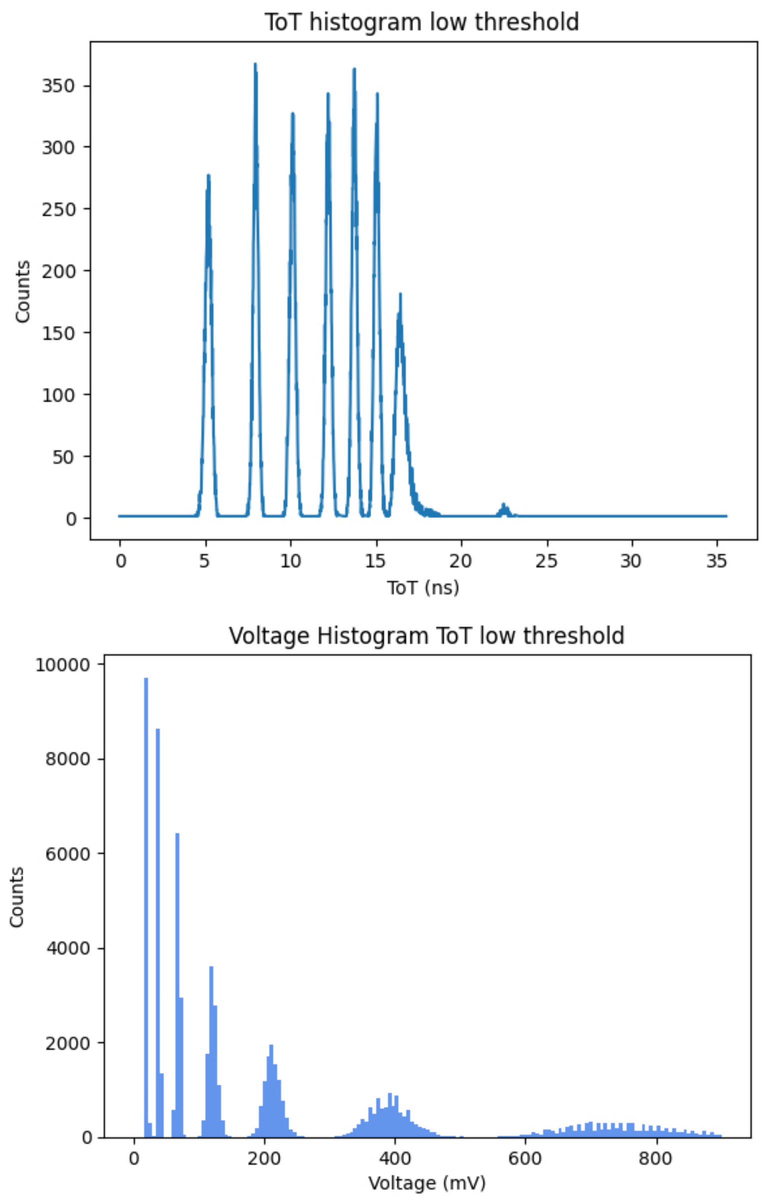

Figure 1.39: ToT distributions (Top) and amplitude from ToT after calibration correction (Bottom) for the low threshold.

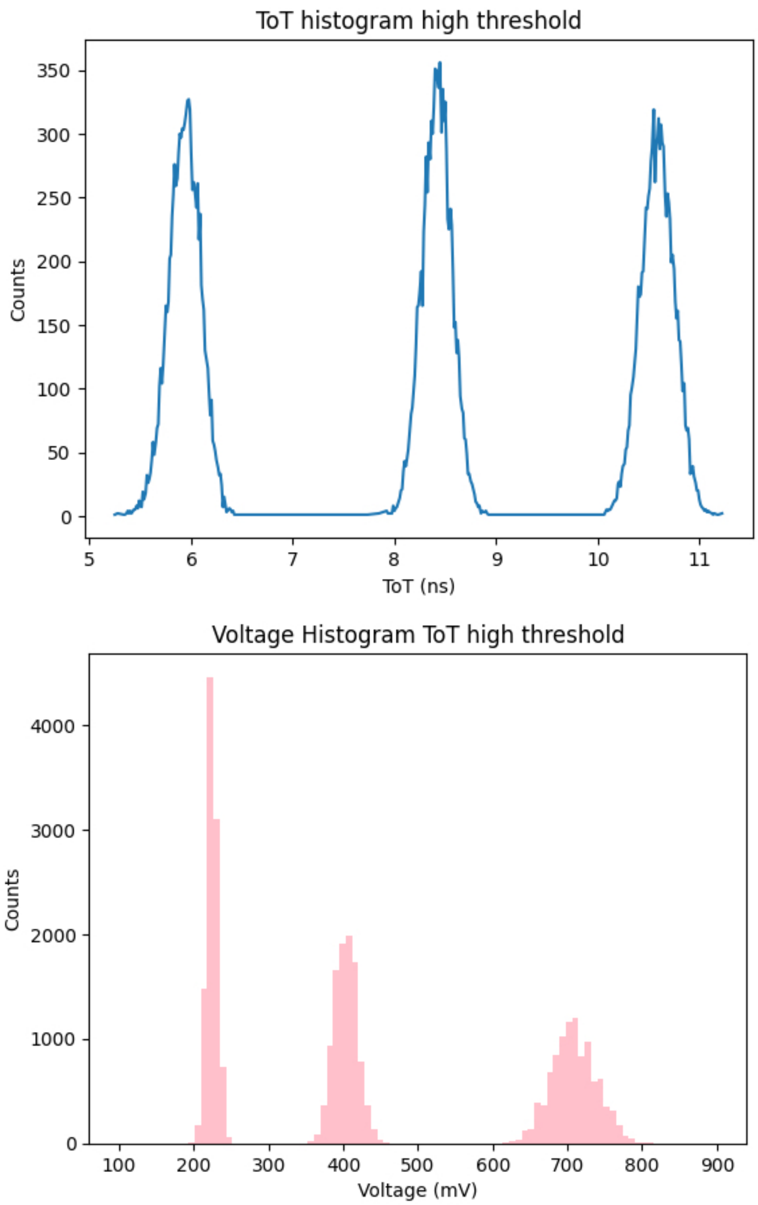

Figure 1.40: ToT distributions (Top) and amplitude from ToT after calibration correction (Bottom) for the high threshold.

model, with a progressive worsening of resolution for increasing amplitudes.

The best resolution results from the two thresholds scans were merged into a single histogram. This merged amplitude distribution from ToT and the amplitude distribution measured with the digitizer were then compared (see Fig. 1.41), and their correlation probed with a linear fit, as shown in Fig. 1.42. The fit indicates a good linearity, with a slope coefficient $c = 0.987 \pm 0.05$ compatible with unity within 2σ, and the intercept at zero $m = -1.78 \pm 0.65$ mV, indicating the presence of a small offset.

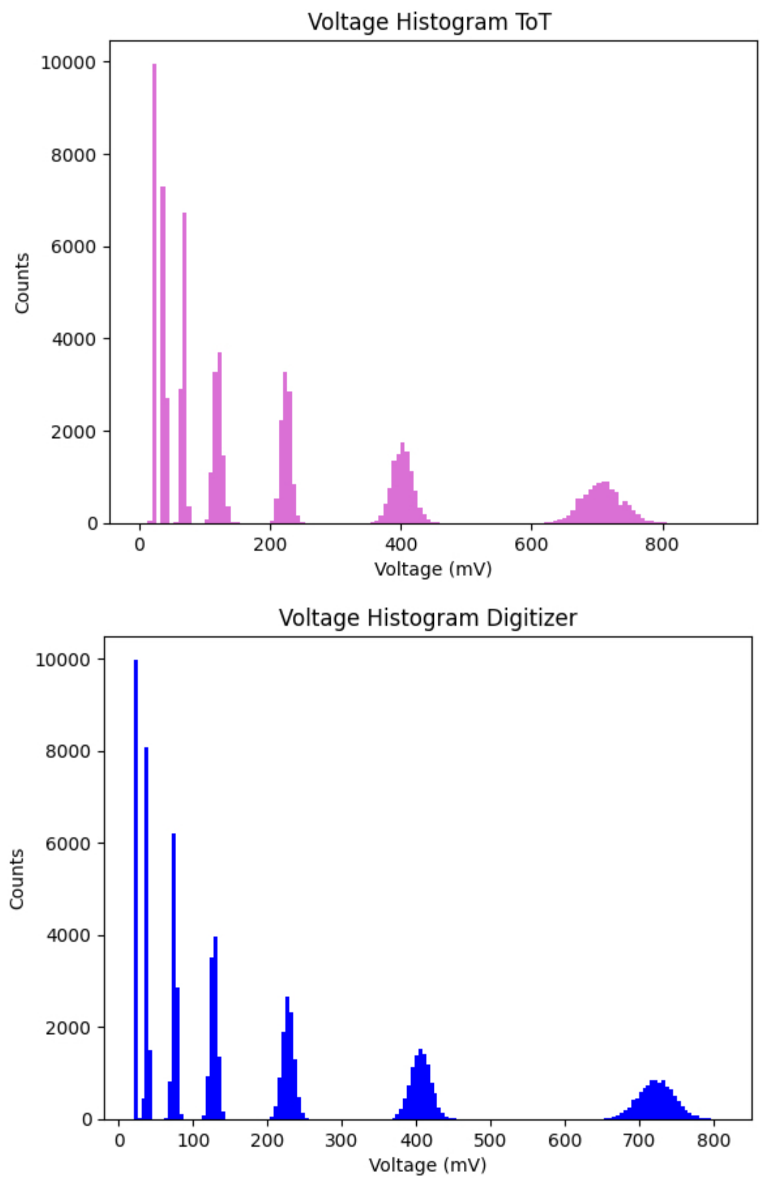

Figure 1.41: (Top) Amplitude distribution from ToT (low and high thresholds merged) and (Bottom) from digitizer.

The amplitude resolution was then calculated for each peak by considering the difference between the amplitudes from digitizer and from ToT in order to subtract possible common sources of signal fluctuations, like the Led Driver light pulse fluctuations. The results for the amplitude resolutions are summarized in Tab.1.13.

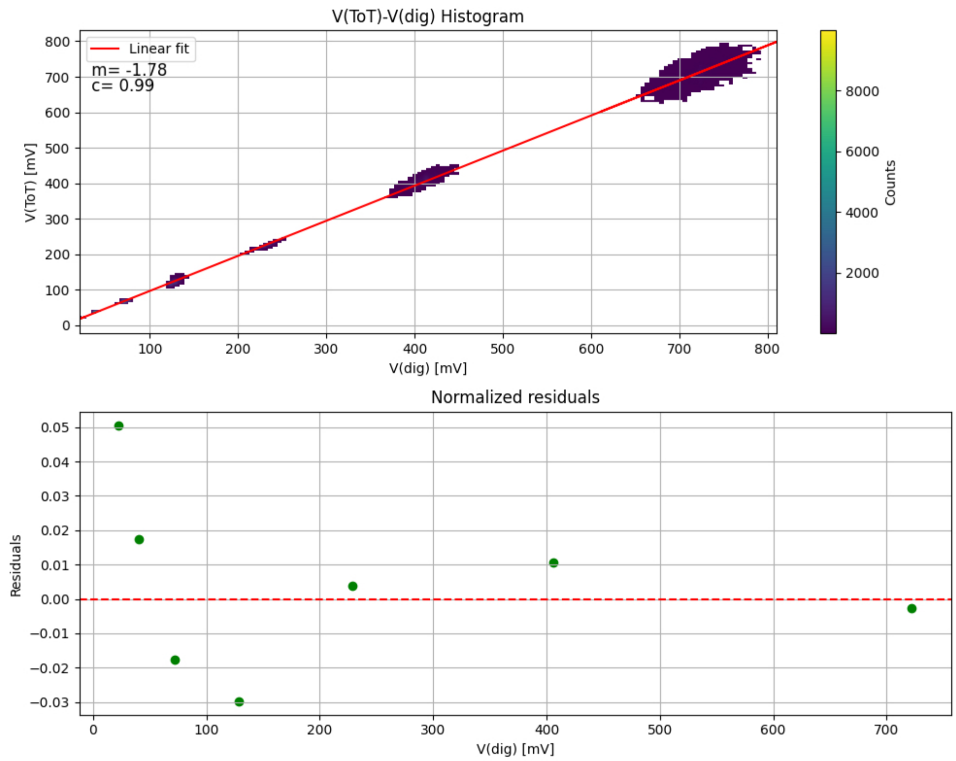

Figure 1.42: Correlation between amplitude from ToT (low and high thresholds merged) and from digitizer.

Table 1.13: Resolutions on reconstructed amplitude peaks from ToT, digitizer, and their difference.

mean A (mV)	σ_A from ToT (%)	σ_A digitizer (%)	difference (%)	best from ToT (%)
722.0	3.2	4.2	3.3	3.3
406.0	3.2	3.8	2.4	2.4
228.3	3.3	3.2	1.5	1.5
128.4	3.6	5.4	4.7	4.7
72.2	4.2	4.0	4.3	4.0
40.6	5.3	4.0	5.2	4.0
22.8	10.8	3.2	10.6	3.2

It is worth noting that the digitizer has a worsening of the resolution at low amplitudes due to the presence of a residual noise, therefore, cannot be considered a reference and subtracted for the lowest values of the amplitude. The best resolutions achieved on the amplitude resolution from ToT considering this limitation are reported in the last column of Tab.1.13.

Finally assuming the PMT gain and the dynamic range of N_{PE} according to the first row of Tab.1.8, by setting the ECAL energy scale 1 MeV = 1 $PE = 1mV$ the amplitude resolution from ToT can be compared to the intrinsic energy resolution of ECAL, eq.(1.4), as shown in Fig. 1.43.

It is worth noting that the resolutions achieved with the picoTDC using the PMT is lower than the intrinsic ECAL resolution throughout the entire explored range (20-700 mV). In the whole range shown in the bottom plot of Fig. 1.43, the following considerations are in order:

1. The two threshold values (10 mv and 100 mV) were not optimized, and there are margins of improvements that remain to be investigated. In particular, the high threshold can be set at higher values than 100 mV to cope with the need of keeping the amplitude resolution below the intrinsic ECAL resolution in the higher end of the energy scale.

2. At an amplitude of 2000 mV, corresponding to 2000 MeV, the limit to keep the preamplifier response linear within the 1 % level is reached.

3. At an amplitude of 2500 mV, corresponding to 2500 MeV, the saturation level of the preamplifier is reached.

4. The shower leakage effects for ECAL ($\sim$ 15 X_0 thick) are anyhow limiting its intrinsic resolution at a scale beyond 1000 MeV.

The foreseen next steps are:

1. Optimization of the thresholds for the best performance in the whole expected dynamic range (2.5-2000 mV) and in the preamp saturation regime.

2. Improve simulation of the PMT signal and FEE electronics in the official SAND MC simulation; implementation of Walk-ToT correction, ToT amplitude reconstruction, preamp saturation etc..

3. Test of PicoTDC and ToT with KLOE modules at the test stand at LNF.

4. Other solutions based on PicoTDC (e.g. CAEN A5204 RADIOROC with picoTDC) are being investigated in collaboration with CAEN, and appear very promising. In particular, from picoTDC with a single threshold discriminator the amplitude can be reconstructed from ToT for all signals, while the amplitude of the largest (and less frequent) signals can be reconstructed from the slower peak-sensing branch implemented in the chip with very good resolution.

In general, once the most suitable solution for ECAL FEE is chosen, it must be integrated in the SAND DAQ scheme, with possible synergies with other SAND subdetector electronics (see

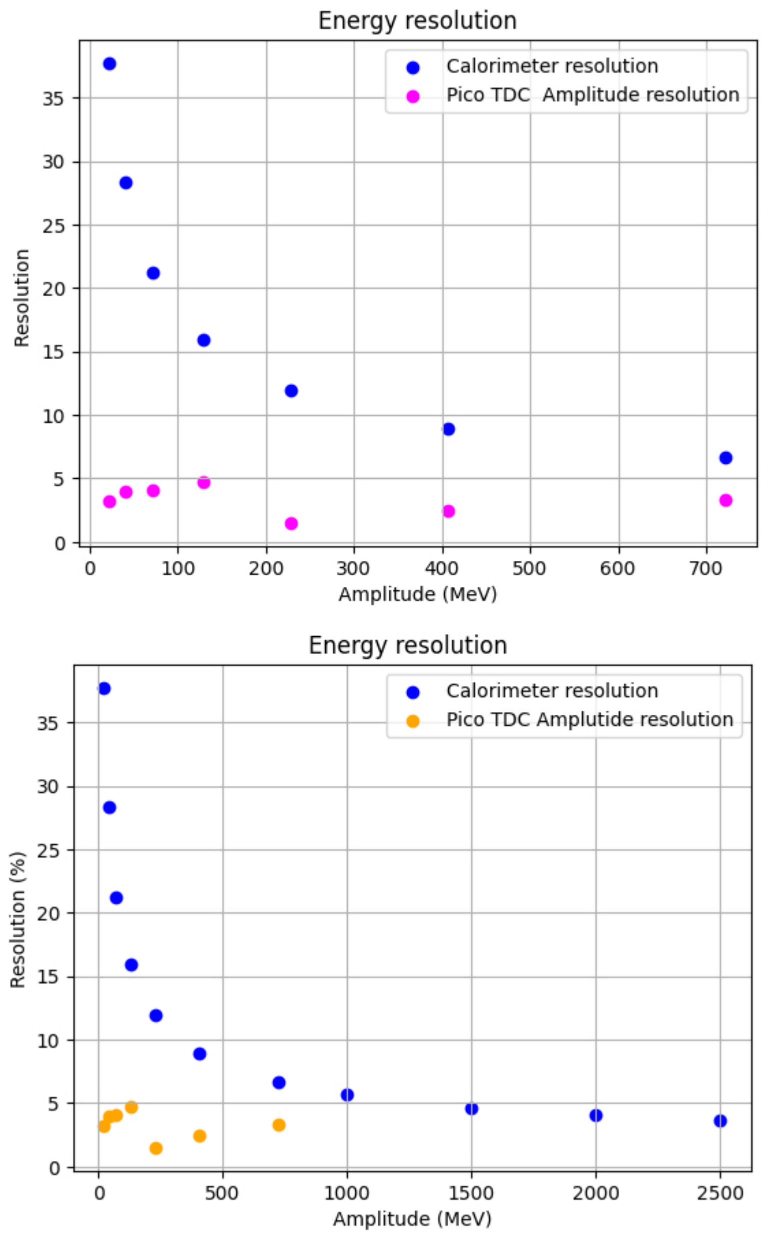

Figure 1.43: Comparison between the intrinsic ECAL energy resolution and the amplitude resolution from ToT vs. energy in the explored range (20-700 mV) (Top) and in the whole energy range expected for signals (Bottom).

Sec.**??**).

1.1.5.3 High-voltage

The Hamamatsu R5946/01 PMTs requires a maximum supply power of 2.3 kV, absorbing an average anode current of 0.01 mA. The CAEN SY4527 mainframe is capable of hosting up to 16 HV A7030P modules suitable for powering the ECAL PMTs. The CAEN A7030P is a module able to independently control up to 48 channels, with an output range of 3 kV/1 mA (1.5 W) at a low ripple (<20 mV_{pp-max} in the range 10 ÷ 1000 Hz and <10 mV_{pp-max} over 1000 Hz). The A7030P module is supplied with a high density multipin Radiall 691803004 connector. This connector is inadequate for powering the ECAL PMTs, therefore a multipin to SHV adapter will be used. The CAEN R648 19” rack module fits one Radiall 691803004-type multipin connector into 48 Radiall R317580-type SHV connectors, suitable for powering the ECAL PMTs. Moreover this module provides Interlock and Shield connections (through LEMO connectors). The described system includes a complete set of software tools for remote control (*via* Gigabit Ethernet or Wi-Fi) of both the mainframe and the high voltage boards, from low-level libraries to graphical application software. Furthermore a proprietary software introduces easy logging capability to the system. Through this tool it is possible to records every command sent to the system and every warning/alarm detected by the system. In this way it is possible to automatically monitor the behavior of every single parameter during operations.

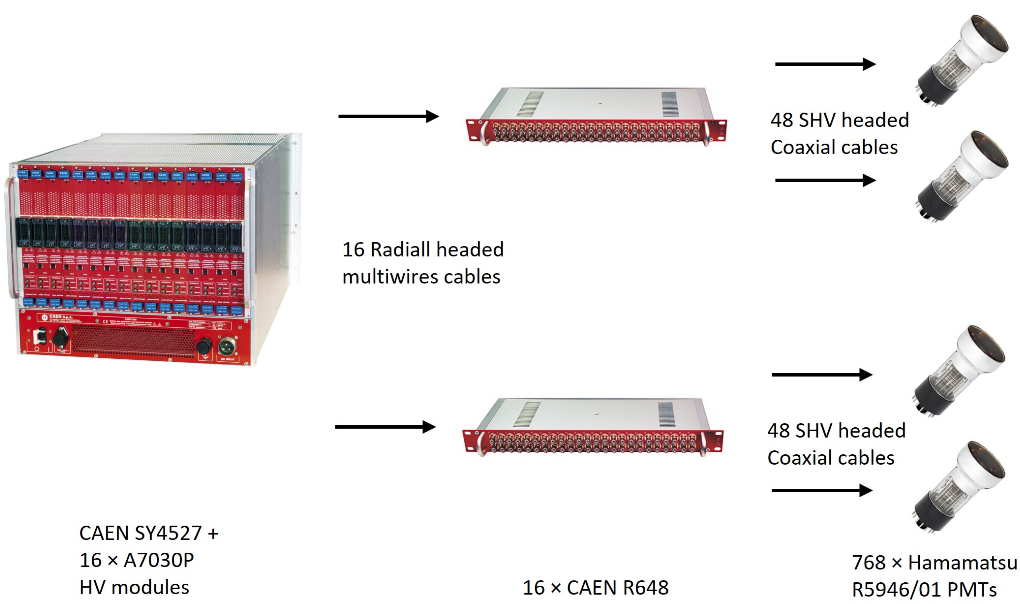

Figure 1.44: HV system to power 768 ECAL PMTs. In order to power all the PMTs, 7 of these systems are required.

Powering 4800 PMTs requires 100 CAEN A7030P HV modules that will be host in 7 CAEN SY4527 mainframes. In addition, 100 CAEN R648 Radiall to SHV connector adapters will be used to transfer HV power from HV module to PMTs. The unused mainframe slots can be used to save HV spare modules (Fig. 1.44).

1.1.5.4 Low-voltage

Each preamplifier on a PMT base is supplied with ± 6 V and has a power consumption of 60 mW. Few CAEN A2551 boards, each with 8 full floating channels 8 V/12 A, are sufficient to power all 4880 PMT bases. The output voltage range is $0 \div 8$ V, with 0.2 mV monitor resolution (connector and sense voltages). The maximum output current is 12 A with 500 μA monitor resolution. The maximum channel power is 60 W. These boards can be host in the same CAEN SY4527 mainframes used for HV.

1.1.6 ECAL Dismounting Procedures

The first step to dismount the KLOE detector was the removal of cables, racks and other stuff in the experimental hall. A huge quantity of cables was unplugged from the calorimeter and the ancillary devices. Only signal and HV cables were stored to be reused at Fermi National Accelerator Laboratory (Fermilab). Twelve boxes were filled with 4880 signal cables and 4880 HV ones (Fig. 1.45). Both the types of cables are 15 m long. From the six platforms aside KLOE 32 FEE+HV racks, 150 crates, and 3000 boards were removed.

Figure 1.45: Left: cables (red) connected to the endcap PMTs. Right: removed cables assembled for the shipping.

The extraction of the Drift Chamber (DC) was the second step. Event though it will not be reused at Fermilab, the extraction was very careful because it will be displayed in the Laboratori Nazionali di Frascati (LNF) exhibition area. The DC structure is made of carbon fibers, the spherical endplates are kept apart by 12 rods, and an external ring is coupled to each endplate through 48 screws, to allow the recovery of the endplate deformation under the wire tension load. The gas sealing of the chamber is ensured by the inner cylinder and 12 panels. About 60.000 wires are tensioned between the endplates, each of which is crimped on the copper feed through. The chamber extraction procedure has been thought considering several aims: to preserve the DC integrity, to avoid the wire breaking, and to ensure the safety of people.

The extraction of the DC was based on the insertion of a beam (Fig. 1.46, right) on the axis of the cylindrical chamber, its clamping on the endplates and the extraction of beam and chamber as a unique piece. More in detail, at the beginning the beams (HEA200, 6 and 5 m long) were placed on 3 reinforced concrete pillars. Then the 6-m beam was inserted inside the DC. The beam and the DC were lifted up of few millimeters by means of the crane. This was enough to unload the DC weight from the static supports inside the calorimeter. A system with trolleys, suitably positioned on the endplates, allowed the DC to slide along the beam. Once the chamber was extracted from the calorimeter (Fig. 1.46, left), it was lifted, with a suitable sling bar, and placed on a handling trolley placed at the entrance of the experimental hall. Then it was ready to be taken away.

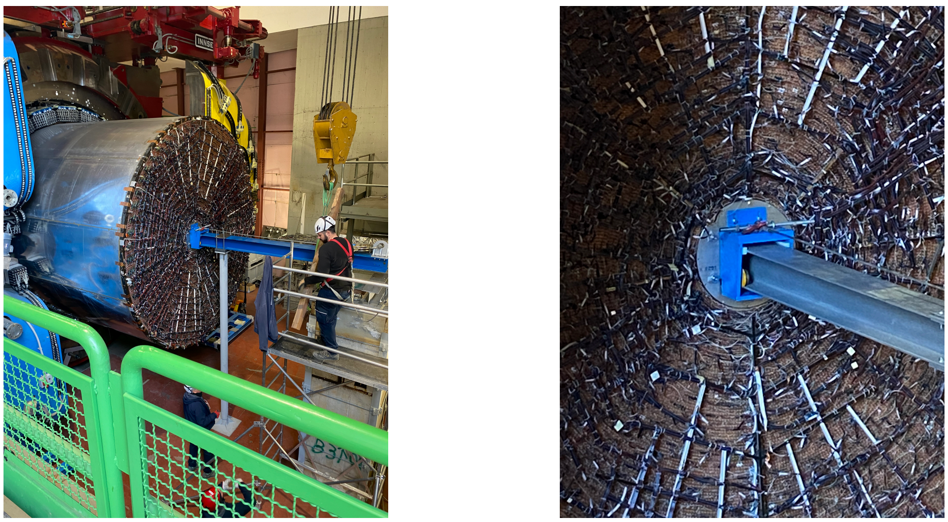

Figure 1.46: Left: extraction of the drift chamber at LNF. Right: zoom on the HEA200 beam and the trolley (detail in the text).

1.1.6.1 Barrel Modules

The operation consists in the extraction of 24 calorimeter modules located inside the KLOE apparatus. The module dimensions and mass are reported in Fig. 1.47. Each module has a mass of 3500 kg and is made by several layers of lead and scintillating fibres glued together. The layout of the calorimeter is shown in Fig. 1.48 together with the number scheme used.

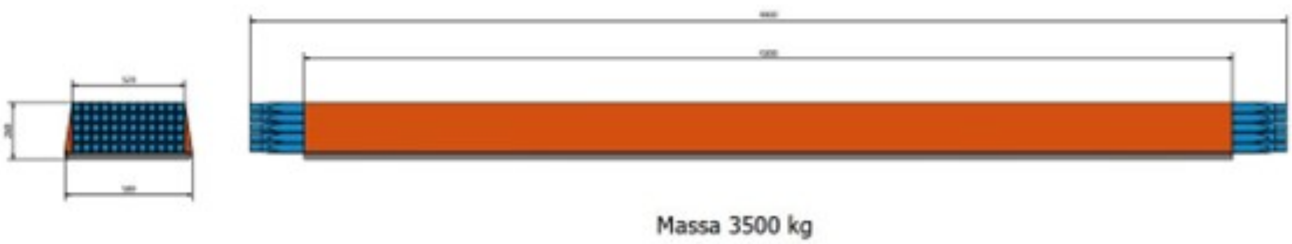

Figure 1.47: Scheme of a module of the barrel.

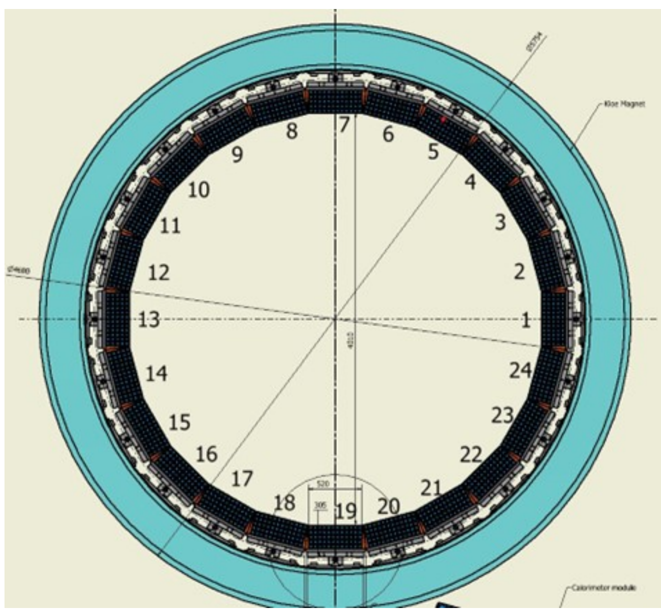

Figure 1.48: Scheme of the 24 modules of the barrel of the calorimeter.

For this operation the old insertion tool has been thoroughly refurbished and used as extraction tool (see Fig. 1.49). It requires an external platform to be placed at the proper height, that has been also designed and customarily realized by an external company under ECAL group supervision (see Fig. 1.50). Both are suitable to be used for the insertion of the modules as well, and are compliant with US safety rules. The 24 modules can slide through bearings on the bars fixed to the internal wall of the magnet cryostat vessel (see Fig. 1.51). The extraction tool has a steel shaft (Fig. 1.52 left) that once is engaged with the support bar allows to extract the module. The shaft is fixed on the upper frame of the extraction tool, that can be moved longitudinally and rotated in all the 3 space axis independently from the base with precise fine-tuning screws, in order to perfectly align the two shafts without moving the heavy base part.

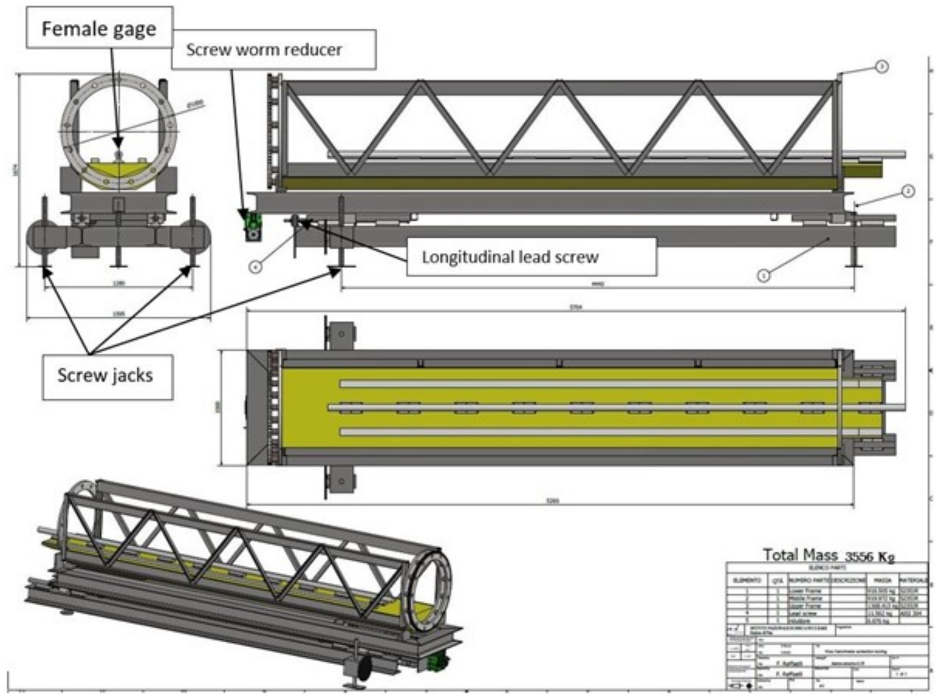

Figure 1.49: Drawing of the barrel modules extraction tool.

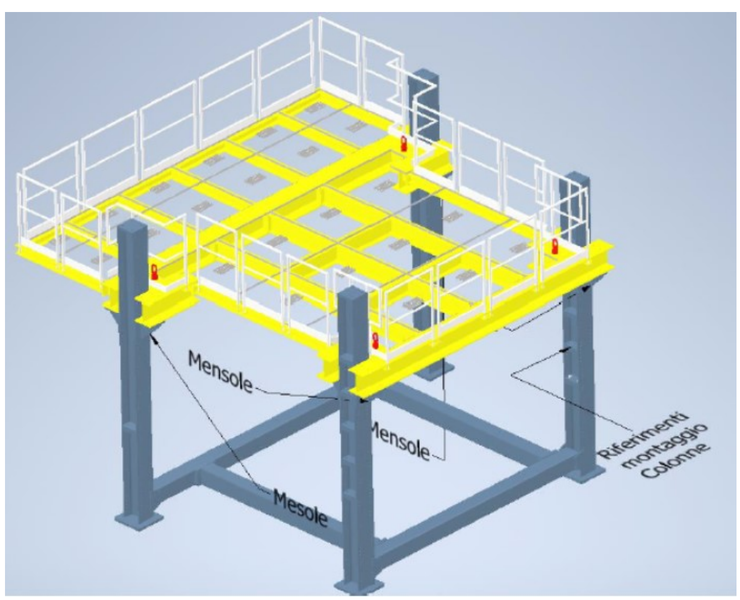

Figure 1.50: Drawing of platform used to position the extraction tool in front of the calorimeter.

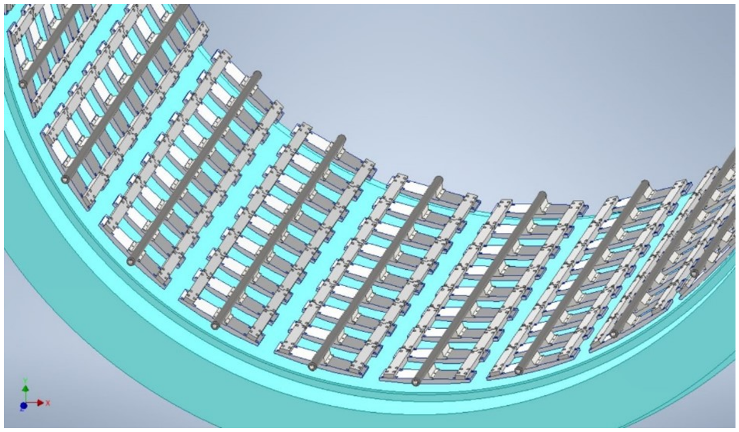

Figure 1.51: Detail of the supporting bars inside the cryostat.

Figure 1.52: Extraction tool (left) and its operating position on the movable platform (right).

The complete list of steps to dismount the barrel is:

1. Insertion of internal support pillars. Nine pillars have been used to hold up the upper modules: 3 on the moving module with rolling elements and 3 fixed on each of the neighbour modules (see Fig. 1.53).

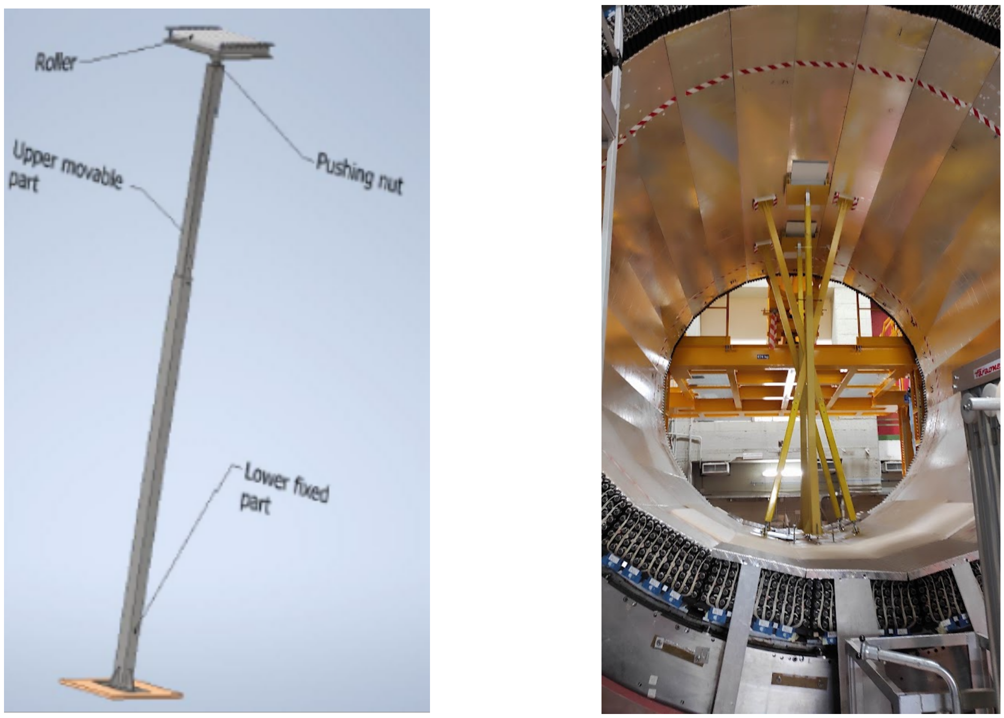

Figure 1.53: Draw of safety support pillar (left) and the pillars mounted inside the calorimeter (right).

2. Setup of the external platform at the appropriated height. For each couple of modules at the same height the platform is properly moved on its legs. The same position is used for the group of the 3 uppermost modules thanks to a limited vertical adjustment of the extraction machine.

3. Setup of the extraction tool on the platform with the crane. Once positioned the extraction tool is aligned to the module by adjusting the upper frame which has independent movement controls in all 3 spatial planes. When the extraction shaft and the module shaft are aligned, the upper frame is rotated to the right angle corresponding to the module (see Fig. 1.53). Finally the frame is longitudinally moved towards the module until the two shafts are engaged through their conical coupling ends.

4. Pull out of the module. A belt is fixed to the module and to a chain hoist used to manually extract the module. Four screws inserted in the bottom plates of the modules, at its ends, act as guides, scraping their heads on rails mounted on the extraction machine. Adjusting the screws it allows to slightly rotate the module around its supporting shaft to gain few tenths of millimeter clearance between the adjacent module. The friction of the screws on the rails creates the most force needed to move module, measured by a dynamo-meter in several thousands of newtons.

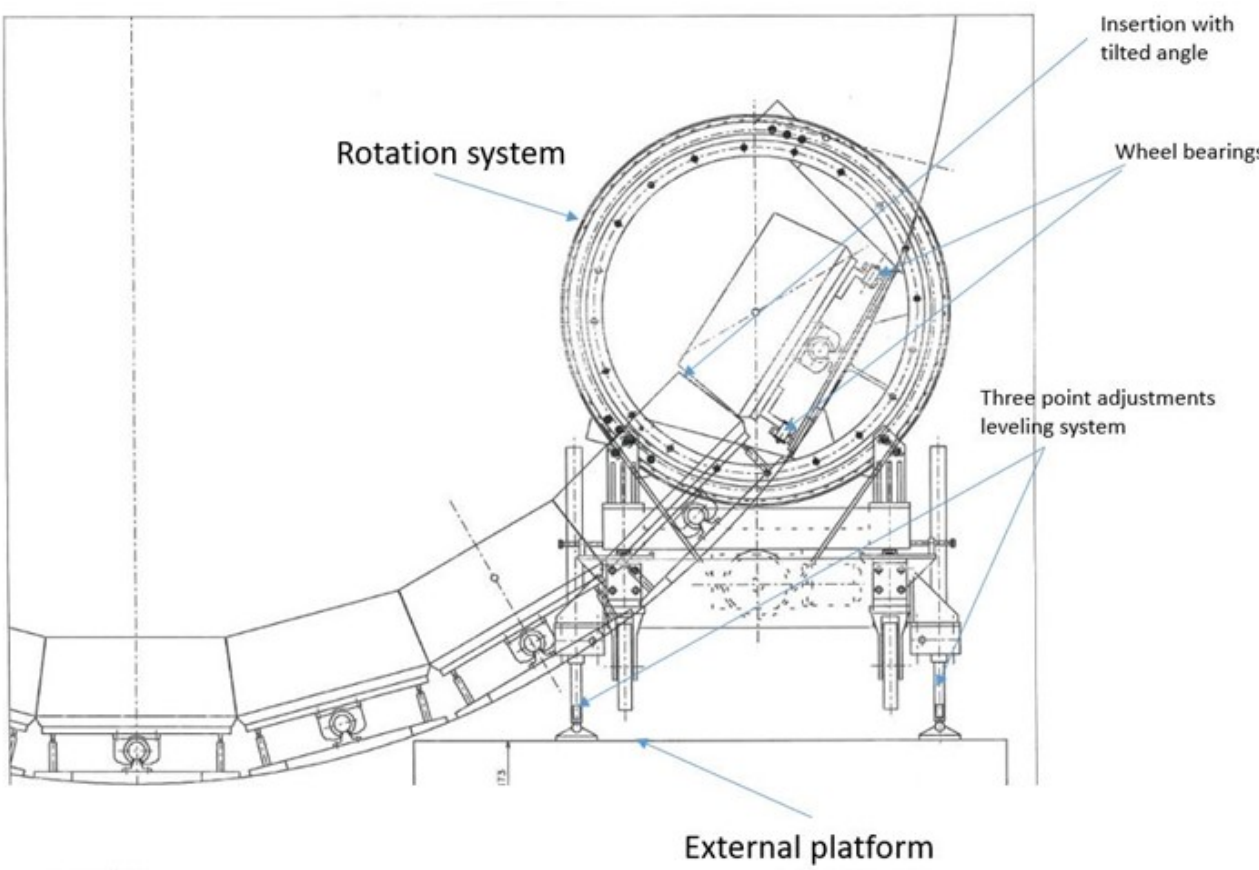

Figure 1.54: Scheme of the extraction of a module.

5. Secure of the module with confining straps. While the module is extracted from the magnet vessel straps are placed every meter to wrap the lead layers and avoid possible delamination.

6. Positioning of the extracted module. When the module has completely shifted from the support shaft to the extraction tool shaft, the upper frame is first retracted to the rear stop position and then rotated to until the module is placed horizontally with the support plates on bottom.

7. Lift of the module and move to the storage area. The module is disconnected by the support plates and the bearings, lifted with the crane from the extraction tool and moved to the test area (see Fig. 1.55).

Figure 1.55: Test area for ECAL modules at LNF.

1.1.6.2 Endcap Modules

Here the operation list is presented for the endcap dismantling.

At the very beginning the disassembly tool is positioned in front of the KLOE apparatus. Once the disassembly tool has been positioned, and the overhead crane has also been positioned, first module is extracted after having previously dismantled it from the plate (see Fig. 1.57).

Now let's assemble the module Cradle, which will also be used to transport and place the module on the transport support.

The disassembly procedure involves using the upper holes with a diameter of 21 mm, present on the tool, to insert a pin with nut, which are then screwed into the two M12 threaded holes of the revolving eyebolts with joint. This operation allows to hook the straps to the overhead crane and start rotating the module and bring it to an almost vertical position.

By positioning a rotating eyebolt with joint, the unhooking of the structure begins.

In this phase, the pushers present in the calorimeter plate are activated and a gap is created

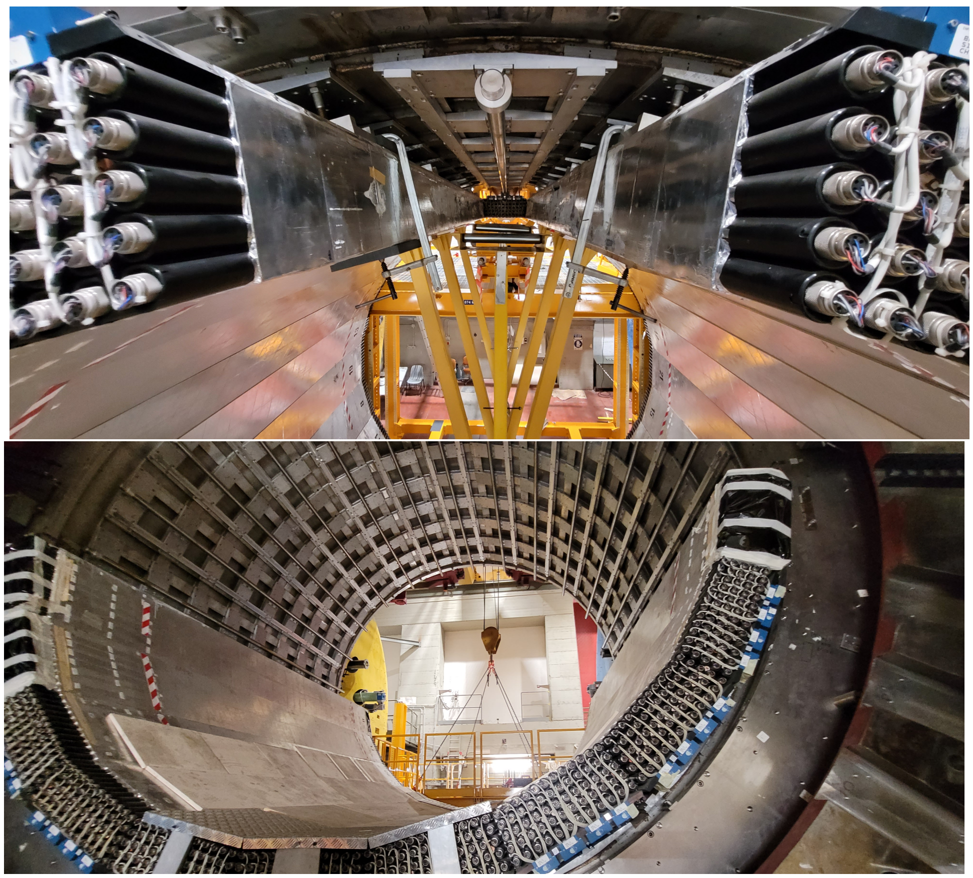

Figure 1.56: Extraction of the first barrel module from magnet cryostat.

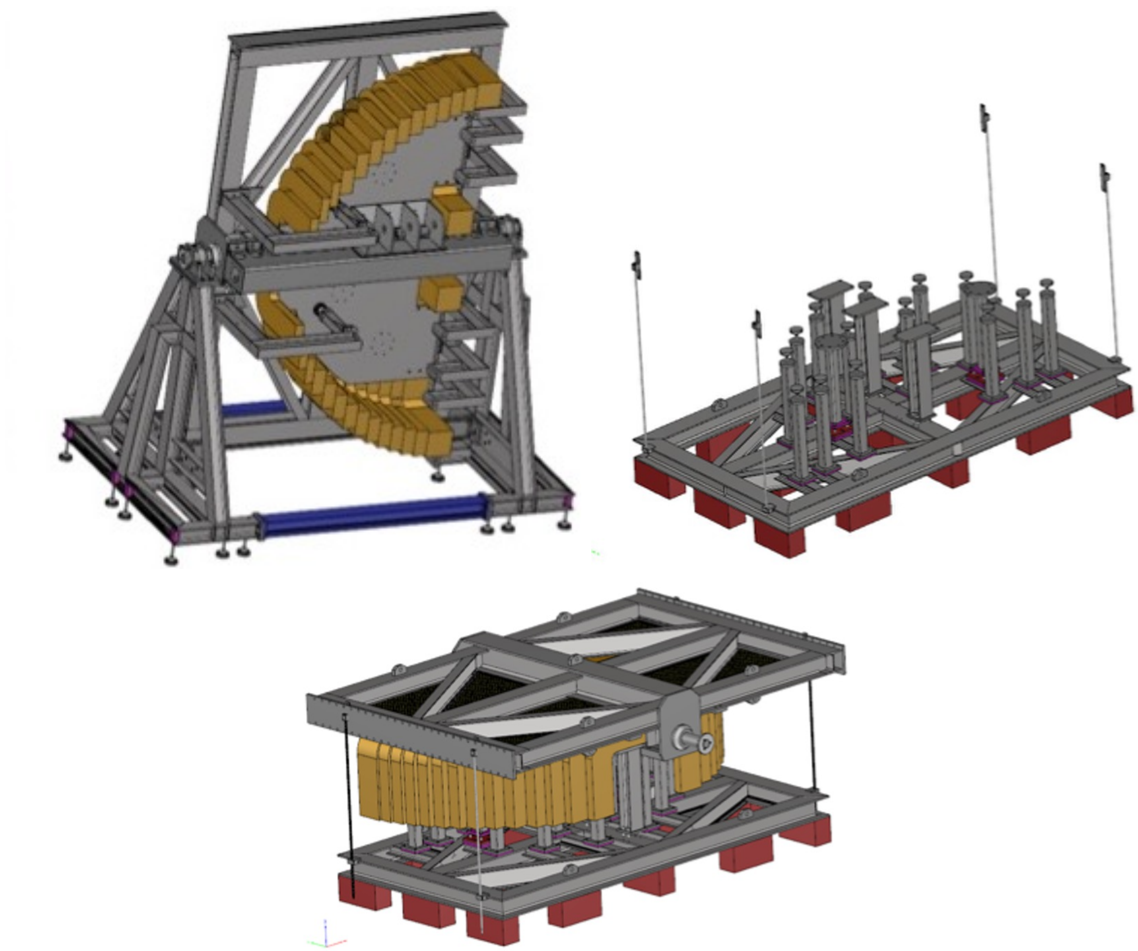

Figure 1.57: Disassembling, rotation and handling mechanical tools for EndCaps.

between the iron part and the bearing plate of the calorimeter. This operation allows the insertion of the aluminum shelves, on which a sliding beam will be slid, which is aligned with the M24 threaded holes on the half-plate and subsequently blocked with screws.

The tool with the rotating table (tipper), using the holes present on both ends, blocks the barycentric subsystem, which will allow the rotation of the rotating table dragged by the overhead crane. The rotating plane/center of gravity system is transported to the half-plate via the overhead crane. Through the centering of the eight M36 holes present on the blue beam, the entire system becomes integral.

The next phase consists in assembling the 2 "C" supports on one side and the other 6 small ones on the other; this operation serves to minimize the possible deformations that the calorimeter plate could undergo.

The movement of the rotating table/calorimeter system begins up to the support which will allow the rotation of the table from vertical to horizontal, and the first pair of the braking system is also added, which guarantees the table in a vertical position, subsequently it is blocked with the second braking couple and you can proceed with the rotation maneuver.

Using couple support, ensure that the system stops in an almost horizontal position, dismantle the barycentric system and proceed to assemble the system to center the calorimeter with the support on the rotating table used for shipping.

The next phase is to prepare the shipping tool and proceed with the assembly of the 14 supports, adjusting them to a height of 955 mm. The centering system is positioned through perforated plates, blocked on the frame for shipping and using a clamp system.

Afterwards it is possible to transfer the calorimeter using the overhead crane to the shipping support, and to place the calorimeter on the shipping frame on the 14 named supports. The calorimeter half-plate can be blocked using the M16 holes, used to connect the pushers, with the 2 supports and using the centering system made up of several slotted plates connected integrally to the shipping frame, compensating any difference in height with threaded bars.

Using the holes present on the sliding beam, it is necessary to insert eyebolts so as to be able to hook the straps which, when attached to the overhead crane, will allow the dismantling of the screws connecting the sliding beam to the half-plate, which will be placed on translating tables to allow its extraction from under the calorimeter.

The last phase, using the revolving table, transport everything to the storage

1.1.7 ECAL Revamping and Test before SAND Installation

The 24 modules composing the Barrel of ECAL will be thoroughly revamped after their dismantling. The list of operations needed in order to have the parts ready to be mounted again is:

- gluing of delaminated lead foils;
- gluing of the unstuck light-guides;
- repair of aluminum grids holding PMTs;
- repair or replacement of the aluminum protection of PMTs;
- wrapping of modules with aluminum tape reinforced with glass-fiber.

Delamination of lead foils from the support plate notoriously occurred in the top-most 3 modules just after the calorimeter assembly. During the years of KLOE operation the position of the internal face of these modules has been monitored with gauges, but no evidence of further detachment happened. A laser-tracker 3D mapping of the calorimeter has been performed before the dismantling, confirming a delamination of the top-most 3 modules resulting in an increase of the overall thickness of about 20 mm. Minor increases, of the order of 1 mm, have been measured for other modules mounted on the top part of the cryostat. All these modules have been supported by pushing rods during their extraction, to avoid any additional damage and for safety reason. The revamping procedure foresees to leak an epoxy adhesive into the delaminated layers and press the module, possibly with a vacuum-bag. The Loctite EA-9483 is quite suitable, having a very low viscosity and a high optical transparency. This gluing process is needed by about 6 modules (see Fig. 1.58).

Figure 1.58: Delaminated ECAL modules.

In only one case during the extraction the light-guides have been disconnected by the lead. Neither of the parts have been damaged, so we proceeded to the polish of the surfaces and a new gluing (see Fig. 1.59).

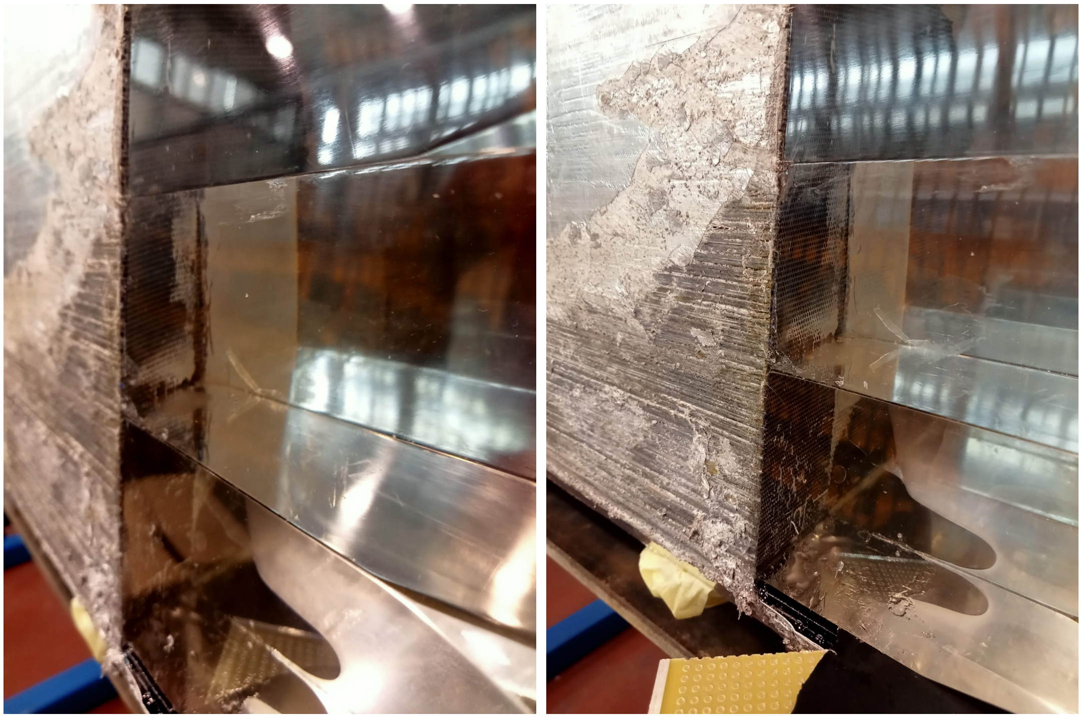

Figure 1.59: Light-guides before and after gluing.

In the same module the grid in front of the PMTs has been bent during the extraction. It is going to be machined as new (see Fig. 1.60).

Figure 1.60: The aluminum grid supporting PMTs going to be replaced.

On their side-ends the light-guides have additional protection foils, made by aluminum 0.25 mm thick. In few cases these have been damaged, and are going to be installed as new.

Finally, the most time-consuming revamping activity is the new wrapping of the modules. The 3M-363 tape has been identified. It is made of aluminum and fiberglass, 450 mm wide and 0.19 mm thick. The old tape will be removed and replaced on all parts where it is deteriorated, while where it is perfectly intact the new tape will be placed above (see Fig. 1.61).

Figure 1.61: A module during the tape wrapping work.

Although not damaged, the support plates of the modules will be partially revamped. Each module hosts 3 aluminum plates 30 mm thick, fixed with screws to the long bottom plate acting as base for the lead and scintillating fibers layers. These plates hold the cylindrical cushions which bind the modules to the support bars fixed in the inner wall of the magnet cryostat. All the screws will be replaced with new and we are studying the possibility of machining the plates, thinning them by few millimeters. In this way the modules will be closer to the magnet and we would gain clearance between the side faces of modules, allowing a smoother and easier mounting.

1.1.7.1 Light Tightness and Tests with Cosmic Rays

The tape wrapped around the modules has not only a mechanical role, but is also mandatory for the light tightness. After the complete re-wrapping a test of the light tightness of the modules is necessary. Most of PMTs have been already dismounted for safety during the extraction operation of the modules from the magnet. All PMTs will be dismounted, and after a proper cleaning of the light guides and PMT photocatode window from the old optical grease, they will be reinstalled in the ECAL modules, applying a new optical gel for the optical contact.

Afterwards, the single PMTs and the entire modules will be tested. The PMT check consists in the readout of the output signal from each tube. A test stand will be equipped with the KLOE readout electronics (constant fraction discriminators, analog-to-digital converter (ADC)s, and TDCs) to check the operation of two complete barrel modules (240 PMTs) collecting signals induced by cosmic rays. The module performance in terms of light yield, energy and time resolution and coordinate reconstruction along the fibers will be measured according to procedures already developed during the commissioning in KLOE at a similar cosmic ray test stand [9]. The consistency of the results with the expected ECAL performance will be checked.

This will allow also to perform comparative tests of prototypes of the new FEE chosen for ECAL, with respect to KLOE FEE, the latter guaranteeing the ECAL performance cited in Sec. 1.1.2.

After the test all PMTs will be dismounted by the ECAL modules and shipped separately from the modules to Fermilab.

1.1.8 ECAL Installation & Integration

1.1.8.1 Packaging and Shipping

The calorimeter will be shipped from LNF to Fermilab travelling by ship. The closer harbour to Frascati which might be capable to dock a suitable ship is Anzio (roughly 50 km away). Once dismantled into 24 barrel modules and 4 End-Caps, ECAL can be placed in a euro-container and is allowed to travel on road with standard trucks, not being considered oversize load transportation and avoiding special permits (that will be necessary for the magnet).

As a first step a mechanical project of the shipping is required for the definition of the maximal vibrations and temperature interval tolerated by the calorimeter during the transportation. Accelerometers and thermometers will be included in the container. Each of the 24 modules of the barrel will be packed in a dedicated wooden or metal box. The 4 EndCaps will have dedicated boxes as well.

1.1.8.2 Activities at Fermilab

Upon arrival at Fermilab, ECAL modules will be stored in a proper area equipped with a crane of 5 t maximum load for handling barrel modules, and 15-20 t for handling Endcap modules. A controlled temperature environment is required in the storage and test area of ECAL modules, avoiding thermal stresses and keeping temperature changes within about $\pm 10°$ C along the whole period.

The quality assurance (QA) and quality control (QC) operation will be performed repeating the tests on each module done at LNF, as described above. In particular, after re-installation of PMTs in the ECAL modules (shipped separately), the ECAL module performance in terms of light yield, energy and time resolution and coordinate reconstruction along the fibers will be measured and checked again at a cosmic ray test stand, with the same equipment used at LNF, before installation in the SAND detector.

1.1.9 Risk Management

The existing components, repurposed from the KLOE detector have operated for several years at the INFN Laboratori Nazionali di Frascati. Their functionality is amply demonstrated, and their performance well known and documented [10]. As part of the preparatory work, to be performed before delivery of the components to Fermilab, all subcomponents, after minor repairs and eventual upgrades, will be extensively tested at LNF. These tests, in addition to confirm the functionality of the subcomponents before travel, will also establish the protocols to be used for QA and QC upon arrival at Fermilab. Development of appropriate documentation for approval of operation at Fermilab is being conducted in close cooperation with a dedicated Fermilab engineering team which is also involved in the definition of the necessary QA/QC protocols. Finally, the same teams and companies involved in the disassembly and test of the repurposed subcomponents, will conduct the tests and the re-assembly at Fermilab. The strategy described above covers most of the risks associated to the installation and utilization of the existing subcomponents of the KLOE detector at Fermilab. The risk analyses in this Section and in Sec. 1.1.9 mostly focus on possible damages occurring during the transport from LNF to Fermilab. Catastrophic events, such as the destruction or the loss of significant portions of the ECAL are not considered, as they would imply a significant re-definition of the experimental program. It has to be noted that the ECAL modules have been transported by truck from their production sites to LNF (about 100 km), without any issues. Other events considered in the risk analyses are related to reassembly operations and to non-functionality of newly constructed components.

1.1.9.1 Detailed risk analysis

1. Event: External damage with inelastic deformation of the lead or the aluminum cover in the hit point, or partial detachment of light guides

   - Possible causes - Shock, bump or vibrations occurred during the transport.
   - Possible consequences - Impossibility of installation of the damaged module due to the deformed geometry, inoperability of the ECAL cells corresponding to the damaged portion of the module. Localization and repair of the damage, by partial disassembly of protective tape and aluminum covers if needed, machining and milling the surface on the hit point, or by re-gluing possible delaminated lead foils, re-gluing or substituting the damaged light guides during the QA/QC phase at Fermilab. These operations cannot take place in the alcove. The estimated time for the operations ranges from few days to two weeks depending on the severity of the damage.
   - Estimated Probability - Moderate, 2% to 5% (from long distance transport statistics).
   - Detection - Visual inspection after delivery to Fermilab, check the recording of the accelerometers. Test of module before insertion in the detector.
   - Intervention- Repair the module and re-test its functionality and performance with cosmic rays.
   - Mitigation - Detailed engineering of the transport with shock and vibration analysis and thermal shock analysis; definition of maximum accelerations, of maximum speeds of road transport, definition of supports and shock absorbers, definition of maximum thermal

variation and of controlled temperature container or environment during transport. Transport with online shock logs and periodic check-points. Choice of carrier with highest reliability for special transports. Early detection by inspection and test upon arrival at Fermilab and before installation of detector components in the magnetized volume.

2. Event: thermal stress with possible partial detachment of light guides or partial damage of scintillating fibers

    - Possible causes - Large temperature variations during the transport or temporary storage.
    - Possible consequences - reduced light collection efficiency and Physical performance of the modules. Localization and repair of the damage, by partial disassembly of protective tape and aluminum covers if needed, re-gluing light guides during the QA/QC phase at Fermilab. These operations cannot take place in the alcove. The estimated time for the operations ranges from few days to two weeks depending on the severity of the damage.
    - Estimated Probability - Moderate, 2% to 5% (from long distance transport statistics).
    - Detection - Visual inspection after delivery to Fermilab, check the recording of the thermometers. Test of module before insertion in the detector.
    - Intervention- Repair the module and re-test its functionality and performance with cosmic rays.
    - Mitigation - Detailed engineering of the transport with thermal shock analysis; definition of maximum thermal variation and of controlled temperature container or environment during transport. Transport with online temperature logs and periodic check-points. Choice of carrier with highest reliability for special transports. Early detection by inspection and test upon arrival at Fermilab and before installation of detector components in the magnetized volume.

3. Event: thermal or mechanical stress of PMTs with possible vacuum leak

    - Possible causes - Shock, bump or vibrations occurred during the transport, or thermal shock during the transport or temporary storage.
    - Possible consequences - Inoperability of PMTs. Broken units need to be replaced before installation in ECAL modules. during the QA/QC phase at Fermilab. These operations cannot take place in the alcove.
    - Estimated Probability - Moderate, 2% to 5% (from long distance transport statistics).
    - Detection - Visual inspection after delivery to Fermilab, check the recording of the thermometers. Test of module before insertion in the detector.
    - Intervention- Repair the module and re-test its functionality and performance with cosmic rays.
    - Mitigation - will be dismounted from ECAL modules and shipped separately in smaller and easier to handle boxes (as delivered by Hamamatsu from Japan to Italy). Detailed engineering of the transport with shock and vibration analysis and thermal shock analysis; definition of maximum accelerations, of maximum speeds of road transport,

definition of supports and shock absorbers, definition of maximum thermal variation and of controlled temperature container or environment during transport. Transport with online shock and temperature logs and periodic check-points. Choice of carrier with highest reliability for special transports. Early detection by inspection and test upon arrival at Fermilab and before installation in ECAL modules.

4. Event: Malfunctioning or break of ECAL electronics - High Voltage and Low Voltage power supply and FEE (new equipment).

    - Possible causes - Infancy defect. Damage due to transport.
    - Possible consequences - Inoperability of corresponding ECAL modules. If detected during the commissioning it would result in a stop of the commissioning for the time required for repair/substitution. Spare units are available for a prompt substitution if needed.
    - Estimated Probability - Moderate $\sim 2\%$
    - Detection - Operate the unit and monitor its functionality and corresponding ECAL module performance.
    - Intervention - Remove the unit. Assess the problem in the lab and define the required repair or substitution.
    - Mitigation - Early detection by testing electronics in the lab or during QA/QC phase before installation.

1.1.10 Schedule and Milestones

The completion of the calorimeter dismantling is foreseen for the end of 2024, with the disassembly of the EndCaps. All the mechanical tooling for this activity is ready and the KLOE hall has been cleared from the previous equipment used for the barrel extraction.

A detailed time-schedule of the ECAL dismounting and shipping is summarized in Fig. 1.62. The milestones are:

- Complete ECAL dismantling: December 2024
- Magnet test: July 2025
- Extraction of magnet cryostat: April 2026
- Shipping: May 2027

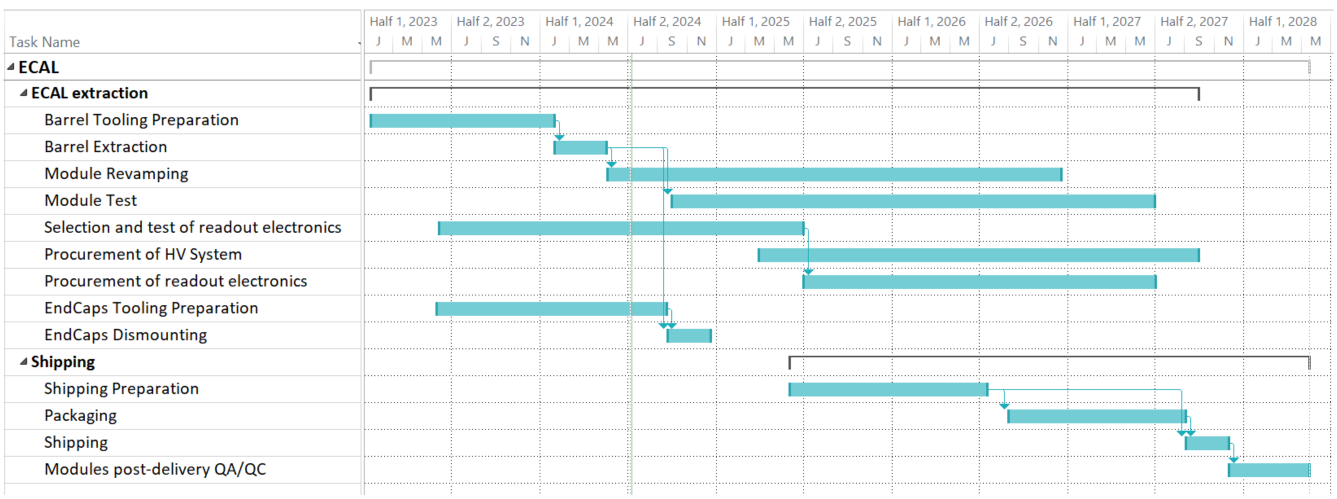

Figure 1.62: GANTT for ECAL dismounting and shipping.

1.2 The Superconducting Magnet

1.2.1 Magnet Specification

The KLOE Magnet is an iron shielded superconducting solenoid coil with a thermo-siphoning cooling method (made by Oxford Instruments A.T.G. - England). The design constructed by Oxford Instruments is shown in the schematic of Fig. 1.63.
The cryostat possesses its own valve box, Joule Thomson (JT) valve and LHe (liquid helium) reservoir of $\sim$ 150 liters. The total liquid volume in the system is in the order of 200 liters.
All the controls associated with magnet functioning (including cool down and warm up) are an integral part of the magnet system. In the following the main feature of the cryogenic configuration are listed:

1. Coil cooling: Thermo-siphoning cycle. 5.2 K GHe at 3 bars from the cryogenic plant and liquefied through JT valve into LHe reservoir for cooling the coil

2. Radiation shield: cooled with 70 K GHe from the cryogenic plant

3. Current leads: cooled with LHe from reservoir; 300 K GHe returns to the cryogenic plant

4. The magnet is under "continuous cooling"

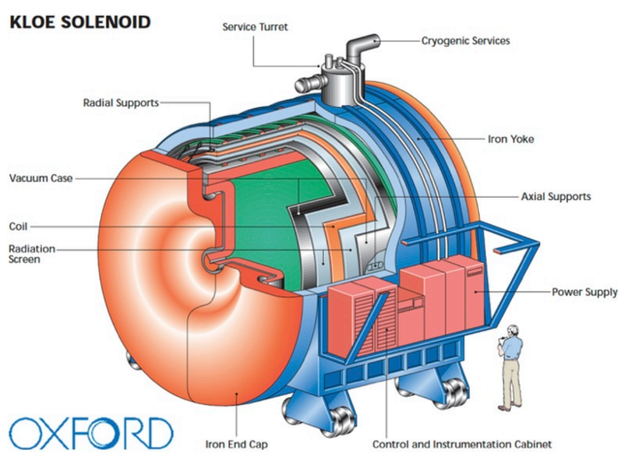

Figure 1.63: Schematic KLOE solenoid.

The superconducting magnet was designed, in conjunction with its iron yoke, to produce 0.6 T over a 4.3 m long 4.8 m diameter volume. The magnet specifications and the major coil parameters are listed in Tab.s 1.14 and 1.15 respectively.

The KLOE magnetic field has been mapped in 1997 by means of a Hall probe integrated on a dedicated positioning device, called MagAx. The MagAx main body was a precisely machined beam of about 7 m length, made of a special Al alloy. The 5 mm $\times$ 14 mm flat encasing of the Hall probe was precisely positioned normally to the longitudinal axis, on the long front face of a 1 cm $\times$ 1 cm $\times$ 170 mm finger support. Details of the device can be found in [11]. Fig. 1.64 reports the solenoid longitudinal field component along the solenoid axis.

Table 1.14: Magnet specifications.

Central magnetic field	0.6 T
Vacuum case length	4.4 m
Vacuum case inner diameter	4.86 m
Vacuum case outer diameter	5.76 m
Coil shell inner diameter	5.19 m
Cold mass	10 t
Vacuum case mass	26 t
Iron return yoke mass	475 t

Table 1.15: Coil parameters.

Layers	2
Turns/layer	368
Ampere-turns	2.14 MA-T
Operating current	2902 A
Stored energy	14.3 MJ
Inductance at full field	3.4 H
Discharge voltage	250 V
Peak quench temperature	80 K

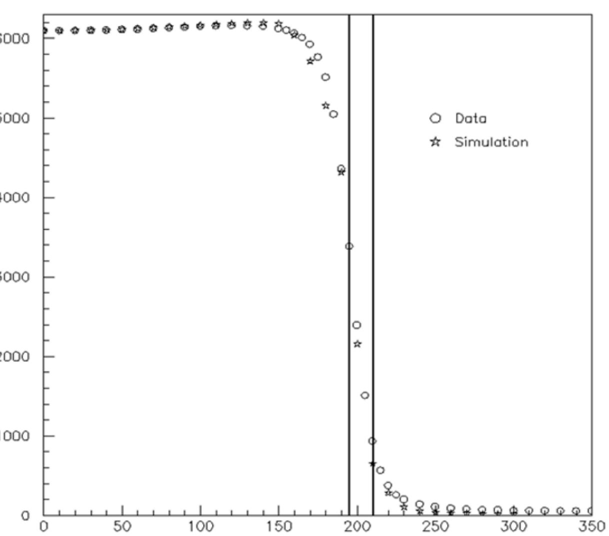

Figure 1.64: KLOE longitudinal field component (Gauss) along magnetic axis (cm, 0-value is the center of the barrel). The MagAx measurements are compared with the Monte Carlo simulation.

1.2.1.1 Coil Shell and Conductor

Oxford Instruments decided for a design of the coil shell to be fabricated from a number of 12 mm thick aluminum sheets and cooling channels. The design relied on achieving the diametrical tolerances (fixed by INFN to ± 8 mm) by fabricating it on an adjustable spider that allowed the ribs to be moved around until the tolerances were met. The inner skin was fully welded to the ribs whilst the outer was partially welded. No machining took place on the shell although the inner welds were all hand dressed. This approach was very successfully carried out by Vosper Thorneycroft (Southampton, UK). This new design of coil shell was designed, manufactured and delivered in 6 months thus minimising the delay (coming from a contractor substitution decided by Istituto Nazionale di Fisica Nucleare (INFN)) to the system manufacturing schedule.

The conductor is a 10 mm by 5 mm composite consisting of a Rutherford cable co-extruded with high purity aluminum. The conductor, provided by LMI (lmi-srl.it), was cleaned and then wrapped with two half lapped layers of 0.125 mm glass tape. The two-layer coil was wound inside the coil shell by rotating the shell on motorized rollers in a controlled manner whilst the conductor was fed in and directed on to the shell face from a spool mounted off the winding machine.

The conductor was wound on flat and between the two layers 1 mm thick high purity aluminum sheets were placed in order to improve propagation velocities and reduce the peak quench temperatures. After winding, the coil was lined with aluminum, to act as an impregnation vessel, before being turned axis vertical and placed inside a 7 m cubic impregnation oven. The aluminum liner was supported against collapse by a fabricated support structure before the coil space was evacuated, filled with epoxy and then cured at 100° C for 48 hours.

1.2.1.2 Radiation Screen

The radiation screen will be cooled by helium gas from the dedicated refrigerator. The inner and outer radiation screen cylinders are simple end cooled screens each constructed from eight prefabricated panels - each panel consists of three components - two 1 mm thick flat aluminum sheets and one 1 mm thick corrugated aluminum sheet. The three components are all bonded and riveted together on a former of the correct diameter in a sandwich construction consisting of flat sheet - corrugated sheet - flat sheet. The cooling pipe is welded to the panels over a length equivalent to 30% of their circumferential extent. This minimal approach to the cooling of the radiation screens is possible only as a result of the extremely low radiant and conducted heat loads. The guaranteed heat load is given in Tab. 1.16.

Table 1.16: Guaranteed Heat Loads.

Source	Heat Load
Current Leads	0.6 g/s
4 K Radiation and Conduction	55 W
77 K Radiation and Conduction	530 W

The screen is supported from the vacuum case by stainless steel cables.

1.2.1.3 Service Turret

The space available for the service turret was very restricted due to the need to minimize the cut out in the iron and the very restricted height. The service turret provides the following functions:

- supply and control of LHe
- 150-liter helium storage volume
- supply and control of 70 K helium for radiation screens gas cooled
- 3 kA current leads from 300 K
- instrumentation connections to the coil and radiation screens

The delay in the settlement of some of the design issues at the time of designing process meant that connections to the refrigerator were finalized after the service turret was in manufacture. This, coupled with a lack of space forced by the need to minimize the iron cut-out, has led to a need for a separate valve box. This was designed as to be mounted on top of the iron and contains a number of valves to facilitate safe and easy connection to the refrigerator.

1.2.1.4 Power Supply and Control Instrumentation

The power supply was originally to be a thyristor controlled switch mode system. However, because of concern about electromagnetic interference with the experimental detectors a series regulated supply designed for low EMI has been provided. The control and instrumentation can be subdivided as shown in Tab. 1.17. The system has distributed control with centralised monitoring via Labview.

Table 1.17: Power Supply and Control Instrumentation.

Overall control + monitoring	Labview running on Pentium PC
Temperature measurement	Oxford Instruments ITC-600
Helium valve control	Weka valve controlled by Labview driver
Current leads control	Northvale Korting Bossmatic valve controlled by separate P&ID controller

1.2.2 Magnet Maintenance and Revamping Options

The KLOE magnet was in operation at the LNF up to the December 2018. From the fluidic operation point of view the system has in general operated in a smoothly way, with only a major non scheduled shutdown of 2 months from the summer 2010 caused by a “silly” VCR gasket producing a He leak (undetectable by the vacuum gauges) from the 4.4 K line toward the insulating vacuum.

In principle, from the P&ID (Pressure & Instrument Diagram) point of view, the magnet has only 3 actively controlled devices, namely

- The Joule-Thomson valve aimed at maintaining the LHe at set point in the magnet turret
- The valve controlling the He flow in the Current Leads
- The heaters preventing frosting at the warm side of the Current Leads

The replacement of all these subsystems together with all the Teflon gasket of the cryogenic valves is foreseen.

The power supply in the last years of operation suffered from aging of some components. First of all, the cooling pipes of the transistors bank and of the free wheeling diodes are affected by several water leaks and the PS control system based on an old LabView version (3.0) needs a revamping. Nevertheless, several passive components (i.e. inductance, dump resistors, etc.), high currents contactors and the bus bars that was tailored on the overall dimensions constraints can be saved after proper functionality tests. This option will allow a significant cost savings guaranteeing at the same time a perfect compatibility with all the magnet apparatus environment, in particular all the busbars connected to the PS output terminal could remain the same as well as the overall dimensions and PS location.

Therefore, INFN is finalizing a market survey among several companies with a few years expertise in power converters and who had already provided power supplies with satisfactory performances for INFN. The required PS performances are the same of the old power converter and they are resumed in Table 1.18. The new PS must have several configurations that will cope all the fault scenarios, that will be later presented.

1.2.2.1 Magnet Power Supply Overview

After discussions with several companies, a basic PS scheme has been defined, It is shown in Fig. 1.65 where three one quadrant power converter modules (1000 A, 10 V) are connected in parallel aiming to reach a maximum current set of 3000 A. The three modules will work with one master and two slaves configuration and will communicate between them by optical fibers. This solution will ensure a redundancy and a higher reliability in case of fault. Each module is connected in series with a diode that will save the module in case of output voltage unbalanced avoiding energy flow between the modules. During the normal magnet operations, the contactors T1 and T3 are closed while T4 and T2 are opened.
In the event that the magnet loses its superconducting state, all the magnet stored energy (about 14 MJ) must be removed as rapidly as possible. Loss of superconducting state is detected by the quench detector and this triggered an energy dump circuit (OCB rundown) within the magnet power supply. The energy is dumped into the permanently connected 85 mΩ resistor "Dump Load". At the nominal power supply terminal voltage this resistor dissipates very little energy, however, when the Quench Signal is sent, T3 contactor breaks the connection from the power supply output to the magnet. The magnet current then decays with a time constant of 50 s. The circulating current in the magnet is now forced to flow through the resistor causing the bus bars to the magnet to rise to about 250 V. The diode D4 ensures that no current will flow through the dump resistor when the magnet is in superconducting state.
Other less severe failures with the magnet at field are also catered for in the power supply design, i.e. in the event of a power supply main power internal PS failure, the contactor T1 is opened, with T4 and T2 who keeps their normal open state, and the current start to flow through a stack of freewheel diodes (all the ones from D5 to D12) maintaining the magnet current path and cause the magnet to ramp down gently (FWD rundown) over a period of approximately 20 minutes. During the nominal magnet ramp up the three modules provide a 0.6 A/s current ramp while for the ramp down, since the PS modules are 1-quadrant type, the T4 contactor is closed with the T1 opened creating a by pass of the freewheel diodes from D5 to D10. In this way the current will flow only through D11 and D12 diodes providing a negative voltage of -2 V and allowing a -0.6 A/s current ramp down.
Since all the freewheel diodes will be water cooled, thus these are protected against overheating

caused by cooling water flow failure by T2 contactor: in this scenario it is closed and T1 is opened. In this way it deenergises and 'crowbars' the power supply output (CBD rundown). The magnet current will then decay away over a period of 2.5 hours, the only power dissipation being due to the heating of the magnet bus bars.

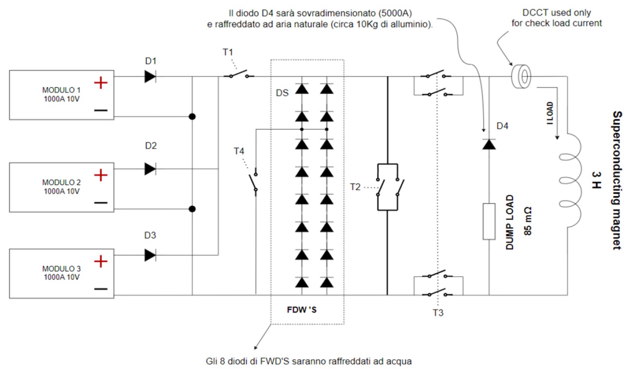

Figure 1.65: Schematic of the new power supply.

1.2.2.2 Uninterruptible Power Supply

All the relays who drive the contactors and the power supply control circuit are all fed from an uninterruptible power supply (UPS) built into the magnet power supply cabinet. The UPS will maintain the power on all the control circuits, including the quench detector unit mounted externally to the power supply in the control rack. The UPS will continue to power these important circuits for more than 30 minutes, allowing the freewheel diode run-down to be completed.
In the event that the UPS fails, the quench breaker contactor T3 will open and any residual magnet stored energy will be dissipated in the discharge resistor.
In the event that the mains input power failed in conjunction with a cooling water flow failure, then after the UPS eventually fails, there will still be an appreciable stored energy that will then be dissipated in the discharge resistor when the UPS finally runs out of power.

1.2.2.3 Control System Interfaces

The PS control system interfaces architecture will follow the old one of KLOE solenoid PS. The power supply receives interlocks from a number of locations in addition to internal protection interlocks. The interlocks are divided into 3 classes functionally.

- Fast energy dump (OCB), forcing the magnet current through the discharge resistor.
- Freewheel diode run down (FWD), causing the PSU to turn off and forcing the current to decay through the diodes.
- Crowbar rundown (CBD), causing the magnet to run down very slowly on the busbar resistance.

All interlocks are made by providing an external contact closure which is sensed by the magnet power supply's built in 24 V power supply which in turn is fed from the built in UPS. All the contacts will be collected to a board that will be rebuilt in the revamping phase, and also a new PLC will be introduced and configured to manage all the interlocks and to perform an internal control of the PS. Remote computer control is effected via ethernet link to the main control PC, however a local control and a local alarm panel are provided for front panel control of the power supply. The UPS power is fed out to the control rack where it powers the quench detector. The quench detector feeds back signals to trigger a fast energy dump should a quench be detected and to trigger a freewheel diode run down if the current lead voltage drop is excessive.

The control rack also triggers a freewheel diode run down for a number of other conditions detected by the control software. The system monitors the temperature of the magnet current leads. This will trigger a freewheel diode run down initially but if the temperature continues to rise, it will trigger a fast energy dump. The front panel power off and magnet fast energy dump buttons may also be duplicated by two series - connected emergency buttons wired round the experimental area. The helium fridge may be arranged to provide an interlock to trigger a freewheel diode run down and the power supply provides a contact closure which opens to signal a fast energy dump is in progress to coordinate the actions of the rest of the INFN installation.

1.2.2.4 Busbars

The main busbars from the power supply unit to the coil terminals are part of the saved item from the old KLOE magnet. They are of aluminum and are internally water-cooled. The ends of each busbar section are copper plated to provide good, long term electrical contacts and all bolts have disc-springs to maintain the bolting force. The busbars are Kapton-insulated and covered in heat-shrink sleeving for mechanical protection. The joint areas and the water pipe connections are elastomer covered as it is not possible to apply sleeving in these areas. Voltage taps on the busbars allow for identifying higher resistance section of the busbar circuit. The expected busbar voltage.drop is about 300 mV at 2963 A. At each end of the busbar run there are flexible copper braids to ease the assembly and avoid undue forces on the PSU terminals or current lead terminals.

All connections to the PSU and to each end of the busbars are made in insulated water hoses. The nominal water flow rate is 33 l/min and the resistive loss in the busbars is 2.6 kW this gives a rise in temperature in this part of the circuit of 1° C. The loss of water flow is sensed by the indicator within the PSU and appropriate action is taken to reduce current.

1.2.2.5 Quench Detection

The quench detector unit monitors the voltage taps of the magnet and the associated current leads and detects when a quench in the magnet has occurred by looking for any small differential voltages against the background of a large common mode voltage. All the boards, the wires and the quench signals will be deeply tested in the revamping phase, leading to a substitution of all aged parts. The working principle will be the same of the old system where several potential taps are foreseen for both inner and outer coil layers. In details, there are two potential taps at each monitored point on the magnet, this is to give some redundancy, indeed there are two completely separate detector cards in the quench detector unit for the same reason. The outer layer of the coil winding has potential taps at the start (also start of the magnet) and end of the layer, the inner layer then has a potential tap at the end of the layer (also end of the magnet), as well as a potential tap at point part way along the winding. Thus, four potential taps are present, giving three sections of magnet of dissimilar inductances. The quench detector has a precisely adjusted resister chain giving resistance ratios identical to the inductance ratios within the magnet. The voltages across each section of this chain are compared to the voltages across each section of the magnet. During ramping the back EMF across the coil will be in proportion to the inductance, when at field all the voltages will be zero. If a quench occurs the quench normal zone resistive voltage will occur in one, or perhaps two, of these sections, upsetting the balance of the detector and trigger a 'magnet has quenched signal'. The detector is housed in a 19" 3U high unit 1.66 and has up to eight channels (including current leads) which are able to withstand voltages of up to 5 kV on the magnet taps. The unit can also withstand up to 500 V across the magnet terminals during a fast discharge. It is powered by an uninterruptable power supply situated in the power supply cabinet (which also powers the vital PSU control hardware in the event of a power failure). An internal test voltages will be possible during the set-up.

Figure 1.66: Kloe Magnet Diagnostic Rack. The Quench Detector (QD) is marked in red.

1.2.2.6 Warm up Power Supply

The warm up power supply can be used to drive 25 A at up to 230 V into the magnet terminals to bring it up to room temperature once it ceases to be superconducting. This is a small current controlled unit, it must be wired into circuit and the magnet bus bar removed before it can be used. The warm up power supply must always be switched off in normal operation. It is only powered up following disconnection of the main magnet circuit which would otherwise short circuit the warm up power supply output through the discharge resister.

1.2.2.7 Power Supply Revamped and Saved parts

The power supply revamping operations will involve mainly the power unit that will be totally substituted with AC/DC power modules in parallel (probably three) including all their DCCT and control unit. The communication of the modules is based on Modbus TCP/IP Ethernet interface. Also the input power will be compliant with the USA standard (208V 3-phase voltage at 60 Hz frequency) while for the tests at LNF a dedicated front end will be used. The new power units will replace all the old transistor banks who work for a long time and they are not still available due to several water leakages on water cooling circuit.

Another relevant intervention will be the installation of two new contactors indicated as T1 and T4 in Fig. 1.65 devoted to the disconnection of the power units from the load and to by-pass several diodes for adjusting the current ramp down in case of FWD rundown or normal 0.6 A/s ramp-down. All the diodes shown in Fig. 1.65 will be new and they will be indirectly water-cooled by new aluminum plates and pipes. The warm up and UPS power supplies will be replace with new ones and a new interlock board will be designed, according to the old scheme, collecting all the signal from the diagnostic rack. A new PLC for the signal management and internal control of the will be installed.

Concerning the control system, this will be based on LabView with the same main functions of the previous one who was built on LabView 3.0. This task will be covered by one of the companies with a long, positive experience with INFN in the automation field. Concerning the saved parts, first of all there will be the contactors T3 and T2 (visible in Fig. 1.65) after several functional test performed by the company who will provide the power converter. Also the dump resistance and all the passive devices who are still preserving their nominal parameters will be saved after functional tests. The original DCCT head with its electronics will be object of a survey, indeed if it still work it will be used for a diagnostic of the load current: if there is a mismatch between the sum of the three currents readout of the three power unit DCCT with the DCCT upstream the load, the control system will give back a warning signal.

The old busbars connected to the magnet will be saved keeping the original voltage drop and avoiding changes in the PS cabinet position and configuration.

All the new and revamped parts will be hosted in a cabinet with the same dimensions of the previous one. Fig. 1.67 shows the current PS cabinet with its overall dimensions.

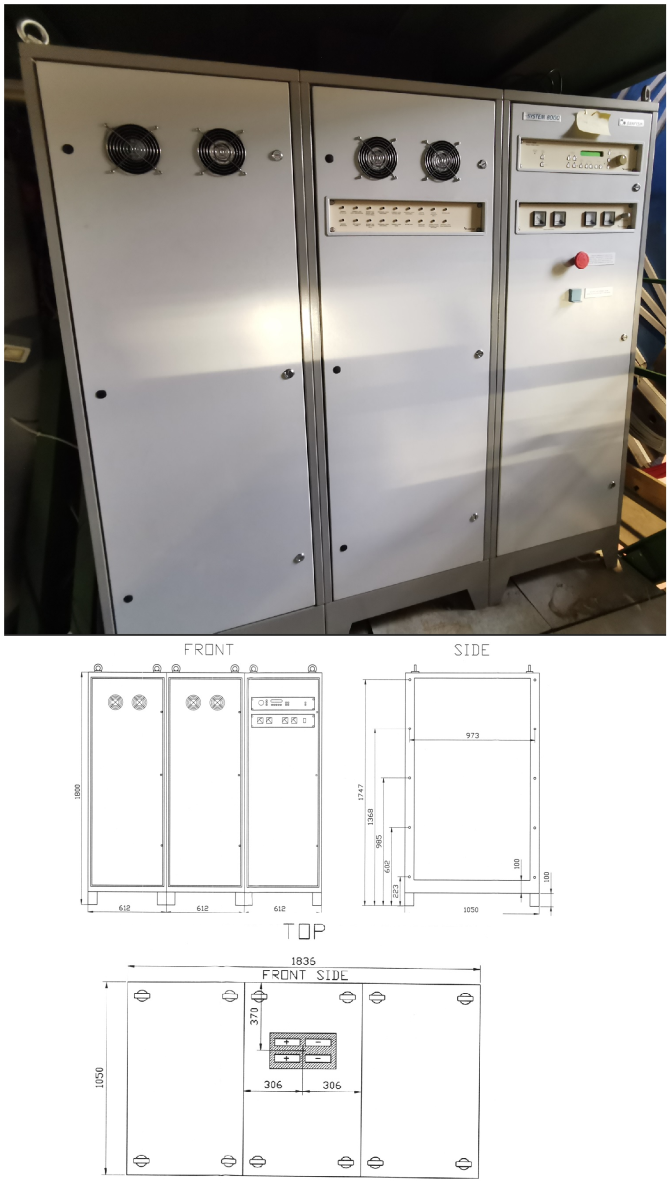

Figure 1.67: KLOE Magnet Power Supply Cabinet (on top) with its overall dimensions (on the bottom).

Table 1.18: Power Supply requirements.

DC OUTPUT RATINGS	
Power Range	30 kW
Current range	3000 A
Maximum output Voltage	10 V
Nominal Ramp Rate	0.6 A/s
Output Polarity	Unipolar
STABILITY ⋆	
Short term 30 min	± 10 ppm
Long term 8 hours	± 10 ppm
WATER COOLING	
Flow Rate	18-25 l/min
Inlet Water Temperature	$25-32°$ C
Current setting resolution	18 Bit
Current readback resolution	16 Bit 16 ppm
AC SUPPLY POWER	
Mains voltage	3×208 VAC ±10% 60 Hz (With 400 VAC connection for LNF Tests)

⋆ These are nominal PS parameters, with the 3H magnet load they will be improved

1.2.3 Activities at Laboratori Nazionali di Frascati

Before the magnet shipment an operational test will be performed, to confirm the integrity of the magnet. The activities are listed below:

1. Warm test - System vacuum check. Pressure test of safety valve. Leak test of pipes connection and LHe tank. Valves hydraulic and actuators test. Insulation test of the pressure, temperature and LHe level sensors

2. Cold test - Cooling of the magnet from 300 K down to 4.2 K. Functional test of the sensors at LHe temperature and coil insulation. Protection system check. Thermal loss measurement

3. Commissioning of the new Power Supply and Control system

4. Coil energizing - Sensors check. Heat loss at steady state. Coil de-energizing and warm-up

5. Final functionality check back to 300 K

At the end of tests before the shipment to Fermilab the service turret must be removed because of the interference with the hall door. The process can be summarized as in the following:

1. disconnection of the signal sensors cable (air side);

2. removing of the cylindrical shell of the vacuum case;

3. removing of the MLI (Multi Layer Insulation);

4. disconnection of the signal sensors cable (vacuum side);

5. disconnection of the coil terminals;

6. cutting of the 4 cryogenic lines.

The turret will be reconnected at Fermilab and the procedure (to be used in the reverse sequence for the turret removal) is described in the drawing from Oxford Instrument AJL0550 "Service Turret Assy KLOE" sheet 1 to 5. Due to the nature of this operation INFN will award a contract to ASG Superconductors to perform the entire process of removal and reconnection at Fermilab of the service turret.

The tests will be performed again at Fermilab before the re-installation in the iron yoke to exclude any damage during the transportation.

1.2.3.1 Magnet cool down

The options of reconnecting the magnet to the Linde TCF 50 refrigerator or to cool down the magnet by direct filling with cryogenic liquids has been investigated. In the following the evaluation for the two options is reported.

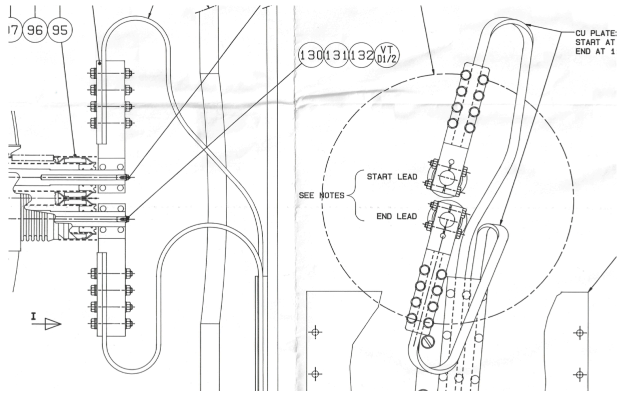

Figure 1.68: KLOE coil leads clamp detail.

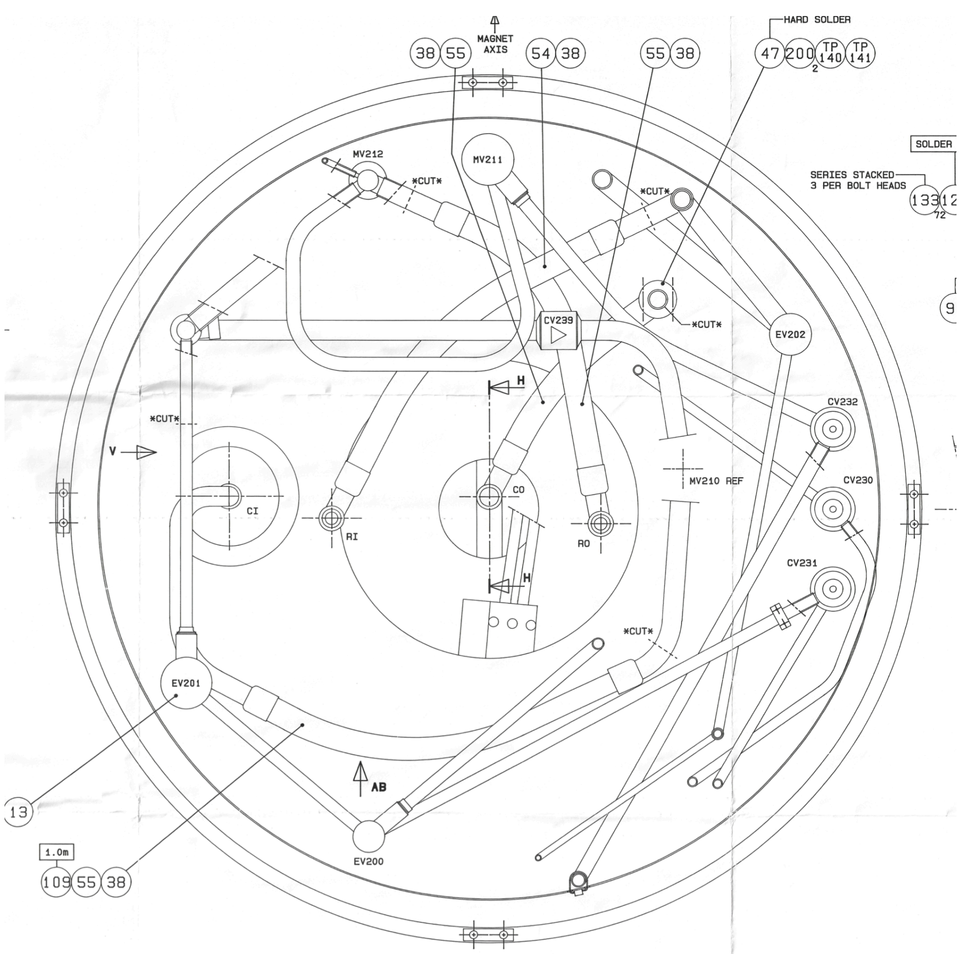

Figure 1.69: KLOE pipes cutting for service turret removal.

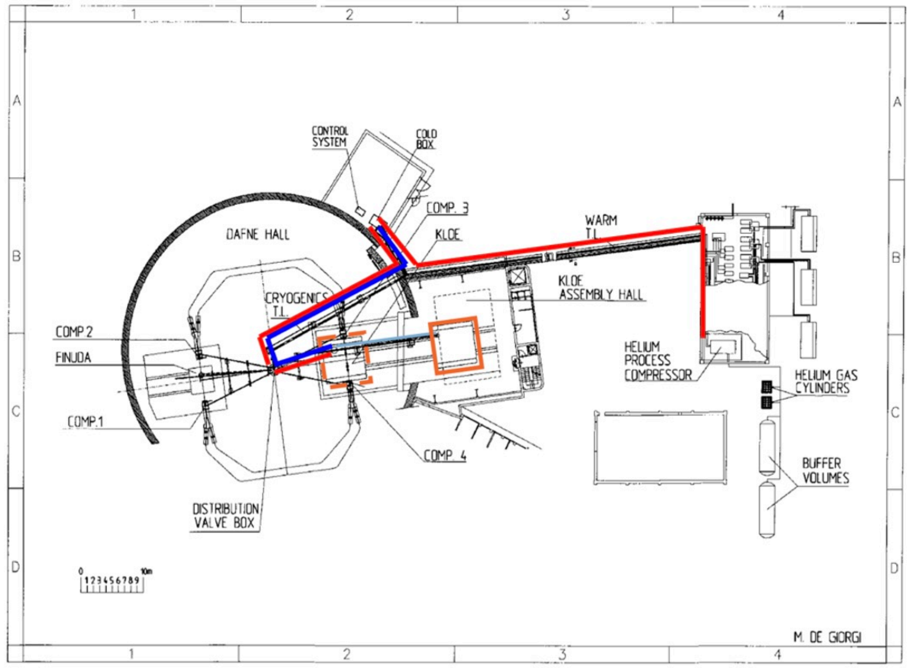

Figure 1.70: Plant layout for the KLOE cooling with existing refrigerator.

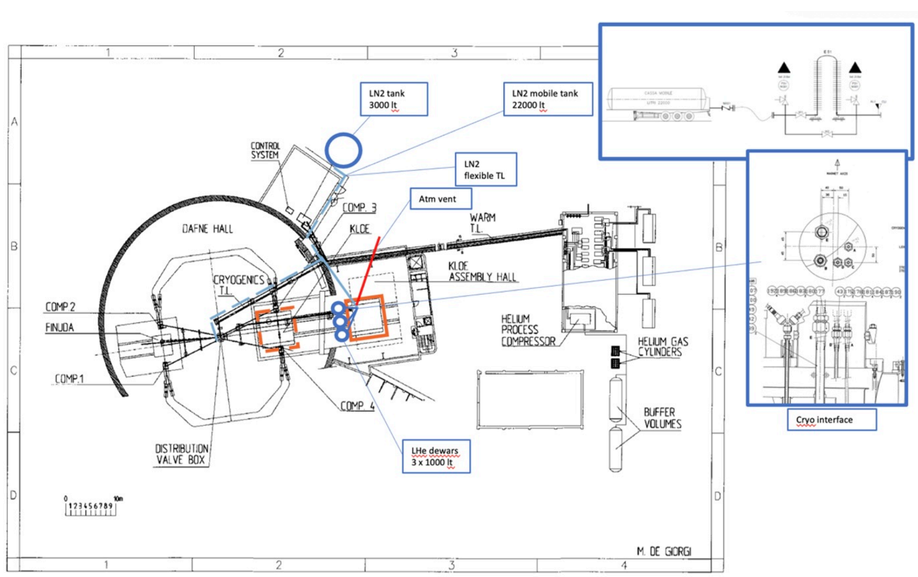

Figure 1.71: Plant layout for the KLOE cooling with cryo liquids.

Magnet cooling with existing refrigerator The KLOE magnet has been cooled down out of the beam in 1997. During the years the transfer line (TL) extension as well as the bridging system aimed to its support have been dismissed and in case must be procured once again. Pros and cons of this option are listed here:

- Pros
  1. Very well-known process, performed several times by LNF personnel from 1998 to 2018.
- Cons
  1. Requires nontrivial re-manufacturing/re-installation of KLOE TL extension + bridging;
  2. Requires full re-installation of the fluidic subsystems;
  3. Requires cryo plant to be put back in service after 5 years just for a few weeks' operation;
  4. Most of the listed hardware and services are not useful to repeat the test in the US.

Magnet cooling using cryo liquids The KLOE magnet has been cooled down out in Oxford Instrument in 1996 before shipment to Italy. The process is briefly described in [12].

- Pros
  1. It requires very limited re-installation of the original fluidic subsystems LN2 flexible TL already in place (with 3000-liter LN2 tank for preliminary test);
  2. LHe dewars are available in house (3000 liters);
  3. It requires the manufacturing of non-complex cryogenic interfaces;
  4. The hardware is self consistent to repeat the test "keys in hand" before magnet re-integration in the yoke at Fermilab.
- Cons
  1. Process performed only once in Oxford by Oxford Instrument personnel before 1996;
  2. To extend/repeat the test could increase the costs consistently.

After careful consideration of what previously reported the option of cooling the magnet with cryo liquids has been selected and some services and goods have been procured or the administrative process for the orders has been concluded.

INFN is negotiating with ASG Superconducting the support in the test activities, a mandatory activity being the case of re-procurement of power supply, quench detector and control system. Support in the task of the magnet turret removal is another critical activity that INFN has requested to be supported by ASG Superconducting.

1.2.3.2 Coil Cryostat extraction

The extraction and handling operations of the Coil Cryostat will take place inside the KLOE experimental hall at LNF, while the preparations for transport will be carried out in the yard in front of the building. The Coil Cryostat is a cylindrical structure measuring 5.8 meters in diameter, 4.4 meters in length, and weighing approximately 40 t. It is installed inside the support structure (hereinafter referred to "Yoke") of the KLOE apparatus. To remove and transport it to Fermilab, a series of equipment is required to allow the Coil Cryostat to slide out of the Yoke and, at the same time, be lifted and positioned onto the loading platform to enable its exit from the assembly hall. The main equipment that will be used to complete all the necessary operations for the extraction, lifting, and transportation of the Coil Cryostat includes:

- The Insertion/Extraction rails (Fig. 1.72, left).
- The Handling Cradle (Fig. 1.72, center).
- The Transport Cradle (Fig. 1.72, right).

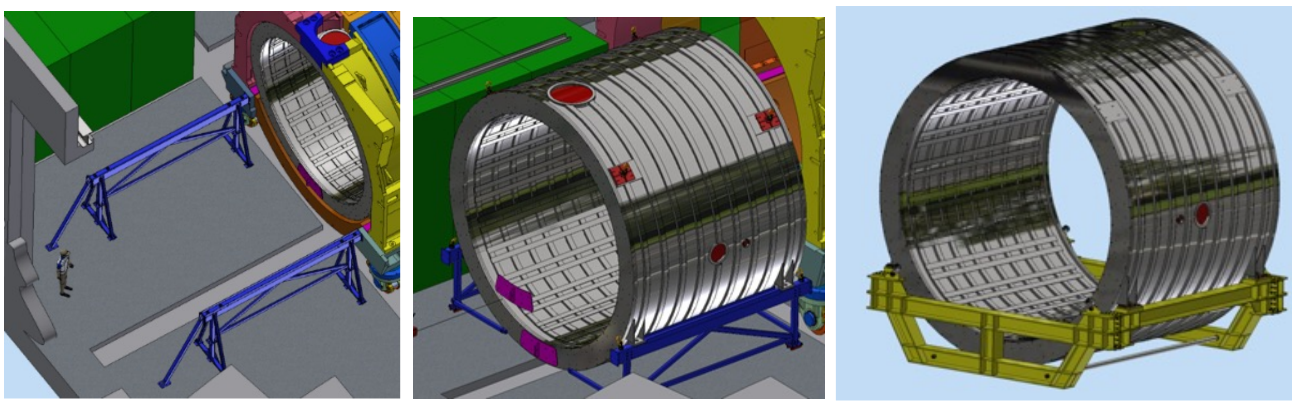

Figure 1.72: Tools for extraction, transport and insertion of the coil. Left: insertion/extraction rails. Center: handling cradle. Right: transport cradle.

The procedure for removing the Coil Cryostat from the KLOE apparatus can be summarized in the following steps:

1. Preparation of the work area.
2. Assembly of the extraction/insertion rails.
3. Assembly of the pulling system (Tirfort© System).
4. Extraction of the Coil Cryostat from Yoke.
5. Lifting and moving the Coil Cryostat to the parking area.
6. Assembly of the loading platform and rails.
7. Lifting and moving the Coil Cryostat onto the loading platform.
8. Moving the Coil Cryostat outside the KLOE hall.
9. Moving the Coil Cryostat into the transport cradle.
10. Moving the Coil Cryostat onto the truck.

To extract the Coil Cryostat from the Yoke, it is necessary to install two rails on which the Coil Cryostat can slide while being pulled from below by a mechanical system.

For safety reasons, to prevent the Coil Cryostat from sliding out uncontrollably, it will be held on the opposite side by a similar mechanical system. As soon as the Coil Cryostat is completely extracted from the Yoke, the four lifting points will be installed. The Coil Cryostat will be connected to the overhead crane, lifted to allow the removal of the roller skids, placed back on the rails, and secured to them.
The Coil Cryostat along with the rails will be lifted to remove the extension of the legs supporting the rails. The bracing bars will be installed, and the Coil Cryostat with the Handling Cradle will be repositioned on the floor.
Since the space between the overhead crane hook and the lifting points is insufficient to lift the Coil Cryostat onto the loading platform directly, the crane slings will be attached directly to the Handling Cradle. Subsequently, the Coil Cryostat-Handling Cradle assembly will be moved inside the hall to facilitate the installation of the loading platform, which was previously removed to enable the extraction operations of the Coil Cryostat.
As soon as the loading platform is installed and ready to receive the load, the Coil Cryostat will be moved onto the platform and taken out of the room by sliding it on special rails.
Once the Coil Cryostat is outside the KLOE hall, it will be placed into the Transport Cradle using two mobile cranes and loaded onto the truck.

1.2.3.3 Dismounting of Iron Yoke

The iron yoke of the KLOE magnet has a global weight of 600 t. It is composed of 32 pieces, the heaviest having a weight of 20 t.
A specialized company in large mechanical assemblies took care of mounting the yoke for the KLOE experiment in 1997. The same company will be contracted to dismount the yoke at LNF, including the ancillary operations needed for the extraction of the coil cryostat from the yoke, all coordinated by INFN personnel, and to re-mount the yoke (and coil) at Fermilab, once ready to be installed in the ND Hall, according to the schedule of the project.

1.2.3.4 Tools, Packaging & Shipping to Fermilab

The main tools necessary to complete the extraction, handling, and transportation operations of the Coil Cryostat are listed in the Table 1.19.

The Coil Cryostat, protected by a waterproof cover, will be transported by land to the port closest to the LNF and then loaded onto a specially equipped ship for transport. Unloading the Coil Cryostat from the truck and loading it onto the ship will be done using a mobile crane.
The Insertion/Extraction system and lifting points will be shipped to Fermilab along with the Coil Cryostat and the Transport Cradle.

1.2.4 Installation & Integration at Fermilab

The KLOE magnet is provided with 180 liters of LHe reservoir aimed to limit its temperature below 20 K in case of a quench, so it must comply Fermilab internal regulation. Cryogenic tanks at Fermilab must be designed, fabricated, tested, and operated according to Fermilab “FESHM 5031: PRESSURE VESSELS” internal standard.

Since the magnet has been built almost 30 years ago (posing issue about different design & manufacturing standards and lack of records like material certificates and test reports) the point 4 of

Tool	Description	Purpose
	Elevating platform (H = 10 m)	Assembly of the lifting lugs and slings
	Overhead crane and related accessories (ropes, eyebolts, and so on)	Handling of coil cryostat and heavy materials
	Various tools	Assembling
	Tirfor©	Extraction/insertion of coil cryostat
	Clark	Extraction/insertion of coil cryostat
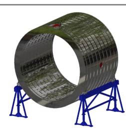	Extraction/insertion tools	Extraction/insertion of coil cryostat
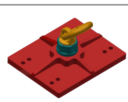	Lugs	Handling of coil cryostat
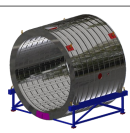	Trolley	Handling of coil cryostat
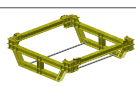	Cradle	Transport of coil cryostat
	Mobile crane	Handling of coil cryostat
	Transpallet	Handling of components

Table 1.19: Tools for handling of coil cryostat.

the procedure "*Exceptional Vessels / Director's Exception*" shall be applied:

Exceptional vessels is a process that requires the approval of the Laboratory Director or his/her designee. An Extended Engineering Note shall be prepared including the following information:

a. Reason for Exception: Division/Section/Project Head or designee shall provide a ES&H Manual FESHM 5031 September 2021 Fermilab ES&H Manual 5031-13.

b. Analysis/Burst Test: For exceptions based on stresses above code allowable stresses, the system designer shall provide a stress analysis of all exceptional parts of the vessel. Include data, formula or test results which demonstrate the anticipated safety factor. Source of information shall be referenced. Alternately, provide burst test data from samples demonstrating the anticipated safety factor. In cases where a vessel is exceptional because the relief system does not conform to the ASME BPVC, provide calculations or test results as appropriate to demonstrate the venting system capacity exceeds the maximum required flow rate.

c. Fabrication: The system designer shall provide a fabrication procedure, a list of planned and completed inspections and any other quality control procedures taken including, but not limited to the weld or braze procedure specification, the procedure qualification and the welder or brazer performance qualification records

d. Hazard Analysis: The system designer shall provide a description of personnel hazards associated with vessel operation and the methods used for protection. The hazard analysis shall address vessel application, operating limits and controls, possible effects in the event of vessel failure and inherent safeguards provided.

e. Pressure Test: A pressure test shall be performed per Chapter 5034 of the Fermilab ES&H Manual.

f. The division/section/project head or designee shall provide a written record of the decisions, judgment, tests, administrative controls, and hazard analyses that were necessary to approve this type of vessel.

1.2.4.1 Storage at Fermilab

The Coil Cryostat must be stored inside a building, while the tools can be stored outdoors if adequately protected to prevent degradation due to environmental factors.

The magnet (the cryostat with the superconducting coil inside) will be initially located in D0 Assembly Building (DAB) where detector components located inside the magnetic volume will be installed. The resulting assembly will then be moved to the DUNE-ND experimental hall for the final installation.

1.2.4.2 Tools and Mounting Procedure

The Coil Cryostat will be installed at Fermilab in the SAND experimental apparatus. The same extraction equipment used at LNF will be employed. The installation procedure will follow the reverse process of the extraction:

1. Preparation of the work area;
2. Assembly of the insertion rails;
3. Assembly of the pulling system (Tirfort© System);
4. Moving the Coil Cryostat into the SAND assembly hall;
5. Moving the Coil Cryostat from the transport cradle to the insertion rails;
6. Inserting the Coil Cryostat into the Yoke;
7. Removing of the insertion rails.

1.2.4.3 Cryogenic Refrigeration Plant for Continuous Operation

The impact of the procurement of a new refrigeration plant to be installed at Fermilab is under investigation. The most natural action is to ask Linde, the provider of the TCF 50 which has supplied the KLOE magnet for almost 20 years in a reliable way.

The company has been contacted and declared that TCF 50 is no longer in their catalogue. They have provided a preliminary offer for a plant with a reduced cryogenic power, due to the fact that in DUNE the cryogenic load will be lower than that required by DAΦNE [13, 14] and the compensator magnets will not be present.

1.2.5 Risk Management

The topics covered in Sec. 1.1.9 about the risks in dismantling, shipping and reassembly of the KLOE detector are not repeated here. However, it is necessary to stress that the risk analyses mostly focus on possible damages occurring during the transport from LNF to Fermilab. Furthermore, it has to be noted that the magnet was transported from Great Britain, where it was built, to LNF by truck and by ship (through the Atlantic ocean and the Mediterranean sea) without suffering any damage.

1.2.5.1 Detailed risk analysis

1. Event: Leak (fissure) on the magnet cryostat
   - Possible causes - Shock, bump or vibrations occurred during the transport.
   - Possible consequences - Inoperability of the magnet. Localization and repair of the leak requires access to the cryostat surface. If detected during the commissioning, location and repair require partial disassembly of the yoke and, potentially, extraction of the magnet and removal of internal detector components. These operations cannot take place in the alcove. The estimated time for the operations ranges from 6 months: (un-cabling, move to the cavern, yoke partial disassembly, leak localization and repair,

re-assembly, re-cabling) to 12 months (add to the previous list removal of the magnet, extraction of detector components, re-insertion of detector components and of the magnet in the yoke). The occupation of the main cavern space, with interference/disruption of activities of other ND detectors, would be 3 to 9 months.

- Estimated Probability - Moderate, 2% to 5% (from long distance transport statistics).
- Detection - Visual inspection after delivery to , check the recording of the accelerometers. Vacuum pumping of the cryostat and helium leak checking.
- Intervention- Seal the leak(s) by welding, re-test the vacuum tightness.
- Mitigation - Detailed engineering of the transport with shock and vibration analysis, definition of maximum accelerations, of maximum speeds of road transport, definition of supports and shock absorbers. Transport with online shock logs and periodic checkpoints. Choice of carrier with highest reliability for special transports. Early detection by inspection and vacuum tightness test upon arrival at Fermilab and before installation of detector components in the magnetized volume.

2. Event: Leak on the internal cooling circuit.

- Possible causes - Loose connection on one of the internal interfaces inside the turret. Shock, bump or vibrations occurred during the transport causing a crack in the piping.
- Possible consequences - The leak will result in a loss of the cryostat insulation vacuum. Inoperability of the magnet. Localization of the leak requires access to the turret, which in turn would require a partial disassembly of yoke, if the magnet is installed in the final configuration. If the leak is located in one of the internal interfaces, inside the turret, repair will only require access to the turret and re-testing of the circuit. If the leak is on the heat exchangers, inside the cryostat, repair would require opening of the cryostat and extraction of the internal coil with the radiation shields. Subsequently, there will be an investigation/assessment of the damage followed by the study of the necessary repair or substitution and by its implementation. This is a major work that, most likely, cannot be done effectively onsite and would therefore require the transfer of the magnet to an external company. If detected during the commissioning, location and repair require partial disassembly of the yoke and, potentially, extraction of the magnet and removal of internal detector components. These operations cannot take place in the alcove. The estimated time for the operations ranges from 6 months: (un-cabling, move to the cavern, yoke partial disassembly, leak localization and repair, re-assembly, re-cabling) to 24 months (add to the previous list removal of the magnet, extraction of detector components, transfer of the magnet to an external company, repair, test, return to Fermilab, re-insertion of detector components and of the magnet in the yoke). The occupation of the main cavern space, with interference/disruption of activities of other ND detectors, would be 3 to 9 months.
- Estimated Probability - Moderate: leak at the internal interfaces; $\sim 5\%$. Very low: leak on the radiation shields
- Detection: Visual inspection after delivery to Fermilab, check the recording of the accelerometers. Monitor the vacuum level in the cryostat while injecting Helium inside the cooling circuit.
- Intervention: Seal the leak by tightening or replacing the connections inside the turret

if the leak is located there, repair by external company otherwise. Re-test the tightness at room temperature prior re-installation as appropriate.

- Mitigation: Detailed engineering of the transport with shock and vibration analysis, definition of maximum accelerations, of maximum speeds of road transport, definition of supports and shock absorbers. Transport with online shock logs and periodic check-points. Early detection by flowing nitrogen first and then helium in the circuit and cooldown to liquid nitrogen or to liquid helium temperature after delivery to Fermilab and before the installation of internal detector components.

3. Event: Break or short in the superconducting coil

- Possible causes - Loose connection on one of the internal interfaces inside the turret. Shock, bump or vibrations occurred during the transport causing a deformation or break of the coil.
- Possible consequences - Inoperability of the magnet. Localization of the break/short requires access to the turret, which in turn would require a partial disassembly of yoke, if the magnet is installed in the final configuration. If the break is located in one of the internal interfaces, inside the turret, repair will only require access to the turret and re-testing of the circuit. If the break/short is on the coil, inside the cryostat, repair would require opening of the cryostat and extraction of the internal coil with the radiation shields. Subsequently, there will be an investigation/assessment of the damage followed by the study of the necessary repair or substitution and by its implementation. This is a major work that cannot be done effectively onsite and would therefore require the transfer of the magnet to an external company. If detected during the commissioning, location and repair require partial disassembly of the yoke and, potentially, extraction of the magnet and removal of internal detector components. These operations cannot take place in the alcove. The estimated time for the operations ranges from 6 months: (un-cabling, move to the cavern, yoke partial disassembly, leak localization and repair, re-assembly, re-cabling) to 30 months (add to the previous list removal of the magnet, extraction of detector components, transfer of the magnet to an external company, repair/substitution, test, return to Fermilab, re-insertion of detector components and of the magnet in the yoke). The occupation of the main cavern space, with interference/disruption of activities of other ND detectors, would be 3 to 9 months.
- Estimated Probability - Moderate: loose connection at the internal interfaces; $\sim 2\%$. Very low: coil break/short.
- Detection - Visual inspection after delivery to Fermilab, check the recording of the accelerometers. Monitor the current flow in the coil.
- Intervention - Check and adjust the connections inside the turret if the break is found there, repair/substitute by external company otherwise. Re-test the coil prior to delivery at Fermilab as appropriate. Re-test at Fermilab prior installation of the internal detector components.
- Mitigation - Detailed engineering of the transport with shock and vibration analysis, definition of maximum accelerations, of maximum speeds of road transport, definition of supports and shock absorbers. Transport with online shock logs and periodic check-points. Early detection by operating the magnet in superconducting mode at low current

after delivery to Fermilab and before the installation of internal detector components.

4. Event: Malfunctioning or break of the main power supply (new equipment).

    - Possible causes - Infancy defect. Damage due to transport.
    - Possible consequences - Inoperability of the magnet. If detected during the commissioning it would result in a stop of the commissioning for the time required for repair/substitution. The lost time for substitution, as the power supply is a custom product, could range from 8 to 12 months.
    - Estimated Probability - Moderate $\sim 2\%$
    - Detection - Operate the unit and monitor the current flow.
    - Intervention - Remove the unit. Assess the problem in the lab and define the required repair or substitution.
    - Mitigation - Early detection by stress testing the power supply in the lab before installation.

5. Event: Issue on the service cryogenic equipment (cryo box, valve box, interfaces, cryo controls).

    - Possible causes - Infancy defects. Damage due to transport.
    - Possible consequences - Inoperability of the magnet. If detected during the commissioning it would result in a stop of the commissioning for the time required for repairs/substitutions/modifications. The lost time for these activities can take up to several months if some rebuild of cryogenic components is required.
    - Estimated Probability - Moderate: 2% to 5%
    - Detection - Operate the unit and monitor the behavior through the control system.
    - Intervention - Assess the problem in the lab and define the required repair, substitution or modification.
    - Mitigation - Early detection by pre-commissioning the plant.

1.2.5.2 Schedule and Milestones

The time-schedule for the magnet dismounting and shipping is summarized in Fig. 1.73.

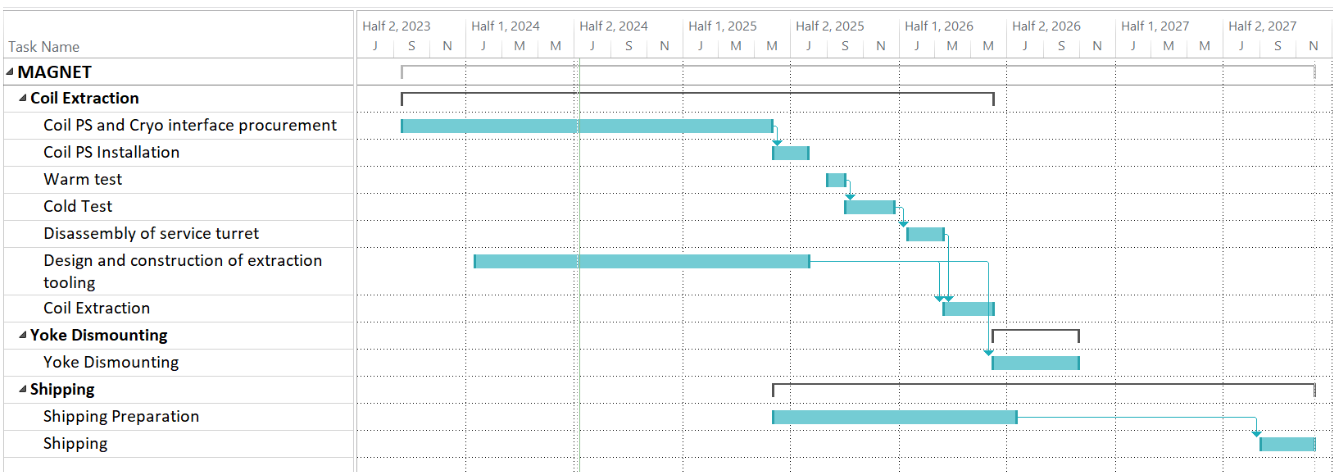

Figure 1.73: GANTT for the magnet dismounting and shipping.

Glossary

analog-to-digital converter (ADC) A sampling of a voltage resulting in a discrete integer count corresponding in some way to the input. 61

ASIC application-specific integrated circuit. 31

European Organization for Nuclear Research (CERN) The leading particle physics laboratory in Europe and home to the ProtoDUNEs. (In French, the Organisation Européenne pour la Recherche Nucléaire, derived from Conseil Européen pour la Recherche Nucléaire). 31

conventional facilities (CF) Pertaining to construction and operation of buildings and conventional infrastructure, and for LBNF and DUNE project (LBNF/DUNE), CF includes the excavation caverns. 92

data acquisition (DAQ) The data acquisition system accepts data from the detector front-end (FE) electronics, buffers the data, performs a trigger decision, builds events from the selected data and delivers the result to the offline secondary DAQ buffer. 31, 44, 91, 93

Deep Underground Neutrino Experiment (DUNE) A leading-edge, international experiment for neutrino science and proton decay studies. 92, 93

far detector module The entire DUNE far detector is segmented into four modules, each with a nominal 10 kt fiducial mass. 93

far detector (FD) The 70 kt total (40 kt fiducial) mass liquid argon time-projection chamber (LArTPC) DUNE detector, composed of four 17.5 kt total (10 kt fiducial) mass modules, to be installed at the far site at Sanford Underground Research Facility (SURF) in Lead, SD, USA. 92, 93

front-end (FE) The front-end refers a point that is "upstream" of the data flow for a particular subsystem. For example the single-phase (SP) front-end electronics is where the cold electronics meet the sense wires of the TPC and the front-end data acquisition (DAQ) is where the DAQ meets the output of the electronics. 91

FEE front-end electronics. 24, 31, 44, 61

Fermi National Accelerator Laboratory (Fermilab) U.S. national laboratory in Batavia, IL. It is the laboratory that hosts Deep Underground Neutrino Experiment (DUNE) and serves as its near site. 47, 92

far site conventional facilities (FSCF) The conventional facilities (CF) at the DUNE far detector site, SURF. 93

fiducial volume (FV) The detector volume within the time projection chamber (TPC) that is selected for physics analysis through cuts on reconstructed event position. 12

high voltage (HV) Generally describes a voltage applied to drive the motion of free electrons through some media, e.g., LAr. 24, 25, 46

Istituto Nazionale di Fisica Nucleare (INFN) Italian institution devoted to nuclear research. 69, 81, 92

KLOE KLOE is a e^+e^- collider detector spectrometer operated at DAFNE, the ϕ-meson factory at Frascati, Rome. In DUNE it will consist of a 26 cm Pb+scintillating fiber ECAL surrounding a cylindrical open detector region that is 4.00 m in diameter and 4.30 m long. The ECAL and detector region are embedded in a 0.6 T magnetic field created by a 4.86 m diameter superconducting coil and a 475 tonne iron yoke. 1, 66, 81–83

liquid argon (LAr) Argon in its liquid phase; it is a cryogenic liquid with a boiling point of 87 K and density of 1.4 g/ml. 93

liquid argon time-projection chamber (LArTPC) A TPC filled with liquid argon; the basis for the DUNE far detector (FD) modules. 91

Long-Baseline Neutrino Facility (LBNF) The organizational entity responsible for developing the neutrino beam, the cryostats and cryogenics systems, and the conventional facilities for DUNE. 92, 93

LBNF and DUNE project (LBNF/DUNE) The overall global project, including Long-Baseline Neutrino Facility (LBNF) and DUNE. 91

Laboratori Nazionali di Frascati (LNF) Istituto Nazionale di Fisica Nucleare (INFN) laboratory in Italy. 47, 54, 81

minimum ionizing particle (MIP) Refers to a particle traversing some medium such that the particle's mean energy loss is near the minimum. 6

photoelectron (PE) An electron ejected from the surface of a material by the photoelectric effect. 13

photomultiplier tube (PMT) A device that makes use of the photoelectric effect to produce an electrical signal from the arrival of optical photons. 1, 5, 46

protons on target (POT) Typically used as a unit of normalization for the number of protons striking the neutrino production target. 12

quality assurance (QA) The process of ensuring that the quality of each element meets requirements during design and development, and to detect and correct poor results prior to production. 61, 62

quality control (QC) The process (e.g., inspection, testing, measurements) of ensuring that each manufactured element meets its quality requirements prior to assembly or installation. 61, 62

System for on-Axis Neutrino Detection (SAND) The beam monitor component of the near detector that remains on-axis at all times and serves as a dedicated neutrino spectrum monitor. 5, 10, 12

secondary DAQ buffer A secondary DAQ buffer holds a small subset of the full rate as selected by a trigger command. This buffer also marks the interface with the DUNE Offline. 91

silicon photomultiplier (SiPM) A solid-state avalanche photodiode sensitive to single photoelectron signals. 5

single-phase (SP) Distinguishes one of the DUNE far detector technologies by the fact that it operates using argon in its liquid phase only. 91

Sanford Underground Research Facility (SURF) The laboratory in South Dakota where the LBNF far site conventional facilities (FSCF) will be constructed and the DUNE FD will be installed and operated. 91, 92

time projection chamber (TPC) A type of particle detector that uses an E field together with a sensitive volume of gas or liquid, e.g., liquid argon (LAr), to perform a 3D reconstruction of a particle trajectory or interaction. The activity is recorded by digitizing the waveforms of current induced on the anode as the distribution of ionization charge passes by or is collected on the electrode (TPC is also used for "total project cost"). 92

trigger candidate Summary information derived from the full data stream and representing a contribution toward forming a trigger decision. 93, 94

trigger command Information derived from one or more trigger candidates that directs elements of the far detector module to read out a portion of the data stream. 93, 94

trigger decision The process by which trigger candidates are converted into trigger commands. 91, 93

References

[1] DOE Office of High Energy Physics, "Mission Need Statement for a Long-Baseline Neutrino Experiment (LBNE)," tech. rep., DOE, 2009. LBNE-doc-6259.

[2] M. Adinolfi *et al.*, "The KLOE electromagnetic calorimeter," *Nuclear Instruments and Methods in Physics Research Section A: Accelerators, Spectrometers, Detectors and Associated Equipment* **482** (2002) 364. https://www.sciencedirect.com/science/article/pii/S0168900201015029.

[3] W. T. Welford and R. Winston, *The Optics of Nonimaging Concentrators*. Academic Press, New York, first ed., 1978.

[4] "https://www.digchip.com/datasheets/parts/datasheet/190/r5946.php.".

[5] F. Alemanno, P. Bernardini, A. Corvaglia, G. D. Matteis, L. Martina, A. Miccoli, M. Panareo, M. Panetta, C. Pinto, and A. Surdo, "Study of silicon photomultipliers for the readout of a lead/scintillating-fiber calorimeter," *Journal of Instrumentation* **19** no. 06, (Jun, 2024) T06005. https://dx.doi.org/10.1088/1748-0221/19/06/T06005.

[6] A. Gallo *et al.*, "DAFNE status report," *Conf. Proc. C* **060626** (2006) 604–606. https://inspirehep.net/literature/724788.

[7] M. Anelli *et al.*, "Measurement and simulation of the neutron response and detection efficiency of a Pb-scintillating fiber calorimeter," *Nucl. Instrum. Meth. A* **581** (2007) 368–372.

[8] G. Adamov, et al., "A Proposal to Enhance the DUNE Near-Detector Complex," 2021. www.mi.infn.it/~ragusa/tracking_sns_28.05.2014.pdf. DocDB 13262.

[9] C. Bini et al., "Evaluation of the p erformance of the KLOE calorimeter barrel mo dules at the Cosmic Ray Stand," 1996. http://www.lnf.infn.it/kloe/kdocs/getfile.php?doc_fname=kn154.ps. KLOE Note N.154 February 1996.

[10] M. Adinolfi *et al.*, "The KLOE electromagnetic calorimeter," *Nucl. Instrum. Meth.* **A482** (2002) 364–386.

[11] **KLOE** Collaboration, A. Ceccarelli, S. Dell'Agnello, A. Di Virgilio, and S. Moccia, "Survey and alignment of the KLOE experiment at DAPHNE," *eConf* **C971013** (1997) 025.

[12] K. Smith, A. Broadbent, M. Greenslade, S. Harrison, D. Jenkins, J. Ross, A. Street, M. Townsend, J. Wiatrzyk, and J. Franzini, "Progress in the design and manufacture of the KLOE solenoid for the DAPHNE ring at Frascati," *IEEE Trans. Appl. Supercond.* **7** no. 2, (1997) 630–632.

[13] C. Ligi, et al., "DAΦNE CRYOGENIC COOLING SYSTEM: STATUS AND PERSPECTIVES," 2002. https://accelconf.web.cern.ch/e02/PAPERS/MOPLE026.pdf. Proceedings of EPAC, Paris.

[14] M. Modena, "The DAΦNE Cryogenic System," 1997. https://inis.iaea.org/collection/NCLCollectionStore/_Public/29/056/29056136.pdf. LNF-97/046.